Spectroscopic, Structural, Electrochemical, and Kinetic Studies of Ligand Substitution in the 33e Dinuclear Radical $Fe_2(CO)_7(\mu\text{-}PPh_2)$ and the 34e Analogues $[Fe_2(CO)_7(\mu\text{-}PPh_2)]^-$ and $FeCo(CO)_7(\mu\text{-}PPh_2)$

R. T. Baker,*,† J. C. Calabrese,† P. J. Krusic,*,† M. J. Therien,‡ and W. C. Trogler*,‡

Contribution No. 4417 from the Central Research and Development Department, E. I. du Pont de Nemours and Company, Experimental Station, Wilmington, Delaware 19898, and Department of Chemistry, University of California at San Diego, La Jolla, California 92093.
Received October 13, 1987

Abstract: The 33e dinuclear radical $Fe_2(CO)_7(\mu\text{-}PPh_2)$ undergoes rapid CO ligand substitution with a variety of tertiary phosphorus ligands, L, to give mono- and disubstituted 33e products, which were characterized by elemental analysis and by IR and ESR spectroscopy. While the first substitution gives a single product, with L on the six-coordinate Fe center trans to the PPh_2 bridge (confirmed by X-ray diffraction for L = $P(OMe)_3$), further substitution (observed for L = PMe_3, PEt_3, $P(OMe)_3$) is complex, giving two isomeric 33e disubstituted radicals, minor amounts of 35e addition products $Fe_2(CO)_6L_2(\mu\text{-}PPh_2)$, and diamagnetic disproportionation products $[Fe_2(CO)_5L_3(\mu\text{-}PPh_2)]^+[Fe_2(CO)_{8-n}L_n(\mu\text{-}PPh_2)]^-$ (L = PMe_3, n = 0; L = $P(OMe)_3$, n = 2), as confirmed by an X-ray diffraction study of the PMe_3 derivative. The 34e anion $[Fe_2(CO)_6(\mu\text{-}CO)(\mu\text{-}PPh_2)]^-$, as the $(Et_4N)^+$ salt, adds two ligands in THF to give the 36e anions $[Fe_2(CO)_6L_2(\mu\text{-}PPh_2)]^-$ (L = PMe_3, PPh_3, $P(OMe)_3$), which have one L on each Fe, both trans to the PPh_2 bridge (confirmed by X-ray diffraction for L = PPh_3). The intermediacy of the monosubstituted 34e anion was ruled out. The 34e heterobimetallic complex $FeCo(CO)_7(\mu\text{-}PPh_2)$ reacts with PPh_3 to give a 34e kinetic product with L on Co trans to the PPh_2 bridge; this product rearranges at 25 °C to the thermodynamic product with L on Fe. With $P(OMe)_3$, monosubstitution occurs as above and disubstitution gives both 34e and 36e products, both with one L on each metal (confirmed for the 34e product by X-ray diffraction). With PMe_3, ligand addition gives 36e $FeCo(CO)_7L(\mu\text{-}PPh_2)$, with L on Co. Electrochemical studies show that the 33e unsubstituted and monosubstituted diiron radicals exhibit chemically reversible 1e reductions to give the 34e CO-bridged anions. A 1e oxidation of the disubstituted 36e anion $[Fe_2(CO)_6(PPh_3)_2(\mu\text{-}PPh_2)]^-$ leads to the monosubstituted 33e radical, via loss of PPh_3. While oxidation of 34e $FeCo(CO)_7(\mu\text{-}PPh_2)$ is chemically irreversible, 1e reduction leads to CO loss to give the 33e radical anion $[FeCo(CO)_6(\mu\text{-}PPh_2)]^-$, which undergoes a further chemically reversible reduction to the 34e dianion. Similarly, 1e reduction of monosubstituted $FeCo(CO)_6(PPh_3)(\mu\text{-}PPh_2)$ gives the 33e monosubstituted radical anion via CO loss, while a chemically reversible 1e oxidation gives the 33e radical cation $[FeCo(CO)_6(PPh_3)(\mu\text{-}PPh_2)]^+$. Kinetic studies of ligand monosubstitution in the 33e diiron radical $Fe_2(CO)_7(\mu\text{-}PPh_2)$ using transient electrochemical techniques are consistent with an associative mechanism involving a 35e radical intermediate. Activation parameters obtained support the proposed associative pathway. Comparison of the reactivities of 33e $Fe_2(CO)_7(\mu\text{-}PPh_2)$ and its 34e analogues $[Fe_2(CO)_6(\mu\text{-}CO)(\mu\text{-}PPh_2)]^-$ and $FeCo(CO)_7(\mu\text{-}PPh_2)$ show that the radical complex is about 10^5–10^6 times more reactive toward PPh_3 than the diamagnetic 34e compounds. The mono- and disubstituted 35e radicals have been observed by ESR spectroscopy for various L's and are proposed to have a $(CO)_2$-bridged structure, with two six-coordinate metal centers. Analogous 36e intermediates in the $[Fe_2]^-$ and FeCo systems have the all-terminal-CO structure, with two five-coordinate metal centers.

We recently reported[1,2] the synthesis and an ESR and IR study of a new family of stable 33e dinuclear radicals $Fe_2(CO)_7(\mu\text{-}PR_2)$ [R = alkyl, phenyl (**1**)] prepared by 1e oxidation of the 34e and 36e anions[3] $[Fe_2(CO)_7(\mu\text{-}PR_2)]^-$ (**6**) and $[Fe_2(CO)_8(\mu\text{-}PR_2)]^-$ (**7**) with $[Cp_2Fe]BF_4$ (Scheme I). Although we were unable to obtain single crystals of **1** suitable for an X-ray diffraction study, our data support the structure shown in Scheme I in which a phosphido group bridges a six-coordinate iron center and a five-coordinate, distorted trigonal-bipyramidal iron center. Such a structure has been established before[4] for the 34e diamagnetic analogue $FeCo(CO)_7(\mu\text{-}PMe_2)$ in which a cobalt replaces the five-coordinate iron of **1** and which is isoelectronic with the anion $[Fe_2(CO)_7(\mu\text{-}PR_2)]^-$ (**6**). The principal characteristics of these novel phosphido-bridged diiron carbonyl radicals can be summarized as follows:

(a) The unpaired electron is almost exclusively localized on the five-coordinate iron and on the carbonyl ligands 1 and 2 (Scheme I), which lie in the equatorial plane of the distorted trigonal bipyramid. This conclusion was recently established beyond doubt by an ESR study of single crystals of diamagnetic $FeCo(CO)_7(\mu\text{-}PPh_2)$ (**8**) containing **1** as a paramagnetic substitutional impurity.[2] This latter study also confirms that **1** and $FeCo(CO)_7(\mu\text{-}PPh_2)$ are isostructural.

(b) The dinuclear radicals are fluxional in solution on the ESR time scale and show five equivalent ^{13}C nuclei at −80 °C. We suggested that the equivalence is caused by a rapid interchange of carbons 1–5, which lie close to the equatorial plane of the idealized structure, via a CO-bridged transition state with a structure similar to that of the 34e anion $[Fe_2(CO)_7(\mu\text{-}PR_2)]^-$ (**6**, Scheme I).

Scheme I

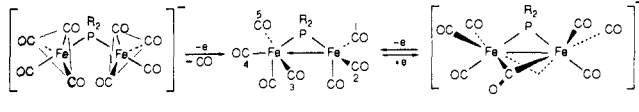

7, R = Ph 1, R = Ph 6, R = Ph

(c) Studies with ^{13}CO showed complete CO exchange in seconds in dilute solutions at 25 °C. In the presence of CO, **1** exists in equilibrium with the 35e CO adduct **3** (eq 1). At 25 °C the

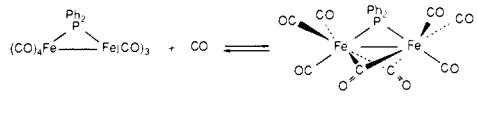

(1)

1 3

† E. I. du Pont de Nemours and Co.
‡ University of California at San Diego.

(1) Baker, R. T.; Krusic, P. J.; Calabrese, J. C.; Roe, D. C. *Organometallics* **1986**, *5*, 1506.
(2) Baker, R. T.; Calabrese, J. C.; Krusic, P. J.; Morton, J. R.; Preston, K. F.; LePage, Y., accepted for publication in *J. Am. Chem. Soc.*
(3) Osterloh, W. T. Ph.D. Thesis, University of Texas, Austin, TX 1982; University Microfilms International Ann Arbor, MI, 1982.
(4) Keller, E.; Vahrenkamp, H. *Chem. Ber.* **1977**, *110*, 430.

0002-7863/88/1510-8392$01.50/0

equilibrium strongly favors **1** but shifts markedly toward the adduct at lower temperatures and at higher CO pressures. ^{13}C-labeling ESR studies and extended Hückel MO calculations are in agreement with a symmetric structure for **3**, shown in eq 1, in which the unpaired electron is delocalized mostly over the two *bridging carbonyl ligands*. The very small spin density on the two irons is responsible for a *g* factor close to the free-spin value and an unusually narrow line width. Thus, the CO adduct **3** can be easily recognized by ESR in the presence of **1**, which has a much larger *g* factor.

(d) Radical **1** (R = Et) is substitutionally very labile and reacts instantaneously in dilute solutions with 1 equiv of $P(OMe)_3$ to give the monosubstituted derivative $Fe_2(CO)_6[P(OMe)_3](\mu\text{-}PEt_2)$. Since the added phosphorus is invisible by ESR and since the ^{13}CO-exchanged species still showed five equivalent CO ligands just as the unsubstituted radical, the phosphorus ligand had to occupy a position trans to the phosphido bridge, most likely on the six-coordinate iron, where it would not interfere with the interchange of the five equatorial CO ligands. This is now confirmed herein by an X-ray diffraction study of the PPh_2 analogue.

In view of the interest in CO ligand substitution in 17e mononuclear[5-16] and odd-electron multinuclear metal carbonyl radicals,[17-19] we have investigated the substitution chemistry and kinetics of $Fe_2(CO)_7(\mu\text{-}PPh_2)$ with a variety of tertiary phosphorus ligands and compared the results with those for the diamagnetic analogues $[Fe_2(CO)_6(\mu\text{-}CO)(\mu\text{-}PPh_2)]^-$ (**6**) and $FeCo(CO)_7(\mu\text{-}PPh_2)$ (**8**). For mononuclear complexes an increase of 10^9–10^{10} in associative ligand substitution rates has been observed for 17e radicals as compared to those of their 18e counterparts.[12,14,16]

Ohst and Kochi[17] recently examined electron-transfer catalysis of CO substitution in $Fe_3(\mu_3\text{-}PPh)_2(CO)_9$ on reduction to the anion radical. The reduced species was labile toward CO substitution by a mechanism that involved slippage of the μ_3-PPh cap to a μ_2 isomer to form a 17e iron center. Rates for the primary substitution step could not be obtained. The $Fe_2(CO)_7(\mu\text{-}PPh_2)$ radical was therefore an attractive candidate for mechanistic study because one can directly probe the mechanism of substitution at a 17e metal center in a cluster environment. Furthermore, the stability of the dinuclear radicals provides a unique opportunity for detailed characterization of their molecular structures.

The pioneering work of Vahrenkamp and co-workers[20-22] demonstrated three stepwise CO ligand substitutions in $FeCo(CO)_7(\mu\text{-}AsMe_2)$ by PMe_3 and $P(OMe)_3$ through a sequence of metal–metal bond breaking and subsequent bond reforming with loss of CO. In addition, it was shown that the kinetic substitution product has the ligand on the five-coordinate Co center trans to the $AsMe_2$ bridge, while the thermodynamic product has the ligand on the six-coordinate Fe center. The detailed stereochemistry and stereoselectivity of further substitutions, however, were not determined. The recent investigations of Carty, Dixneuf, and coworkers[23-25] on CO ligand substitution in $RuCo(CO)_7(\mu\text{-}PPh_2)$ with a variety of phosphine ligands showed that thermodynamic mono- and disubstituted products have the ligands on Ru exclusively and that the detailed stereochemistry and distribution of the isomeric products are a sensitive function of the ligand. Trisubstitution with $P(OMe)_3$ gave a single isomer with one ligand on each metal center trans to the Ru–Co bond and the third ligand on Ru trans to the PPh_2 bridge.

In this work we report the following: (1) the detailed stereoselectivity and stereochemistry of ligand substitution in $Fe_2(CO)_7(\mu\text{-}PPh_2)$, $[Fe_2(CO)_6(\mu\text{-}CO)(\mu\text{-}PPh_2)]^-$, and $FeCo(CO)_7(\mu\text{-}PPh_2)$; (2) the electrochemistry of the Fe_2 and FeCo systems, which leads to the identification of new cationic and anionic 33e FeCo radicals; and (3) the kinetics of ligand substitution in $Fe_2(CO)_7(\mu\text{-}PPh_2)$. The latter is consistent with an associative mechanism and exhibits rate enhancements of 10^5–10^6 over the diamagnetic $[Fe_2]^-$ and FeCo analogues.

Experimental Section

Materials and Spectroscopic Characterization. All manipulations were performed at ambient temperature in a nitrogen-filled Vacuum Atmospheres Dri-Lab glovebox with continuous purge. Solvents were purified by standard methods and distilled under argon from sodium or potassium benzophenone ketyl. Literature methods were used to prepare $Fe_2(CO)_7(PPh_2)$,[1] $[Et_4N][Fe_2(CO)_7(PPh_2)]$,[3] and $FeCo(CO)_7(PPh_2)$.[26] Tertiary phosphorus ligands were used as obtained from Strem Chemicals. NMR spectra were obtained on a Nicolet NMC-300 wide-bore (300-MHz ^1H and 120.5-MHz ^{31}P) spectrometer, and ^{31}P NMR chemical shifts are positive downfield from external 85% H_3PO_4. IR spectra were recorded on a Perkin-Elmer 983 or IBM FTIR/32 spectrometer by using KBr solution cells with a path length of 0.1 mm or as mineral oil mulls by using NaCl plates. ESR spectra were recorded on a Bruker ER420 spectrometer equipped with a field-tracking gaussmeter and a microwave frequency counter. Photolyses were performed in Pyrex NMR tubes with a concentric coil apparatus described previously.[27] Elemental analysis was performed by Pascher Mikroanalytisches Labor, Remagen, West Germany.

Synthesis. $Fe_2(CO)_6(PPh_3)(\mu\text{-}PPh_2)$ (2a). A solution of 130 mg (0.5 mmol) of PPh_3 in 20 mL of THF was added dropwise to a solution of 245 mg (0.5 mmol) of $Fe_2(CO)_7(\mu\text{-}PPh_2)$ in 20 mL of THF, and the resulting green solution was stirred for 18 h. The solvent was removed in vacuo and the residue washed with 2 × 10 mL of pentane and dried in vacuo, yielding 263 mg (72%) of **2a**.

In another experiment, a solution of 56 mg (0.05 mmol) of $Et_4N[Fe_2(CO)_6(PPh_3)_2(\mu\text{-}PPh_2)]$ in 5 mL of acetone was treated with 10 mg (0.05 mmol) of $AgBF_4$ giving silver metal and a green solution of **2a**. After 1 h, the solvent was removed in vacuo. The residue was extracted with hexane, and the IR and ESR spectra were recorded.

Generation of $Fe_2(CO)_6(PMe_3)(\mu\text{-}PPh_2)$ (2b). A solution of 15 mg (0.2 mmol) of PMe_3 in 10 mL of THF was added dropwise to a solution

(5) Darchen, A.; Mahe, C.; Patin, H. *J. Chem. Soc., Chem. Commun.* **1982**, 243.
(6) (a) Hershberger, J. W.; Kochi, J. K. *J. Chem. Soc., Chem. Commun.* **1982**, 212. (b) Hershberger, J. W.; Klingler, R. J.; Kochi, J. K. *J. Am. Chem. Soc.* **1982**, *104*, 3034.
(7) Zizelman, P. M.; Amatore, C.; Kochi, J. K. *J. Am. Chem. Soc.* **1984**, *106*, 3771.
(8) (a) Narayanan, B. A.; Amatore, C.; Kochi, J. K. *Organometallics* **1986**, *5*, 926. (b) Narayanan, B. A.; Amatore, C.; Kochi, J. K. *Ibid.* **1987**, *6*, 129.
(9) (a) Stiegman, A. E.; Steiglitz, M.; Tyler, D. R. *J. Am. Chem. Soc.* **1983**, *105*, 6032. (b) Stiegman, A. E.; Goldman, A. S.; Leslie, D. B.; Tyler, D. R. *J. Chem. Soc., Chem. Commun.* **1984**, 632. (c) Stiegman, A. E.; Tyler, D. R. *Inorg. Chem.* **1984**, *23*, 527. (d) Goldman, A. S.; Tyler, D. R. *J. Am. Chem. Soc.* **1984**, *106*, 4066. (e) Stiegman, A. E.; Tyler, D. R. *Comments Inorg. Chem.* **1986**, *5*, 215.
(10) (a) Herrinton, T. R.; Brown, T. L. *J. Am. Chem. Soc.* **1985**, *107*, 5700. (b) Wegman, R. W.; Olson, R. J.; Gard, D. R.; Faulkner, L. R.; Brown, T. L. *Ibid.* **1981**, *103*, 6089. (c) McCullen, S. B.; Brown, T. L. *Ibid.* **1982**, *104*, 7496. (d) McCullen, S. B.; Walker, H. W.; Brown, T. L. *Ibid.* **1982**, *104*, 4007.
(11) Doxsee, K. M.; Grubbs, R. H.; Anson, F. C. *J. Am. Chem. Soc.* **1984**, *106*, 7819.
(12) (a) Shi, Q.-Z.; Richmond, T. G.; Trogler, W. C.; Basolo, F. *J. Am. Chem. Soc.* **1984**, *106*, 71. (b) Richmond, T. G.; Shi, Q.-Z.; Trogler, W. C.; Basolo, F. *Ibid.* **1984**, *106*, 76.
(13) (a) Kowaleski, R. M.; Trogler, W. C.; Basolo, F. *Gazz. Chim. Ital.* **1986**, *116*, 105. (b) Kowaleski, R. M.; Basolo, F.; Trogler, W. C.; Ernst, R. D. *J. Am. Chem. Soc.* **1986**, *108*, 6046.
(14) Trogler, W. C. *Int. J. Chem. Kinet.* **1987**, *109*, 5127.
(15) Broadley, K.; Connelly, N. G.; Geiger, W. E. *J. Chem. Soc., Dalton Trans.* **1983**, 121.
(16) Therien, M. J.; Ni, C.-L.; Anson, F. C.; Osteryoung, J. G.; Trogler, W. C. *J. Am. Chem. Soc.* **1986**, *108*, 4037.
(17) (a) Ohst, H. H.; Kochi, J. K. *J. Am. Chem. Soc.* **1986**, *108*, 2897. (b) Ohst, H. H.; Kochi, J. K. *Inorg. Chem.* **1986**, *25*, 2066. (c) Ohst, H. H.; Kochi, J. K. *Organometallics* **1986**, *5*, 1359. (d) Richmond, M. G.; Kochi, J. K. *Inorg. Chem.* **1986**, *25*, 656. (e) Richmond, M. G.; Kochi, J. K. *Organometallics* **1987**, *6*, 254.
(18) (a) Schroeder, N. C.; Angelici, R. J. *J. Am. Chem. Soc.* **1986**, *108*, 3688. (b) Hommeltoft, S. I.; Berry, D. H.; Eisenberg, R. *J. Am. Chem. Soc.* **1986**, *108*, 5345.
(19) Downard, A. J.; Robinson, B. H.; Simpson, J. *Organometallics* **1986**, *5*, 1122, 1132, 1140, and references cited therein.
(20) Mayr, A.; Ehrl, W.; Vahrenkamp, H. *Chem. Ber.* **1974**, *107*, 3860.
(21) Langenbach, H.-J.; Vahrenkamp, H. *Chem. Ber.* **1977**, *110*, 1195.
(22) Langenbach, H.-J.; Vahrenkamp, H. *Chem. Ber.* **1979**, *112*, 3391.
(23) Regragui, R.; Dixneuf, P. H.; Taylor, N. J.; Carty, A. J. *Organometallics* **1984**, *3*, 1020.
(24) Regragui, R.; Dixneuf, P. H.; Taylor, N. J.; Carty, A. J. *Organometallics* **1986**, *5*, 1.
(25) Guesmi, S.; Taylor, N. J.; Dixneuf, P. H.; Carty, A. J. *Organometallics* **1986**, *5*, 1964.
(26) Benson, B. C.; Jackson, R.; Joshi, K. K.; Thompson, D. T. *J. Chem. Soc., Chem. Commun.* **1968**, 1506.
(27) Krusic, P. J.; Jones, D. J.; Roe, D. C. *J. Am. Chem. Soc.* **1986**, *5*, 456.

of 98 mg (0.2 mmol) of $Fe_2(CO)_7(\mu\text{-}PPh_2)$ in 10 mL of THF, and the IR and ESR spectra of **2b** were recorded.

$Fe_2(CO)_6(PEt_3)(\mu\text{-}PPh_2)$ (2c). A solution of 40 mg (0.34 mmol) of PEt_3 in 5 mL of hexane was added dropwise to a solution of 80 mg (0.16 mmol) of $Fe_2(CO)_7(\mu\text{-}PPh_2)$ in 5 mL of hexane giving a green solution with a small quantity of red-orange solid. While not completely characterized, the IR spectrum suggests the latter is a disproportionation product analogous to **5a,b**. After 1 h the solution was filtered, concentrated to 1 mL, and cooled at −20 °C for 20 h. The resulting dark green crystals were filtered off and dried in vacuo to yield 68 mg (73%) of **2c**.

$Fe_2(CO)_6[P(OMe)_3](\mu\text{-}PPh_2)$ (2d). A solution of 98 mg (0.8 mmol) of $P(OMe)_3$ in 25 mL of THF was added dropwise to a solution of 394 mg (0.8 mmol) of $Fe_2(CO)_7(\mu\text{-}PPh_2)$ in 25 mL of THF. The resulting green solution was stirred for 2 h, the solvent was removed in vacuo, and the residue was extracted with 30 mL of pentane, yielding 185 mg of a yellow solid (**5b**, see later) and a green filtrate. The latter was concentrated to 5 mL and cooled at −20 °C for 18 h to yield 228 mg of green crystals of **2d** (48%).

Generation of $Fe_2(CO)_5(PMe_3)_2(\mu\text{-}PPh_2)$ (4a, 4a′) and Isolation of $[Fe_2(CO)_5(PMe_3)_3(\mu\text{-}PPh_2)][Fe_2(CO)_8(\mu\text{-}PPh_2)]$ (5a). A solution of 80 mg (1.1 mmol) of PMe_3 in 5 mL of toluene was added dropwise to a solution of 245 mg (0.5 mmol) of $Fe_2(CO)_7(\mu\text{-}PPh_2)$ in 15 mL of toluene. After the solution was stirred for 45 min, the orange precipitate was filtered, washed with 5 mL of pentane, and dried in vacuo to yield 192 mg of **5a** (65%). The green filtrate was shown to be **4a,4a′** by IR and ESR spectroscopy. Complex **5a** was recrystallized from THF–Et_2O to give orange-red plates.

Generation of $Fe_2(CO)_5[P(OMe_3)]_2(\mu\text{-}PPh_2)$ (4c, 4c′) and Isolation of $[Fe_2(CO)_5[P(OMe)_3]_3(\mu\text{-}PPh_2)][Fe_2(CO)_6[P(OMe)_3]_2(\mu\text{-}PPh_2)]$ (5b). A solution of 185 mg (1.5 mmol) of $P(OMe)_3$ in 5 mL of toluene was added dropwise to a solution of 245 mg (0.5 mmol) of $Fe_2(CO)_7(\mu\text{-}PPh_2)$ in 25 mL of toluene. After the solution was stirred for 30 min, the yellow-orange precipitate was filtered, washed with 5 mL of pentane, and dried in vacuo to yield 270 mg of crude **5b**. The green filtrate was shown to be **4c,4c′** by IR and ESR spectroscopy. Crude **5b** was recrystallized from THF–Et_2O to give 195 mg of fibrous yellow crystals of pure **5b** (51%).

Generation of $Fe_2(CO)_5(PEt_3)_2(\mu\text{-}PPh_2)$ (4b, 4b′). A solution of 96 mg (0.8 mmol) of PEt_3 in 5 mL of THF was added dropwise to a solution of 40 mg (0.1 mmol) of $Fe_2(CO)_7(\mu\text{-}PPh_2)$ in 5 mL of THF. The solution turns from red-brown to green-brown. The ESR spectrum of **4b**, **4b′** was recorded, and the THF solution IR spectrum showed also small amounts of disproportionation products.

Generation of 35e $Fe_2(CO)_{8-n}L_n(\mu\text{-}PPh_2)$ (3a–f). For the monosubstituted radicals, a ca. 0.01 M solution of **2c,d** was saturated with CO, and the ESR spectrum was recorded. For the disubstituted radicals, a ca. 0.01 M solution of $Fe_2(CO)_7(\mu\text{-}PPh_2)$ in THF was allowed to react with an excess of L in a closed ESR tube, and the ESR spectrum was recorded. Alternatively, toluene solutions of **4a–c**, generated as described above, were saturated with CO and the ESR spectra recorded.

Generation of $Fe_2(CO)_{7-n}[P(OMe)_3]_n(\mu\text{-}PEt_2)$ Radicals and Their 35e CO Adducts. A 0.01 M solution of $Fe_2(CO)_7(\mu\text{-}PEt_2)$ in pentane was treated with a 0.01 M solution of $P(OMe)_3$ in 1:1, 1:2, 1:3, and 1:5 ratios, and the ESR spectra were recorded. The solutions were then saturated with CO and the ESR spectra recorded again.

$[Et_4N][Fe_2(CO)_6(PPh_3)_2(\mu\text{-}PPh_2)]$ (7a). A solution of 623 mg (1.0 mmol) of $Et_4N[Fe_2(CO)_7(\mu\text{-}PPh_2)]$ and 526 mg (2.0 mmol) of PPh_3 in 20 mL of THF was stirred for 4 days, and the resulting yellow powder was filtered, washed with 10 mL of cold (−20 °C) THF and then 10 mL of Et_2O, and dried in vacuo to yield 500 mg of **7a**. Concentration of the filtrate to 5 mL yielded a second crop of 56 mg of yellow crystals, bringing the total yield of **7a** to 576 mg (51%).

The PMe_3 analogue was prepared similarly with 310 mg (4.0 mmol) of PMe_3 and 623 mg of $[Et_4N][Fe_2(CO)_7(\mu\text{-}PPh_2)]$ to yield 556 mg of **7b** as a yellow solid (74%).

The $P(OMe)_3$ analogue was prepared similarly with 248 mg (2.0 mmol) of $P(OMe)_3$ and 623 mg of $[Et_4N][Fe_2(CO)_7(\mu\text{-}PPh_2)]$ to yield 550 mg of **7c** as a yellow solid (65%).

Generation of $[Et_4N][Fe_2(CO)_5(PPh_3)(\mu\text{-}CO)(\mu\text{-}PPh_2)]$ (6a). A solution of 56 mg (0.05 mmol) of **7a** in CD_3CN was photolyzed at 0 °C in an NMR tube for 60 min, and the ^{31}P NMR spectrum was recorded, indicating >95% conversion to PPh_3 and **6a**. The solvent was removed in vacuo, and the IR spectrum was recorded as a Nujol mull. In another experiment performed in THF, the photolyzed solution was allowed to undergo thermal back-reaction at 25 °C. After 4 weeks the ratio of **7a** to **6a** was ca. 3:1.

Identical photolysis reactions with the PMe_3 and $P(OMe)_3$ analogues (**7b,c**) indicated conversions of 35 and 60%, respectively, to give **6b,c** and the disubstituted analogues $[Et_4N][Fe_2(CO)_4L_2(\mu\text{-}CO)(\mu\text{-}PPh_2)]$ (**6d,e**).

Generation of $Et_4N[Fe_2(CO)_7L(\mu\text{-}PPh_2)]$ (7d–f). The CD_3CN solutions of **6a–e**, obtained as above, were evaporated to dryness, and the residue was washed with 5 mL of hexane and 5 mL of Et_2O to remove excess L. The residue was then redissolved in CD_3CN and CO was bubbled through the solution until the red-orange color changed to orange. The ^{31}P NMR spectra of **7d–f** were then recorded. Addition of excess L to these solutions led rapidly (<5 min) to formation of disubstituted **7a–c**.

$FeCo(CO)_6(PPh_3)(\mu\text{-}PPh_2)$ (8a). A solution of 52 mg (0.2 mmol) of PPh_3 and 100 mg (0.2 mmol) of $FeCo(CO)_7(\mu\text{-}PPh_2)$ in 5 mL of THF was stirred for 20 h, and the solvent was removed in vacuo. The residue was washed with 10 mL of pentane, and the resulting red-brown solid was dried in vacuo to yield 110 mg of **8a** (75%). In another experiment this reaction was monitored at 2-h intervals by ^{31}P NMR spectroscopy.

Generation of $FeCo(CO)_6[P(OMe)_3](\mu\text{-}PPh_2)$ (8b and 8b′). Complex **8b′** was generated from 25 mg (0.2 mmol) of $P(OMe)_3$ and 100 mg of $FeCo(CO)_7(\mu\text{-}PPh_2)$ in 5 mL of toluene, and its formation was monitored at 2-h intervals by IR and ^{31}P NMR spectroscopy. The yield was estimated by ^{31}P NMR spectroscopy to be ca. 85%, with the remainder being the unsubstituted and disubstituted complexes. Heating a toluene solution of **8b′** at 60 °C for 12 h gave quantitative conversion to isomeric **8b**.

$FeCo(CO)_7(PMe_3)(\mu\text{-}PPh_2)$ (11). A solution of 40 mg (0.5 mmol) of PMe_3 in 3 mL of toluene was added to a solution of 200 mg (0.4 mmol) of $FeCo(CO)_7(\mu\text{-}PPh_2)$ in 2 mL of toluene, yielding an orange solid, which was filtered, washed with 5 mL of pentane, and dried in vacuo to give 158 mg of **11**. A second crop brought the total yield to 200 mg (87%).

Generation of $FeCo(CO)_6(PMe_3)(\mu\text{-}PPh_2)$ (8c) and Its Isomer, 8c′. A suspension of 80 mg (0.13 mmol) of $FeCo(CO)_7(PMe_3)(\mu\text{-}PPh_2)$ (**11**) in 10 mL of toluene was heated at 95 °C for 18 h. The solvent was removed in vacuo, and the IR and ^1H and ^{31}P NMR spectra of **8c** were recorded.

A solution of 57 mg (0.1 mmol) of **11** in THF-d_8 was photolyzed at 0 °C for 2 h, and the ^1H and ^{31}P NMR spectra of **8c′** were recorded. After 24 h at 25 °C, the ^{31}P NMR spectrum indicated complete conversion of **8c′** to **8c**.

Generation of $FeCo(CO)_5(PMe_3)_2(\mu\text{-}PPh_2)$ (9b) and $FeCo(CO)_6(PMe_3)_2(\mu\text{-}PPh_2)$ (10b). A 0.1 mmol sample of **8c**, generated as above, was dissolved in 1 mL of THF-d_8, and 38 mg (0.5 mmol) of PMe_3 was added. After 20 h, the ^{31}P NMR spectra of **9b** and **10b** were recorded.

$FeCo(CO)_5[P(OMe)_3]_2(\mu\text{-}PPh_2)$ (9a). A solution of 50 mg (0.4 mmol) of $P(OMe)_3$ and 100 mg (0.2 mmol) of $FeCo(CO)_7(\mu\text{-}PPh_2)$ in 5 mL of toluene was stirred for 20 h, and the solvent was removed in vacuo. The residue was washed with 5 mL of cold (−20 °C) pentane and dried in vacuo to give 110 mg of a red-brown solid (80%). Complex **9a** was recrystallized from toluene–pentane at −20 °C.

Generation of $[Na(THF)_m]_n[FeCo(CO)_6(\mu\text{-}PPh_2)]$ [12 (n = 1), 13 (n = 2)]. A 0.1 M solution of $FeCo(CO)_7(\mu\text{-}PPh_2)$ in THF was treated with a 0.1 M solution of sodium naphthalenide in THF in 1:1, 1:1.5, and 1:2 ratios. The resulting solutions were monitored by IR, ESR, and ^{31}P NMR spectroscopy.

Attempted Isolation of $[Na(18\text{-crown-}6)_n][FeCo(CO)_6(\mu\text{-}PPh_2)]$ (12′). To a solution of 175 mg (0.35 mmol) of $FeCo(CO)_7(\mu\text{-}PPh_2)$ in 5 mL of THF was added 850 mg of 1.0% Na–Hg amalgam (0.37 mmol). The solution turned from red-brown to green. After the IR and ESR spectra were recorded, 93 mg (0.35 mmol) of 18-crown-6 in 5 mL of THF was added. After 1 h the solvent was removed in vacuo and the red-brown solid washed with 4 × 5 mL of diethyl ether to give 141 mg. Elemental analysis showed the product to be mostly the dianion, $[Na_2(18\text{-crown-}6)][FeCo(CO)_6(\mu\text{-}PPh_2)]$ (**13′**).

Generation of $[FeCo(CO)_6(PPh_3)(\mu\text{-}PPh_2)]BF_4$ (14). A solution of 19 mg (0.1 mmol) of $AgBF_4$ in 5 mL of CH_2Cl_2 was added dropwise to a solution of 73 mg (0.1 mmol) of $FeCo(CO)_6(PPh_3)(\mu\text{-}PPh_2)$ in 5 mL of CH_2Cl_2, and the IR and ESR spectra were recorded.

Molecular Structure Determinations. Crystals suitable for X-ray diffraction were obtained as described above with the exception of **7a**, which was recrystallized from acetone–diethyl ether. A summary of the crystallographic results is presented in Table VII. All data sets were collected at low temperatures on Enraf-Nonius CAD4 diffractometers with graphite-filtered Mo radiation. The data were reduced in the usual fashion for Lorentz–polarization, and, in the case of **5a**, for a 16% decay in intensity. In addition, only the **5a** data set was treated for absorption via the $\Delta|F_o - F_c|$ method.[28] The solution and refinement of the structures for **5a**, **7a**, and **9a** were performed on a VAX/IBM cluster system with a local program set. The heavy-atom positions were obtained via automated Patterson analysis and used to phase the reflections for the remaining light atoms via the usual combination of structure factor, Fourier synthesis, and full-matrix least-squares refinement. The solution and refinement for **2d** were performed by the Molecular Structure Corp., College Station, TX. The structure was solved by direct methods[29] and

(28) Walker, N.; Stuart, D. *Acta Crystallogr.* **1983**, *A39*, 158.

Table I. Elemental Analytical Data[a]

complex	no.	% C	% H	% P	% Fe	% N or Co
$Fe_2(CO)_6(PPh_3)(PPh_2)$	**2a**	59.75, 58.93 (59.46)	3.57, 3.72 (3.47)	7.31, 8.20 (8.52)	14.9, 14.8 (15.36)	
$Fe_2(CO)_6(PEt_3)(PPh_2)$	**2c**	49.31, 49.09 (49.44)	4.39, 4.39 (4.32)	10.7, 10.7 (10.62)	18.9, 19.0 (19.16)	
$Fe_2(CO)_6[P(OMe)_3](PPh_2)$	**2d**	42.98, 42.96 (42.82)	3.30, 3.34 (3.25)	10.6, 10.6 (10.52)	18.9, 18.9 (18.96)	
$[Fe_2(CO)_5(PMe_3)_3(PPh_2)]$ $[Fe_2(CO)_8(PPh_2)]$	**5a**	46.55 (46.58)	4.04 (3.99)	12.9 (13.06)	18.7 (18.83)	
$\{Fe_2(CO)_5[P(OMe)_3]_3(PPh_2)\}$ $\{Fe_2(CO)_6[P(OMe)_3]_2(PPh_2)\}$	**5b**	39.90, 39.80 (39.45)	4.34, 4.35 (4.30)	14.3, 14.2 (14.24)	14.7, 14.6 (14.67)	
$Et_4N[Fe_2(CO)_6(PPh_3)_2(PPh_2)]$[b]	**7a**	61.73, 62.16 (66.50)	5.07, 5.20 (5.40)	7.53, 7.42 (8.30)	8.95, 8.81 (9.97)	1.15, 1.20 (1.25)
$Et_4N[Fe_2(CO)_6(PMe_3)_2(PPh_2)]$	**7b**	50.50, 50.60 (51.43)	6.39, 6.32 (6.47)	11.8, 11.8 (12.43)	14.2, 14.1 (14.95)	1.85, 1.77 (1.87)
$Et_4N\{Fe_2(CO)_6[P(OMe)_3]_2(PPh_2)\}$[b]	**7c**	41.63, 41.81 (45.57)	5.19, 5.24 (5.74)	10.3, 10.3 (11.02)	12.2, 12.3 (13.24)	1.52, 1.50 (1.66)
$FeCo(CO)_6(PPh_3)(PPh_2)$[b]	**8a**	56.76, 56.63 (59.21)	3.38, 3.32 (3.45)	8.04, 8.06 (8.48)	7.23, 7.23 (7.65)	7.64, 7.59 (8.07)
$FeCo(CO)_5[P(OMe)_3]_2(PPh_2)$	**9a**	40.49, 40.74 (40.14)	4.20, 4.27 (4.10)	13.5, 13.4 (13.50)	7.99, 7.98 (8.12)	8.54, 8.46 (8.56)
$FeCo(CO)_7(PMe_3)(PPh_2)$	**11**	46.20, 45.90 (46.19)	3.48, 3.46 (3.35)	10.4, 10.8 (10.83)	9.75, 9.57 (9.76)	10.0, 10.1 (10.30)
$[Na_2(18\text{-crown-}6)]$ $[FeCo(CO)_6(PPh_2)]$[c]	**13′**	45.52, 45.88 (46.30)	4.29, 4.26 (4.40)	3.68, 3.56 (3.98)	6.26, 6.25 (7.18)	8.71, 8.60 (7.57)

[a] Found; calculated in parentheses. [b] Samples only ca. 95% pure but relative elemental proportions are correct. [c] Contaminated with monoanion, **12′**. Na: 5.40, 5.27 (5.91).

displayed a slight rotational disorder of the PEt_3 group about the Fe–P bond, resulting in a splitting of the methylene atoms. These were included in the refinement model as complementary atoms with a 1:4 occupancy ratio. All refinements were performed by full-matrix least squares on F, with anisotropic thermal parameters for all non-hydrogen atoms, and included anomalous dispersion terms[30] for Fe and P, as well as idealized hydrogen coordinates as fixed-atom contributors. For the acentric structures, the coordinates used were those corresponding to the enantiomorph with the lowest R value. The final positional and thermal parameters for the non-hydrogen atoms appear in Tables VIII, X, XII, and XIV. Selected bond distances and angles are given in Tables IX, XI, XIII, and XV. Tables of general temperature factors, calculated hydrogen atom positions and structure factor listings are available as supplementary material.

Electrochemical and Kinetic Studies. The supporting electrolyte tetra-*n*-butylammonium hexafluorophosphate, (Southwestern Chemical, Electrometric Grade) was recrystallized twice from a mixture of ethyl acetate and pentane (Burdick and Jackson) and dried in vacuo. Solvents dichloromethane (analytical reagent, Fischer), distilled from CaH_2 under nitrogen, and tetrahydrofuran (analytical reagent, Fischer), distilled from potassium benzophenone ketyl under nitrogen, were stored in Schlenk flasks under an inert atmosphere.

Cyclic voltammetry and double potential step chronocoulometry experiments used a BAS-100 Electrochemical Analyzer interfaced to a BAS Model PL-10 digital plotter. The electrochemical cell consisted of an IBM voltammetric cell assembly equipped with a thermostated jacket. Platinum and glassy carbon disk working electrodes, the platinum wire auxiliary electrode, and the Ag/0.1 M $AgNO_3$ reference electrode (in acetonitrile) were also obtained from IBM Instruments. Temperatures of solutions were measured with a Love digital thermometer (±0.1 °C) calibrated at 0.0 and −78.0 °C. A Brinkman–Lauda RMS constant-temperature circulating bath was used to maintain cell temperature. The cell was blanketed with nitrogen, presaturated with solvent at the same temperature.

In a typical cyclic voltammetry experiment, 5 mL of a 0.15 M tetra-*n*-butylammonium hexafluorophosphate (TBAHFP) stock solution was syringed into the electrochemical cell, and the potential of the working electrode was cycled several times between the initial and final values. Then, 5 mL of a solution 2 mM in the phosphido-bridged metal carbonyl complex and 0.15 M in TBAHFP was syringed into the cell along with a known concentration of nucleophile (if used). Voltammograms were recorded at several scan rates, with stirring between each measurement. Platinum working and auxiliary electrodes were cleaned with aqua regia after each set of experiments. Both the platinum and glassy carbon disk working electrodes were polished with 0.3-μm alumina. No contamination of the electrode surfaces was observed in the potential window of these experiments. Reproducible cyclic voltammograms were obtained throughout the course of each set of experiments.

Chronocoulometric measurements were conducted under the same conditions described above for the cyclic voltammetric measurements. Substituting a silver wire pseudo-reference electrode for the Ag/Ag^+ reference electrode avoided leakage of Ag^+ ions into the test solutions, which lowered the background current. The response ratios Q_R/Q_F were calculated after correction of both Q_R and Q_F for background contributions in blank experiments. Error limits reported for kinetic parameters represent a single standard deviation from unweighted least-squares analysis.

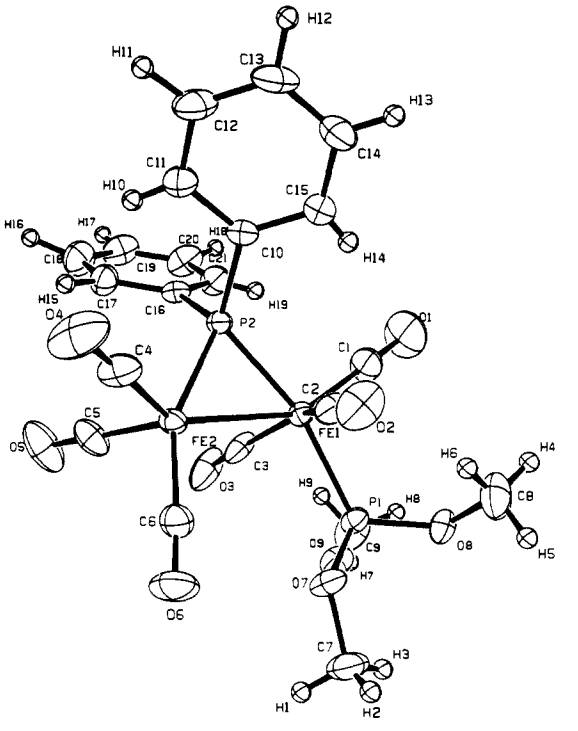

Figure 1. Molecular structure of $Fe_2(CO)_6[P(OMe)_3](\mu\text{-}PPh_2)$ (**2d**).

Scheme II

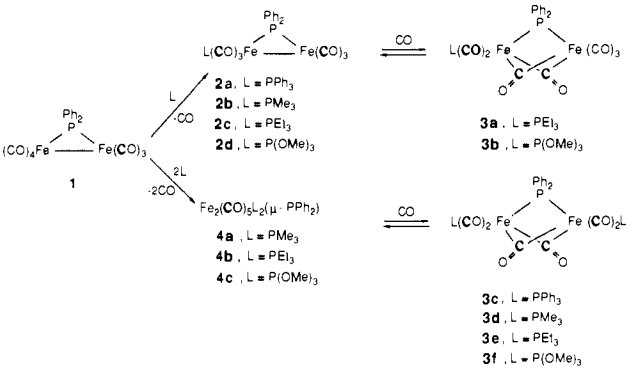

Results and Discussion

Ligand Substitution Reactions of $Fe_2(CO)_7(\mu\text{-}PPh_2)$ (1). The 33e dinuclear radical $Fe_2(CO)_7(\mu\text{-}PPh_2)$ (**1**) reacts rapidly with a variety of tertiary phosphorus ligands, L, in THF solution to

(29) Gilmore, C. J. MITHRIL, University of Glasgow, Scotland, 1983. This is a computer program for the automatic solution of crystal structures from X-ray data.

(30) *International Tables for X-ray Crystallography*; Kynoch: Birmingham, England, 1974; Vol. IV, (a) Table 2.2B, (b) Table 2.31.

Table II. Infrared Spectroscopic Data[a] (cm^{-1})

$Fe_2(CO)_7(PPh_2)$ (**1**) (hexane): 2078 (m), 2022 (vs), 2001 (s), 1960 (m), 1946 (m)
$Fe_2(CO)_6(PPh_3)(PPh_2)$ (**2a**) (hexane): 2037 (s), 1979 (m), 1952 (vs), 1927 (w), 1907 (w)
$Fe_2(CO)_6(PMe_3)(PPh_2)$ (**2b**) (THF): 2028 (m), 1980 (s), 1941 (vs)
$Fe_2(CO)_6(PEt_3)(PPh_2)$ (**2c**) (hexane): 2033 (s), 1980 (s), 1953 (vs), 1935 (m), 1904 (m)
$Fe_2(CO)_6[P(OMe)_3](PPh_2)$ (**2d**) (hexane): 2040 (m), 1994 (s), 1962 (vs, sh), 1956 (vs), 1915 (w, sh)
$Fe_2(CO)_5(PMe_3)_2(PPh_2)$ (**4a**) (THF): 1979 (m), 1939 (vs), 1908 (s, sh), 1891 (s)
$Fe_2(CO)_5(PEt_3)_2(PPh_2)$ (**4b**) (THF): 1979 (m), 1935 (vs), 1916 (m), 1888 (s), 1872 (m, sh)
$Fe_2(CO)_5[P(OMe)_3]_2(PPh_2)$ (**4c**) (THF): 2000 (m), 1958 (vs), 1919 (s), 1900 (m, sh)
$[Fe_2(CO)_5(PMe_3)_3(PPh_2)][Fe_2(CO)_8(PPh_2)]$ (**5a**) (THF): 2032 (m), 2012 (s), 1984 (m, sh), 1968 (s), 1936 (vs), 1918 (vs)
$\{Fe_2(CO)_5[P(OMe)_3]_3(PPh_2)\}\{Fe_2(CO)_6[P(OMe)_3]_2(PPh_2)\}$ (**5b**) (THF): 2067 (w), 2001 (s), 1965 (m, br), 1892 (vs), 1874 (vs), 1861 (vs)
$Et_4N[Fe_2(CO)_6(PPh_3)(PPh_2)]$ (**6a**) (Nujol mull): 2017 (s), 1970 (vs), 1930 (s, sh), 1916 (vs), 1883 (vs, sh), 1868 (vs), 1854 (vs, sh), 1833 (s, sh), 1719 (vs, br)
$Et_4N[Fe_2(CO)_6(PPh_3)_2(PPh_2)]$ (**7a**) (Nujol mull): 1950 (w), 1927 (w), 1863 (vs, sh), 1855 (vs), 1828 (vs)
$Et_4N[Fe_2(CO)_6(PMe_3)_2(PPh_2)]$ (**7b**) (Nujol mull): 1942 (m), 1916 (s), 1855 (vs), 1845 (vs), 1827 (vs, sh), 1818 (vs, sh)
$Et_4N\{Fe_2(CO)_6[P(OMe)_3]_2(PPh_2)\}$ (**7c**) (Nujol mull): 1962 (m), 1938 (m), 1874 (vs), 1862 (vs), 1841 (vs), 1825 (vs, sh)
$FeCo(CO)_6(PPh_3)(PPh_2)$ (**8a**) (THF): 2050 (m), 2043 (m), 1997 (vs), 1977 (vs), 1966 (vs), 1952 (s, sh)
$FeCo(CO)_6[P(OMe)_3](PPh_2)$ (**8b**) (THF): 2060 (w), 2048 (m), 2002 (s), 1971 (vs, br)
$FeCo(CO)_6[P(OMe)_3](PPh_2)$ (**8b′**) (THF): 2060 (m), 1997 (s, sh), 1981 (vs), 1925 (m)
$FeCo(CO)_6(PMe_3)(PPh_2)$ (**8c**) (THF): 2035 (w), 1994 (s), 1971 (vs), 1950 (m, sh), 1935 (m, sh)
$FeCo(CO)_5[P(OMe)_3]_2(PPh_2)$ (**9a**) (THF): 2025 (w), 1965 (vs), 1943 (s), 1913 (m)
$FeCo(CO)_5(PMe_3)_2(PPh_2)$ (**9b**) (THF): 1980 (m), 1949 (s), 1916 (vs), 1903 (m, sh)
$FeCo(CO)_7(PMe_3)(PPh_2)$ (**11**) (THF): 2053 (w), 2029 (s), 1987 (vs), 1978 (vs), 1955 (m), 1928 (s, sh), 1922 (vs)
$[Na(THF)_n][FeCo(CO)_6(PPh_2)]$ (**12**) (THF): 2005 (s), 1950 (vs), 1916 (vs), 1905 (vs, sh), 1856 (m)
[Na(18-crown-6)][$FeCo(CO)_6(PPh_2)$] (**12′**) (THF): 2004 (m), 1948 (s), 1915 (s), 1886 (vs)
$[Na(THF)_n]_2[FeCo(CO)_6(PPh_2)]$ (**13**) (THF): 2017 (m), 1967 (s), 1887 (vs)

[a] Underlined absorptions for **5a,b** are due to the cation.

Table III. ESR Parameters of $Fe_2(CO)_{7-n}L_n(\mu\text{-}PPh_2)$ Radicals and Their 35e CO Adducts in THF

complex	no.	no. of e	T, °C	g	a(P), G	a(P_1), G	a(P_2), G
$Fe_2(CO)_7(PPh_2)$[a]	**1**	33	−70	2.0520	23.4		
$Fe_2(CO)_8(PPh_2)$[b]	**3**	35	−70	2.0043	1.73		
$Fe_2(CO)_7(PPh_2)$	**1**	33	−20	2.0514	23.1		
$Fe_2(CO)_6(PPh_3)(PPh_2)$	**2a**	33	−20	2.0483	21.1	<2	
$Fe_2(CO)_6(PPh_3)_2(PPh_2)$	**3c**	35	−40	2.0283	10.9	3.8	3.8
$Fe_2(CO)_6(PMe_3)(PPh_2)$	**2b**	33	−20	2.0491	21.2	<2	
$Fe_2(CO)_5(PMe_3)_2(PPh_2)$	**4a**	33	−20	2.0515	22.2	7.2	<2
$Fe_2(CO)_5(PMe_3)_2(PPh_2)$[c]	**4a′**	33	−20	ca. 2.049	ca. 22.0	ca. 22.0	<2
$Fe_2(CO)_6(PMe_3)_2(PPh_2)$	**3d**	35	−20	2.0183	8.73	3.50	3.50
$Fe_2(CO)_6(PEt_3)(PPh_2)$[a]	**2c**	33	−70	2.0498	21.6	<2	
$Fe_2(CO)_7(PEt_3)(PPh_2)$[b]	**3a**	35	−70	2.0214	10.3	12.8	
$Fe_2(CO)_6(PEt_3)(PPh_2)$	**2c**	33	−20	2.0491	21.0	<2	
$Fe_2(CO)_5(PEt_3)_2(PPh_2)$	**4b**	33	−20	2.0518	23.2	<2	<2
$Fe_2(CO)_5(PEt_3)_2(PPh_2)$[c]	**4b′**	33	−20	ca. 2.049	ca. 20.0	ca. 20.0	<2
$Fe_2(CO)_6(PEt_3)_2(PPh_2)$	**3e**	35	−20	2.0236	10.1	4.1	4.1
$Fe_2(CO)_6[P(OMe)_3](PPh_2)$[a]	**2d**	33	−80	2.0500	22.2	<2	
$Fe_2(CO)_7[P(OMe)_3](PPh_2)$[b]	**3b**	35	−80	2.0130	6.5	13.2	
$Fe_2(CO)_6[P(OMe)_3](PPh_2)$	**2d**	33	−20	2.0500	21.9	<2	
$Fe_2(CO)_5[P(OMe)_3]_2(PPh_2)$	**4c**	33	−20	2.0499	22.7	5.5	<2
$Fe_2(CO)_5[P(OMe)_3]_2(PPh_2)$[c]	**4c′**	33	−20	2.0496	20.9	27.6	<2
$Fe_2(CO)_6[P(OMe)_3]_2(PPh_2)$	**3f**	35	−20	2.0241	9.5	6.1	6.1

[a] In pentane. [b] In CO-saturated pentane. [c] Approximate ESR parameters since the spectrum is obscured by that of the major stereoisomer.

give the monosubstituted 33e radicals $Fe_2(CO)_6L(\mu\text{-}PPh_2)$ (**2a–d**; L = PPh_3, PMe_3, PEt_3, $P(OMe)_3$) as dark green crystalline solids (Scheme II). Complexes **2a–d** were characterized by elemental analyses, by IR and ESR spectroscopy (Tables I–III), and, for **2d**, by a single-crystal X-ray diffraction study.

The molecular structure of **2d**, shown in Figure 1, consists of $Fe(CO)_3L$ and $Fe(CO)_3$ fragments bridged by a PPh_2 group and an Fe–Fe bond (2.6159 (9) Å), with L trans to the PPh_2 bridge (P2–Fe1–P1 = 164.04 (4)°). Including the metal–metal bond, the coordination geometries are distorted octahedral and trigonal bipyramidal about the six- and five-coordinate metal centers, with the axial ligands trans to the PPh_2 bridge bent toward the metal–metal bond (P2–Fe2–C6 = 155.6 (1)°). The steric bulk of the phosphite ligand increases these trans angles relative to the unsubstituted heterobimetallic analogue,[2] $FeCo(CO)_7(\mu\text{-}PPh_2)$, in which P–Fe–C = 156.27 (6)°, P–Co–C = 139.78 (5)°, and Fe–Co = 2.652 (1) Å.

The structures of the remaining monosubstituted derivatives, **2a–c**, are analogous to that of **2d**, judging by the similarity of the solution IR spectra for the entire series (Table II).

The reaction of **1** with more than 1 equiv of tertiary phosphorus ligands is more complex and involves several species existing in equilibrium with each other and with the CO liberated in the substitution process. The latter can add to the various substituted derivatives of **1** to give 35e adducts much as CO adds to the parent complex to give the 35e adduct **3** (eq 1). This process can be enhanced by deliberate addition of CO. Under these circumstances, pure materials were not isolated, and the characterization of the products was based on solution ESR and, to a lesser extent, IR investigations. These studies show that for L = PPh_3 and PEt_3 substitution effectively stops with the incorporation of two phosphorus ligands. For L = PMe_3 and $P(OMe)_3$ trisubstitution occurs readily but leads to diamagnetic ionic products by disproportionation reactions (see below). A trisubstituted diiron radical was observed only with the sterically less demanding diethylphosphido analogue of **1** (see below). The species identified by ESR in the following section are shown in Scheme II.

ESR Characterization of $Fe_2(CO)_{7-n}L_n(\mu\text{-}PPh_2)$ (2a–d and 4a–c) and of the CO Ligand Adducts 3a–f. The solution ESR spectra of **2a–d** in pentane or THF are quite similar to the spectrum of the unsubstituted parent complex **1** and consist of doublets (20–24 G, g ca. 2.05, Table III) from coupling of the unpaired electron to the ^{31}P nucleus of the phosphido bridge. The narrowest line widths of about 4 G are observed at ca. −70 °C

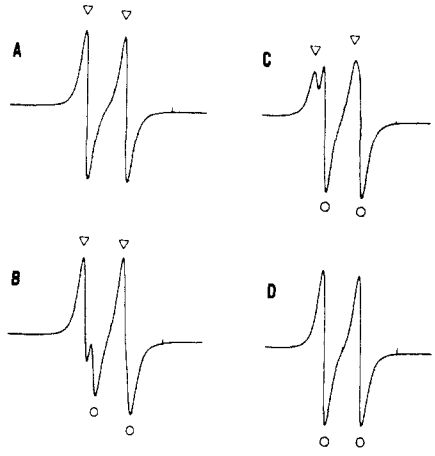

Figure 2. ESR spectral changes recorded at −20 °C attending the addition of n equiv of PPh_3 to a 0.01 M THF solution of $Fe_2(CO)_7(\mu\text{-}PPh_2)$ at room temperature: (A) $n = 0$; (B) $n = 0.5$; (C) $n = 1$; (D) $n = 1.5$.

in pentane and at ca. −20 °C in THF. As noted previously,[1] no coupling to L is observed as the SOMO is localized on the five-coordinate Fe center while L is bonded to the six-coordinate Fe center. Powder spectra in organic glasses (3-methylpentane and 2-methyltetrahydrofuran) at −173 °C also fail to show a hyperfine interaction with the P atom of the added ligand and reveal three distinct principal components of the **g** and **A**(^{31}P) tensors appropriate for the low symmetry of these organometallic radicals (cf. Figure 4A and ref 1).

Since the isotropic ESR spectra of **1** and **2a–d** are very similar doublets, careful measurements of the g factor and of the ^{31}P splitting were needed to distinguish the monosubstituted derivatives from the parent complex. Figure 2, for example, shows the spectral changes that occur as 0 (A), 0.5 (B), 1 (C), and 1.5 (D) equiv of PPh_3 (in THF) are added to a 10^{-2} M THF solution of **1**. About 1.5 equiv of the ligand were required for complete conversion of **1** (doublet marked with triangles) into **2a** (doublet marked with circles), suggesting the equilibrium shown below. Indeed, when solutions of **2a** are saturated with CO, **2a** is converted back to **1**. In the presence of CO, the 35e adduct **3** (eq 1) is also observed

$$\underset{\mathbf{1}}{Fe_2(CO)_7(\mu\text{-}PPh_2)} + PPh_3 \rightleftarrows \underset{\mathbf{2a}}{Fe_2(CO)_6(PPh_3)(\mu\text{-}PPh_2)} + CO \quad (2)$$

(Table III), but no evidence was obtained for a direct addition of CO to **2a** to form the monosubstituted 35e $Fe_2(CO)_7(PPh_3)(\mu\text{-}PPh_2)$, in contrast to the behavior of the PEt_3 and $P(OMe)_3$ analogues (see below). Evidently this 35e species readily loses the PPh_3 ligand to regenerate the starting complex **1**, which can then add another CO (eq 1).

Further addition of PPh_3 in the above titration beyond 1.5 equiv produced no further changes until about 4 equiv had been added when a very weak doublet of triplets spectrum (10.9 and 3.8 G) appeared at higher field with a small g factor (2.0283) characteristic of 35e species such as **3**. CO substitution with PPh_3 in **1** thus stops at monosubstitution: in the presence of sufficient PPh_3, however, a small equilibrium concentration of the disubstituted 35e $Fe_2(CO)_6(PPh_3)_2(\mu\text{-}PPh_2)$ (**3c**) is formed. The instability of **3c** in the absence of added PPh_3 was also demonstrated by the oxidation of the anion $[Fe_2(CO)_6(PPh_3)_2(\mu\text{-}PPh_2)]^-$ (see below) at 25 °C using $[Cp_2Fe]BF_4$ or $AgBF_4$, which gives only the monosubstituted 33e complex **2a** by PPh_3 loss. For **3c** we assign the doublet splitting to the bridging ^{31}P atom and the triplet splitting to the ^{31}P atoms of two terminal PPh_3 ligands, one on each Fe atom probably trans to the phosphido bridging group, in a structure such as that of **3**. Analogous 35e disubstituted complexes, **3d–f**, were also observed for other phosphorus ligands (see below and Scheme II).

Substitution of CO in **1** with the less bulky phosphorus ligands PMe_3, PEt_3, and $P(OMe)_3$ is more complex and gives rise to several paramagnetic substitution products as well as to several

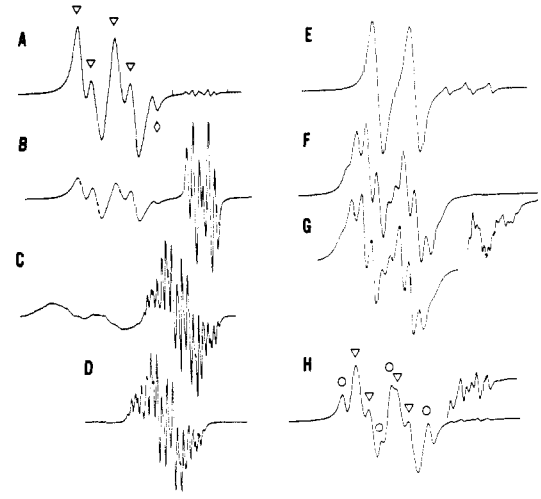

Figure 3. (A) ESR spectrum at −20 °C obtained after addition of 3 equiv of PMe_3 to a 0.01 M THF solution of $Fe_2(CO)_7(\mu\text{-}PPh_2)$ at room temperature. (B) ESR spectrum at −30 °C obtained by saturating with CO a dilute toluene solution of $Fe_2(CO)_5(PMe_3)_2(\mu\text{-}PPh_2)$. (C) Same with ^{13}CO. (D) Computer simulation of spectrum in C. (E) Spectrum at −50 °C obtained by saturating with CO a dilute pentane solution of $Fe_2(CO)_6(PEt_3)(\mu\text{-}PPh_2)$. (F) Same with ^{13}CO. (G) Computer simulation of spectrum in F. (H) ESR spectrum at −20 °C obtained after addition of 10 equiv of $P(OMe)_3$ to a 0.01 M THF solution of $Fe_2(CO)_7(\mu\text{-}PPh_2)$ at room temperature.

diamagnetic disproportionation products. Monitoring the titration of **1** with PMe_3 in THF by ESR, as described above for PPh_3 (cf. Figure 2), again shows the gradual transformation of the doublet for **1** to the doublet of monosubstituted **2b** (Table III). Further addition of PMe_3 produces more complicated spectra, precipitation of insoluble material (see later), and the change of the green color characteristic of **1** and **2a–d** to yellow-brown. The ESR spectrum obtained on addition of 3 equiv of PMe_3 in THF (0.01 M solutions) no longer shows the presence of the monosubstituted derivative and reveals three new species (Figure 3A). The major species gives rise to a doublet of doublets (triangles in Figure 3A) assigned to the disubstituted 33e derivative $Fe_2(CO)_5(PMe_3)_2(\mu\text{-}PPh_2)$ (**4a**). Evidently, only one ^{31}P nucleus of the two PMe_3 ligands in this complex is visible by ESR and gives rise to the smaller doublet splitting (7.2 G). The larger doublet splitting (22.2 G) is associated with the phosphido ^{31}P nucleus, since it has a value comparable to that of the phosphido ^{31}P nuclei of complex **1** and **2b** (Table III). The line marked with a diamond in Figure 3A is always present in about the same ratio relative to the major doublet of doublets for several stoichiometries of **1** and PMe_3. Consequently, we do not believe that it belongs to a trisubstituted derivative but rather to another stereoisomer **4a′** of the major disubstituted derivative **4a**. By comparison with the results for PEt_3, where this point is clearer, we conclude that this line is part of a triplet or a doublet of doublets of comparable splitting (ca. 22 G) whose remaining lines nearly coincide with the first and third lines of the major disubstituted derivative (first and third triangle from the left in Figure 3A) and would thus not be discernible. By analogy with **4a**, we believe that the two almost equivalent ^{31}P atoms, which give rise to this hyperfine splitting, are those of the phosphido bridge and of one of the two PMe_3 ligands. The P atom of the remaining PMe_3 ligand again has a splitting too small to be resolved.

The third species formed in the reaction of **1** with 3 equiv of PMe_3 in THF gives rise to a doublet of triplets at higher field (8.7 and 3.5 G, respectively, $g = 2.0183$, Figure 3A) analogous to that observed for **3c** with PPh_3. The smaller g value and narrower line width compared to the 33e complexes clearly suggest the 35e species **3d** with two PMe_3 ligands replacing the terminal CO ligands on each Fe atom trans to the phosphido bridge as shown in eq 3. The assignment of this species as $Fe_2(CO)_6(PMe_3)_2(\mu\text{-}PPh_2)$ (**3d**) is corroborated by the observation that the concentration of **3d** is enhanced at the expense of **4a** and **4a′** by saturating the solution with CO, as shown in Figure 3B (using

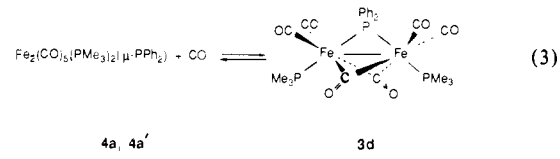

(3)

4a, 4a′ 3d

toluene as solvent in which **3d** is more soluble). Thus, the 33e and 35e disubstituted PMe_3 derivatives are in equilibrium with CO (eq 3). This equilibrium is temperature dependent and shifts in the direction of the 35e derivative **3d** as the temperature is lowered to ca. −30 °C, below which **3d** is almost completely insoluble.

The spectrum obtained when a dilute toluene solution of the two isomers of $Fe_2(CO)_5(PMe_3)_2(\mu\text{-}PPh_2)$ (**4a** and **4a′**) is saturated with ^{13}CO (99%, Figure 3C) supports the structure proposed for **3d**. The complicated spectrum, which replaces the doublet of triplets in Figure 3B, can be computer simulated (Figure 3D) in terms of four equivalent ^{13}C atoms (2.26 G, terminal CO's), two equivalent ^{31}P atoms (3.51 G, PMe_3 ligands), a unique ^{31}P atom (9.17 G, phosphido bridge), and two strongly interacting ^{13}C atoms (8.86 G), which must be associated with the two bridging CO ligands. The ESR parameters for **3d** indicate that the PMe_3-disubstituted 35e radical is electronically quite similar to the unsubstituted parent complex **3**.

Additional support for the presence of bridging CO's in **3d** was obtained by IR spectroscopy. Although equilibrium 3 precludes the observation of the IR bands for **3d** at 25 °C, we exploited the low solubility of **3d** in toluene at low temperatures to obtain a yellow-brown precipitate. A Nujol mull IR spectrum of this precipitate shows bands for **4a** and **4a′** and four additional bands (2036 (w), 2013 (m, sh), 2010 (m), and 1842 (s, br) cm^{-1}), which must be assigned to **3d**. The band at 1842 cm^{-1} is appropriate for the bridging CO's by comparison with $Fe_2(CO)_9$ (1821 cm^{-1})[31] and $(\eta\text{-}C_5H_5)_2Fe_2(\mu\text{-}CO)_3$ (1811 cm^{-1}).[32]

A slightly different substitution behavior was observed with PEt_3. If a pentane solution of the monosubstituted derivative **2c** is briefly saturated with CO, a new doublet of doublets spectrum (12.8 and 10.3 G, g = 2.0214, Figure 3E) is observed at higher field showing couplings to two distinct ^{31}P nuclei. This spectrum can be assigned to the PEt_3-monosubstituted 35e species **3a** formed by addition of CO to **2c** (eq 4). Evidently, PEt_3 is more tightly

$$\underset{\textbf{2c}}{Fe_2(CO)_6(PEt_3)(\mu\text{-}PPh_2)} + CO \rightleftarrows \underset{\textbf{3a}}{Fe_2(CO)_7(PEt_3)(\mu\text{-}PPh_2)} \quad (4)$$

bound than PPh_3 since the latter was displaced by CO in a similar experiment. The addition of CO to **2c** is again a temperature-dependent equilibrium, with lower temperatures favoring the formation of the 35e adduct **3a** at the expense of **2c**. We assign the larger of the two doublet splittings (12.8 G) to the P atom of the PEt_3 ligand since it is appreciably temperature dependent and the smaller (10.3 G), which is invariant with temperature, to the bridging phosphorus atom. This is because a temperature-dependent coupling requires motions of wide amplitude, which are clearly more likely for terminal ligands than for bridging ligands. A 12.8-G phosphorus coupling for the PEt_3 ligand is surprising in view of the 3.5- and 4.1-G splittings for the disubstituted analogues **3d,e** in which the phosphorus ligands are presumably trans to the phospido bridge. We have also noticed that the g factor of **3a** is remarkably solvent and temperature dependent: 2.0214 in pentane and 2.0261 in toluene at −50 °C with intermediate values in mixtures of the two solvents. We suggest that the spectrum of **3a** arises from a rapidly equilibrating mixture of the two possible stereoisomers, which differ from each other by the orientation of the PEt_3 ligand relative to the phosphido bridge, each having a different g factor and ^{31}P coupling. The molar fractions of the different conformers are evidently temperature and solvent dependent, hence, the temperature dependence of the ^{31}P coupling and the solvent dependence of the g factor.

When a pentane solution of **2c** is saturated with 99% ^{13}CO, the spectrum shown in Figure 3F is observed when all original CO ligands of **2c** are replaced with ^{13}CO. The additional hyperfine structure brought about by ^{13}C enrichment of **3a** (inset in Figure 3F) is unfortunately too complicated to be analyzed and provides no additional information. The most obvious change in Figure 3F compared to that in Figure 3E, however, is the new structure acquired by each line of the doublet for the monosubstituted 33e **2c**. A computer simulation (Figure 3G) confirms that this structure is a binomial sextet, indicating the presence of five equivalent ^{13}C nuclei (5.7 G), as found previously for the parent complex **1**. This observation confirms that the PEt_3 ligand in **2c** is situated trans to the phosphido bridge on the six-coordinate iron where it does not interfere with the fluxional behavior of the equatorial CO ligands. Unfortunately, we were not able to establish if the exchange process could be frozen out since below −50 °C severe line broadening obliterates any effect due to intramolecular ^{13}CO exchange.

The reaction of **1** with more than 2 equiv of PEt_3 leads, as with PMe_3, to a mixture of disubstituted radicals. The spectrum of the 33e disubstituted radical $Fe_2(CO)_5(PEt_3)_2(\mu\text{-}PPh_2)$ (**4b**) is now a broad doublet (23.2 G); only the phosphido ^{31}P nucleus gives a resolvable hyperfine structure, and the ^{31}P couplings of the two PEt_3 ligands only broaden each line. At higher field, as in the case of PMe_3, there is the resonance of the 35e CO adduct $Fe_2(CO)_6(PEt_3)_2(\mu\text{-}PPh_2)$ (**3e**) consisting of a doublet of triplets (10.1 and 4.1 G, respectively). In addition there is a weaker line, similar to the line marked with a diamond in Figure 3A, which can now be related to two shoulders, quite prominent at −40 °C. The weak line and the two shoulders complete a triplet appropriate for two equivalent or almost equivalent ^{31}P atoms. We assign again this weaker spectrum to a stereoisomer of the major 33e disubstituted complex on the grounds that it is present in the same relative concentration for several stoichiometries of **1** and PEt_3. No ESR evidence was obtained for further substitution after introduction of two PEt_3 ligands.

Monosubstitution with $P(OMe)_3$ is straightforward and affords spectra for the 33e (doublet, Table III) and 35e (doublet of doublets, Table III) monosubstituted radicals **2d** and **3b**. The latter is obtained after addition of CO. Addition of more than 1 equiv of $P(OMe)_3$ to **1** yields complicated spectra; some simplification occurs when a large excess of $P(OMe)_3$ is added. The spectrum of Figure 3H, obtained on addition of 10 equiv of $P(OMe)_3$ to **1** in THF (0.01 M), can be interpreted in terms of only disubstituted radicals. The doublet of doublets marked with triangles belongs to the major 33e disubstituted derivative **4c**, and the doublet of doublets marked with circles belongs to the less abundant stereoisomer **4c′**, while the weak doublet of triplets at higher field belongs to the 35e disubstituted complex **3f** (Table III). The interconversion of these species in the presence of CO and the observation of a temperature-dependent equilibrium as discussed above further support the assignment. Additional confirmation comes from the observation of an identical mixture of the two isomeric 33e disubstituted radicals when the diamagnetic 34e anion $\{Fe_2(CO)_6[P(OMe)_3]_2(\mu\text{-}PPh_2)\}^-$ (**7c**) is oxidized in THF with either $(Cp_2Fe)BF_4$ or $AgBF_4$.

The similarity of the IR spectra of **4a–c** supports the view that these disubstituted radicals are isostructural. No IR information was obtained for the minor isomers **4a′–c′** because of their low concentration in solution.

ESR Characterization of $Fe_2(CO)_{7-n}[P(OMe)_3]_n(\mu\text{-}PEt_2)$ Radicals and Their CO Ligand Adducts. While further substitution beyond disubstitution of coordinated CO with PMe_3 and $P(OMe)_3$ in $Fe_2(CO)_7(\mu\text{-}PPh_2)$ (**1**) leads to diamagnetic disproportionation products (see later), we have obtained ESR evidence for the formation of a $P(OMe)_3$-trisubstituted derivative of the related 33e complex $Fe_2(CO)_7(\mu\text{-}PEt_2)$. Trisubstitution in this complex is probably made possible by the lesser steric demands of the diethylphosphido bridge compared to those of the diphenylphosphido bridge in **1**. Except for the formation of a trisubstituted

(31) Fritz, H. P.; Paulus, E. F. *Z. Naturforsch., B: Anorg. Chem., Org. Chem., Biochem., Biophys., Biol.* **1963**, *18B*, 435.
(32) Hepp, A. F.; Blaha, J. P.; Lewis, C.; Wrighton, M. S. *Organometallics* **1984**, *3*, 174.

Table IV. ESR Parameters of $Fe_2(CO)_{7-n}[P(OMe)_3]_n(\mu\text{-}PEt_2)$ Radicals and Their 35e CO Adducts in Pentane

complex	no. of e	T, °C	g	a(P), G	$a(P_1)$, G	$a(P_2)$, G
$Fe_2(CO)_7(PEt_2)$[a]	33	−70	2.0515	22.8		
$Fe_2(CO)_7(PEt_2)$	33	−70	2.0526	23.2		
$Fe_2(CO)_8(PEt_2)$[b,c]	35	−90	2.0065	3.1		
$Fe_2(CO)_6[P(OMe_3)](PEt_2)$	33	−60	2.0507	21.8	<2	
$Fe_2(CO)_7[P(OMe)_3](PEt_2)$[b]	35	−60	2.0186	8.8	13.7	
$Fe_2(CO)_5[P(OMe)_3]_2(PEt_2)$	33	−50	2.0511	22.3	16.9	<2
$Fe_2(CO)_6[P(OMe)_3]_2(PEt_2)$	35	−30	2.0103	8.6	13.6	13.6
$Fe_2(CO)_4[P(OMe)_3]_3(PEt_2)$[d]	33	−30	2.0520	21.5	15.3	4.9

[a] In THF. [b] In CO-saturated pentane. [c] Under high-resolution conditions an additional splitting of 0.5 G due to two hydrogen atoms can be partially resolved. Two strongly interacting bridging ^{13}C nuclei (12.4 G) can be seen using ^{13}CO. [d] $a(P_3) < 2$ G.

Table V. ^1H NMR Spectroscopic Data[a]

complex	no.	chemical shift,[b] ppm: PPh_2	chemical shift,[b] ppm: L[b]
$[Fe_2(CO)_5(PMe_3)_3(PPh_2)]^+[Fe_2(CO)_8(PPh_2)]^-$	**5a**	7.54 (m, 4 H), 7.44 (ov m, 6 H) 7.87 (m, 4 H), 7.16 (m, 4 H), 7.11 (m, 2 H)	1.75, 1.17, 1.63 (d, 9, 9 H)
$\{Fe_2(CO)_5[P(OMe)_3]_3(PPh_2)\}^+\{Fe_2(CO)_6[P(OMe)_3]_2(PPh_2)\}^-$	**5b**	7.65 (m, 4 H), 7.39 (ov m, 6 H) 7.89 (m, 4 H), 7.19 (m, 4 H), 7.13 (m, 2 H)	3.83 (ov d, 27 H) 3.58 (d, 12, 18 H)
$Et_4N[Fe_2(CO)_6(PMe_3)(PPh_2)]$	**6b**	7.61 (m, 4 H), 7.23 (ov m, 6 H)	1.53 (d, 9.2, 9 H)
$Et_4N\{Fe_2(CO)_6[P(OMe)_3](PPh_2)\}$	**6c**	7.62 (m, 4 H), 7.25 (ov m, 6 H)	3.63 (d, 12, 9 H)
$Et_4N[Fe_2(CO)_6(PPh_3)_2(PPh_2)]$	**7a**	8.01 (m, 4 H), 7.20 (m, 4 H), 7.11 (m, 2 H)	7.61 (m, 12 H), 7.36 (ov m, 18 H)
$Et_4N[Fe_2(CO)_6(PMe_3)_2(PPh_2)]$	**7b**	7.90 (m, 4 H), 7.15 (m, 4 H), 7.07 (m, 2 H)	1.43 (d, 9.3, 18 H)
$Et_4N\{Fe_2(CO)_6[P(OMe)_3]_2(PPh_2)\}$	**7c**	7.90 (m, 4 H), 7.20 (m, 4 H), 7.13 (m, 2 H)	3.58 (d, 12, 18 H)
$FeCo(CO)_6(PPh_3)(PPh_2)$	**8a**	7.63 (m, 4 H), 7.35 (m, 4 H), 7.33 (m, 2 H)	7.62 (m, 6 H), 7.46 (m, 6 H), 7.44 (m, 3 H)
$FeCo(CO)_6[P(OMe)_3](PPh_2)$[c]	**8b**	7.80 (m, 4 He, 7.01 (m, 4 H), 6.95 (m, 2 H)	3.30 (d, 12, 9 H)
$FeCo(CO)_6[P(OMe)_3](PPh_2)$[c]	**8b′**	7.79 (m, 4 H), 6.99 (m, 4 H), 6.92 (m, 2 H)	3.43 (d, 12, 9 H)
$FeCo(CO)_6(PMe_3)(PPh_2)$	**8c**	7.67 (m, 4 H), 7.33 (ov m, 6 H)	1.79 (d, 10, 9 H)
$FeCo(CO)_6(PMe_3)(PPh_2)$	**8c′**	7.64 (m, 4 H), 7.35 (ov m, 6 H)	1.64 (d, 10, 9 H)
$FeCo(CO)_5[P(OMe)_3]_2(PPh_2)$	**9a**	7.68 (m, 4 H), 7.26 (ov m, 6 H)	3.78 (d, 12, 9 H), 3.50 (d, 12, 9 H)
$FeCo(CO)_5(PMe_3)_2(PPh_2)$	**9b**	7.65 (m, 4 H), 7.26 (ov m, 6 H)	1.72 (d, 9.7, 9 H), 1.56 (d, 9.3, 9 H)
$FeCo(CO)_6(PMe_3)_2(PPh_2)$	**10b**	7.86 (m, 4 H), 7.22 (ov m, 6 H)	1.61 (d, 10.8, 9 H), 1.53 (d, 9.8, 9 H)
$FeCo(CO)_7(PMe_3)(PPh_2)$	**11**	7.82 (m, 4 H), 7.33 (ov m, 6 H)	1.69 (d, 11, 9 H)

[a] Recorded at 25 °C in THF-d_8. Complexes **5b**, **6**, and **7** were run in CD_3CN. For **6** and **7** Et_4N^+ resonances are at δ 3.12 (q, $^3J_{HH}$ = 7.2 Hz, 8 H) and 1.18 (tt, $^3J_{HN}$ = 2.0 Hz, 12 H). [b] J_{HP} in hertz in parentheses. [c] Recorded in toluene-d_8.

derivative, CO substitution with $P(OMe)_3$ in $Fe_2(CO)_7(\mu\text{-}PEt_2)$ resembles that of $Fe_2(CO)_7(\mu\text{-}PPh_2)$. The ESR spectrum of the monosubstituted derivative shows no splitting from the ^{31}P atom of the added $P(OMe)_3$ ligand (Table IV). Its powder spectrum in a 3-methylpentane glass at −170 °C (Figure 4A) is similar to that of the unsubstituted parent and shows three distinct principal components of the **g** tensor (2.0933, 2.0325, 2.0248) and of the **A**(^{31}P) hyperfine tensor for the bridging ^{31}P atom (21.0, 26.4, and 19.1 G). The monosubstituted 35e CO adduct $Fe_2(CO)_7[P(OMe)_3](\mu\text{-}PEt_2)$ gives rise to a doublet of doublets (Figure 4B; 8.8 and 13.7 G) with a characteristically small g value (2.0186). We assign the larger splitting, which is temperature dependent, to the ^{31}P atom of the $P(OMe)_3$ ligand. Addition of 2 equiv of $P(OMe)_3$ to a pentane solution of $Fe_2(CO)_7(\mu\text{-}PEt_2)$ produces a doublet of doublets spectrum (Figure 4C; 22.3 and 16.9 G) for the disubstituted derivative $Fe_2(CO)_5[P(OMe)_3]_2(\mu\text{-}PEt_2)$ in which, once again, only one ^{31}P atom of the two $P(OMe)_3$ ligands interacts appreciably with the unpaired electron. Note that only one isomer is observed and that the ^{31}P hyperfine splittings resemble those of the minor disubstituted isomer in the PPh_2-bridged system. With $Fe_2(CO)_7(\mu\text{-}PPh_2)$ no further major spectral changes took place beyond this point. With $Fe_2(CO)_7(\mu\text{-}PEt_2)$, on the other hand, a new spectrum grows in immediately after addition of more than 2 equiv of $P(OMe)_3$. It seems reasonable, therefore, to assign it to trisubstituted $Fe_2(CO)_4[P(OMe)_3]_3(\mu\text{-}PEt_2)$. The spectrum obtained after addition of 4 equiv of $P(OMe)_3$ is shown in Figure 4D. The trisubstituted derivative gives rise to a multiplet consisting of three doublets of 21.5, 15.3, and 4.9 G confirmed by computer simulation (Figure 4D). Thus, only three of the four ^{31}P atoms of the molecule give rise to resolvable hyperfine structure. The weaker multiplet at higher field in Figure 4D is a triplet of doublets (13.6 and 8.6 G), and we assign it to the disubstituted 35e derivative $Fe_2(CO)_6[P(OMe)_3]_2(\mu\text{-}PEt_2)$ by comparison with the results for the diphenylphosphido-bridged analogues.

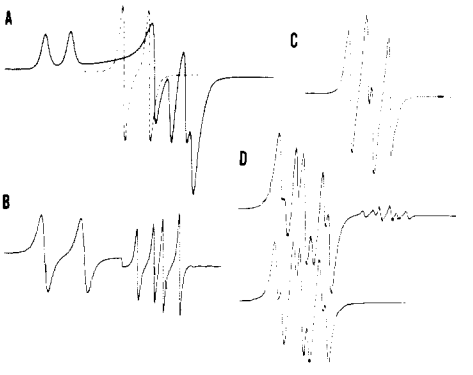

Figure 4. (A) Solution (dashed line) and solid-state ESR spectra of $Fe_2(CO)_6[P(OMe)_3](\mu\text{-}PEt_2)$ in 3-methylpentane at −70 and −170 °C, respectively. (B) ESR spectrum obtained when a dilute pentane solution of $Fe_2(CO)_6[P(OMe)_3](\mu\text{-}PEt_2)$ is saturated with CO. The step in the base line is caused by a change of instrumental gain. (C) ESR spectrum at −50 °C obtained when a dilute pentane solution of $Fe_2(CO)_7(\mu\text{-}PEt_2)$ is reacted with 2 equiv of $P(OMe)_3$ at room temperature. (D) Same as C with 4 equiv of $P(OMe)_3$ and computer simulation.

Formation of Disproportionation Products. When the reactions of **1** with excess PMe_3 and $P(OMe)_3$ in THF were monitored by IR and ESR spectroscopy, it became apparent that diamagnetic products were also formed. When the substitution reactions were performed in concentrated toluene solutions, these products were isolated in good yield and shown to be the complex salts $[Fe_2(CO)_5(PMe_3)_3(\mu\text{-}PPh_2)]^+[Fe_2(CO)_8(\mu\text{-}PPh_2)]^-$ (**5a**) and $\{Fe_2(CO)_5[P(OMe)_3]_3(\mu\text{-}PPh_2)\}\{Fe_2(CO)_6[P(OMe)_3]_2(\mu\text{-}PPh_2)\}$ (**5b**) (eq 5). The crude product in the $P(OMe)_3$ reaction contains the 34e trisubstituted cation along with unsubstituted, mono-, and disubstituted 36e anions. The latter predominates, and pure **5b** was obtained by recrystallization from THF–diethyl ether. Complexes **5a,b** were characterized by elemental analysis, by IR,

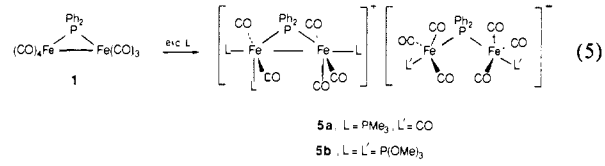

(5)

^1H and ^{31}P NMR spectroscopy (Tables V and VI), and, for **5a**, by a single-crystal X-ray diffraction study.

The molecular structure of **5a** consists of discrete dinuclear anions and cations. The structure of the 36e anion is identical with that determined previously[3] as the Et_4N^+ salt. The 34e cation, shown in Figure 5, consists of $Fe(CO)_2L_2$ and $Fe(CO)_3L$ fragments joined by a PPh_2 bridge and a metal–metal bond (Fe–Fe = 2.780 (2) Å), with one L on each Fe trans to the Fe–Fe bond (av P–Fe–Fe = 157.12 (8)°) and the third L trans to the PPh_2 bridge (P1–Fe–P3 = 151.1 (1)°). The substitution pattern thus resembles that observed[25] for $RuCo(CO)_4[(P(OMe)_3]_3(\mu\text{-}PPh_2)$, although both metal centers in the cation are six-coordinate. The Fe–P distances in the cation fall within a narrow range between 2.217 and 2.230 Å, except for the PMe_3 ligand trans to the PPh_2 bridge, for which Fe–P = 2.265 (2) Å. The Fe–P distances to the PPh_2 bridge (av = 2.325 (2) Å) in the anion are much larger.

Spectroscopic Characterization of the Disproportionation Products (5a,b). The IR spectra of **5a,b** provided little information about the structure of the cations because of overlap with the anion absorptions. The ^{31}P NMR spectrum of **5a** in THF-d_8 at −40 °C consists of a singlet at 58.0 ppm characteristic of the "open" PPh_2 bridge[33] in $[Fe_2(CO)_8(PPh_2)]^-$, a doublet of doublets ($^2J_{PP}$ = 31, 22 Hz) at 160.1 ppm from the "closed" PPh_2 bridge, and one singlet and two doublet PMe_3 resonances in $[Fe_2(CO)_5(PMe_3)_3(PPh_2)]^+$. The observed values of the two-bond P–P coupling constants (two medium, one small) are not easily understood[34] in terms of the observed solid-state structure of the cation unless $^2J_{PP} < 1$ Hz between the PPh_2 bridge and the PMe_3 ligand trans to it. A more likely proposal consists of an alternative stereoisomer for the cation of **5a** in solution, which consists of two PMe_3 ligands trans to the PPh_2 bridge and one PMe_3 ligand trans to the Fe–Fe bond on the six-coordinate Fe center. Note that this structure is related to that observed for **5a** in the solid state by a rotation of the $Fe(CO)_2L$ vertex with respect to the FePFe bridge plane. The ^{31}P NMR spectrum of **5a** at 25 °C shows broadening of the two PMe_3 doublet resonances, which become broad singlets at 55 °C. The nature of this fluxional process has not yet been elucidated. The ^{31}P NMR spectrum of **5b** is more complex. The triplet and doublet resonances at 71.8 and 202.1 ppm, respectively ($^2J_{PP}$ = 55 Hz), are easily assigned to the PPh_2 bridge and the two $P(OMe)_3$ ligands trans to it in the 36e anion (see later). The resonances of the cation are complicated by their sizable P–P spin couplings and small chemical shift differences, which give rise to second-order effects. In addition, ^{31}P spectra of **5b** at lower temperatures again point to an ill-defined fluxional process. In acetone-d_6 at 50 °C, however, the spectrum is readily analyzed. Thus, the PPh_2 bridge couples to all three $P(OMe)_3$ ligands with $^2J_{PP}$ values of 81, 26, and 9 Hz. Taking into account the ratio of coupling constants involving $P(OR)_3$ vs PR_3 of about 1.5–2.0 observed previously[35] and in this work (Table VI), the $^2J_{PP}$ values for the cation of **5b** appear now to be more consistent with the stereoisomer observed for **5a** in the solid state with one $P(OMe)_3$ ligand trans and two cis to the PPh_2 bridge.

Ligand Substitution Reactions of $Et_4N[Fe_2(CO)_7(\mu\text{-}PPh_2)]$ (6). The reactions of $Et_4N[Fe_2(CO)_6(\mu\text{-}CO)(\mu\text{-}PPh_2)]$ with PPh_3, PMe_3, and $P(OMe)_3$ proceed slowly at 25 °C to give the disubstituted 36e products $Et_4N[Fe_2(CO)_6L_2(\mu\text{-}PPh_2)]$ (**7a–c**) as pale yellow crystalline solids (eq 6). Monitoring the reactions by ^{31}P NMR spectroscopy using 1, 2, and 5 equiv of L showed only the presence of **7a–c**. The products were characterized by elemental

(33) The ^{31}P NMR chemical shifts of PPh_2 resonances in 36e dinuclear complexes are often found 50–150 ppm upfield of their 34e counterparts. Cf.: Carty, A. J. *Adv. Chem. Ser.* **1982**, *No. 196*, 163.
(34) Verkade, J. G. *Coord. Chem. Rev.* **1972**, *9*, 1.
(35) Pidcock, A. *Adv. Chem. Ser.* **1982**, *No. 196*, 1.

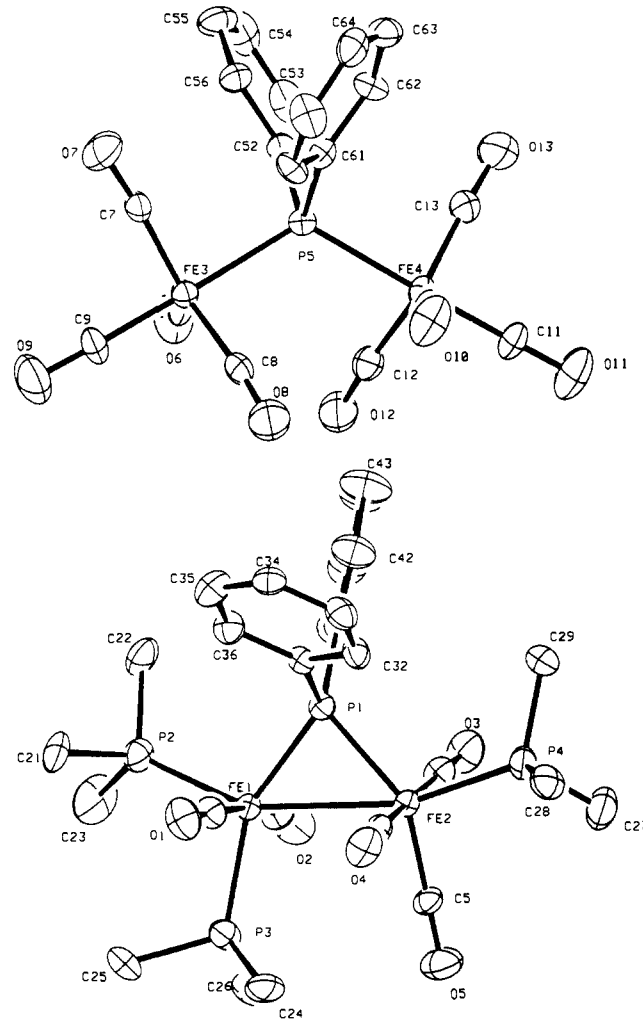

Figure 5. Molecular structure of $[Fe_2(CO)_5(PMe_3)_3(\mu\text{-}PPh_2)]^+[Fe_2(CO)_8(\mu\text{-}PPh_2)]^-$ (**5a**). Hydrogen atoms are omitted for clarity.

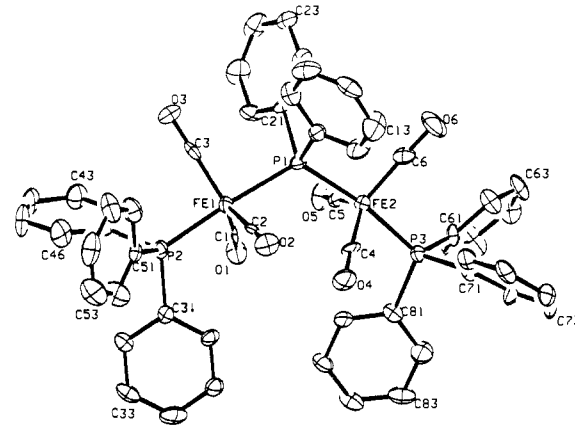

Figure 6. Molecular structure of the $[Fe_2(CO)_6(PPh_3)_2(\mu\text{-}PPh_2)]^-$ anion of **7a**. Hydrogen atoms are omitted for clarity.

Scheme III

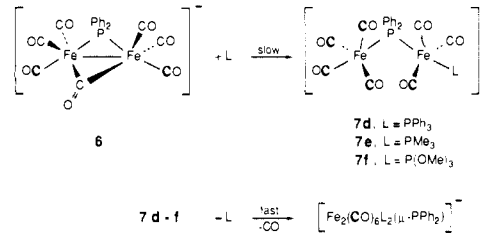

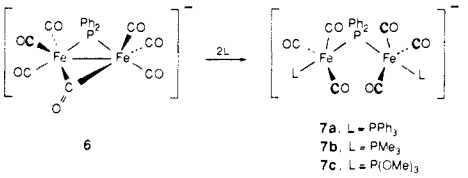

(6)

analysis, by IR and NMR spectroscopy, and, for **7a**, by a single-crystal X-ray diffraction study.

The molecular structure of **7a**, shown in Figure 6, consists of two $Fe(CO)_3L$ fragments connected by a PPh_2 bridge, with both PPh_3 ligands trans to the PPh_2 bridge (P–Fe–P (av) = 173.2 (1)°). Both Fe centers are trigonal bipyramidal, with the equatorial CO ligands staggered along the P–Fe–P–Fe–P chain, as observed previously for the unsubstituted anion.[3] The average Fe–P distance to the PPh_2 bridge (2.304 (3) Å) is shorter than that in the unsubstituted anion (2.323 (1) Å), while the Fe–P–Fe angle (118.6 (1)°) is almost identical (118.92 (4)°). The average Fe–P distance to the PPh_3 ligands (2.195 (3) Å) is significantly shorter than that to the PPh_2 bridge, unlike those reported previously[36-38] for the 34e complexes $FeIr(CO)_5(PPh_3)_2(\mu\text{-}PPh_2)$ (Fe–P(PPh_3) = 2.248 (2) and Fe–P(PPh_2) = 2.239 Å), $Fe_2(CO)_5(PPh_3)(\mu\text{-}C_2Ph)(\mu\text{-}PPh_2)$ (Fe–P(PPh_3) = 2.274 (1) and Fe–P(PPh_2) = 2.212 (1) Å), and $Fe_2(CO)_5(PPh_2Me)(\mu\text{-}C(O)Me)(\mu\text{-}PPh_2)$ (Fe–P(PPh_2Me) = 2.268 (2) and Fe–P(PPh_2) = 2.200 (2) Å).

While complexes **7a–c** are unchanged after 12 h in refluxing acetonitrile, photolysis for 1–2 h results in ligand loss and formation of the substituted 34e complexes $Et_4N[Fe_2(CO)_4L_2(\mu\text{-}CO)(\mu\text{-}PPh_2)]$ (**6a–e**) characterized by IR and ^{31}P NMR spectroscopy (eq 7). The PPh_3 analogue **7a** loses PPh_3 exclusively,

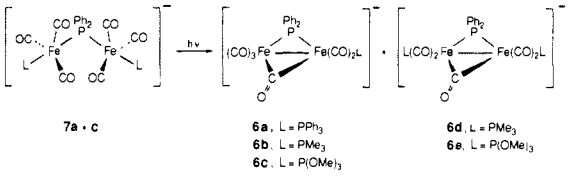

(7)

and the thermal back-reaction is so slow ($t_{1/2}$ > 14 days) at 25 °C that **6a** can be ruled out as an intermediate in the formation of **7a** from the $[Fe_2(CO)_7(PPh_2)]^-$ anion. With the PMe_3 and $P(OMe)_3$ analogues, CO ligand loss is competitive with loss of L, giving rise to both mono- (**6b,c**) and disubstituted (**6d,e**) 34e anions, with the former predominating. The thermal back-reactions of **6b,d** with L are also slow, but if L is removed from the photolysis reaction products, followed by treatment with CO, the monosubstituted products react to give the monosubstituted 36e anions $Et_4N[Fe_2(CO)_7L(\mu\text{-}PPh_2)]$ (**7d–f**) characterized by ^{31}P NMR spectroscopy. Although quantitative data were not obtained, reaction of **7d–f** with L to give the disubstituted 36e anions **7a–c** is rapid, supporting the mechanistic scheme shown in Scheme III.

Spectroscopic Characterization of $Et_4N[Fe_2(CO)_5L_2(\mu\text{-}PPh_2)]$ (6a–e) and of the CO Ligand Adducts 7a–f. While the analytical data indicated only ca. 95% purity for complexes **7a,c**, the relative proportions of the elements are correct, and the spectroscopic data confirm that **7a–c** are isostructural. The infrared spectra of **7a–c** contained only terminal CO absorptions, consistent with the structure determined for **7a**. The infrared spectrum of $Et_4N[Fe_2(CO)_6(PPh_3)(\mu\text{-}PPh_2)]$ (**6a**) contains an absorption (1719 cm^{-1}) for a bridging CO, as observed previously for unsubstituted **6** (1737, 1710 cm^{-1} in THF solution).[3] The ^1H NMR spectra also distinguish between the metal–metal bonded 34e anions **6a–e** and their 36e CO adducts **7a–f** as the chemical shift dispersion of the PPh_2 bridge protons is much greater for the latter (Table V). The two classes are also easily distinguished by ^{31}P NMR spectroscopy as the resonances for the open PPh_2 bridges are about 50 ppm upfield from their closed PPh_2-bridged counterparts.[33] The two-bond P–P coupling constants between L and the PPh_2 bridge are 20–30 Hz for L = PPh_3 and PMe_3 and 55–70 Hz for L = $P(OMe)_3$ for all the complexes except the disubstituted 34e anions, **6d–e**, for which $^2J_{PP}$ is reduced by half. Low-temperature ^{31}P NMR studies in acetone-d_6 show no spectral change except for **6d,e**, which exhibit fluxional behavior. Unfortunately, this fluxional process is not frozen out sufficiently at the low-temperature solvent limit (−90 °C) to permit a detailed analysis. If we assume that the $^2J_{PP}$ values observed for **6a–c** and **7a–f** arise from a trans orientation of L and the PPh_2 bridge, as observed in the solid state for **7a**, then the smaller coupling constants observed for **6d,e** may result from exchange averaging between the trans isomer with "normal" values of $^2J_{PP}$ and another isomer with L cis to the PPh_2 bridge and with small values of $^2J_{PP}$.

Scheme IV

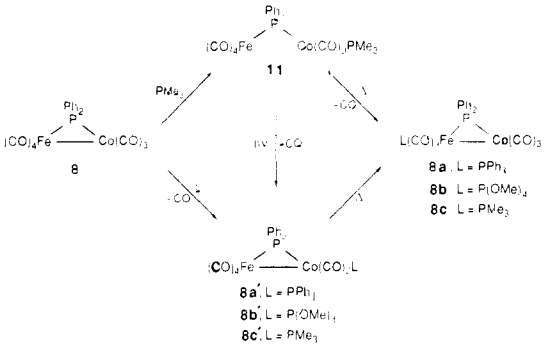

Ligand Substitution Reactions of $FeCo(CO)_7(\mu\text{-}PPh_2)$ (8). The reaction between $FeCo(CO)_7(\mu\text{-}PPh_2)$ and 1 or more equiv of PPh_3 in THF at 25 °C gives the 34e monosubstituted product $FeCo(CO)_6(PPh_3)(\mu\text{-}PPh_2)$ (**8a**) isolated as red-brown crystals. Monitoring the above reactions by ^{31}P NMR spectroscopy indicates the buildup of an initial substitution product **8a′**, which isomerizes to the observed product **8a** (Scheme IV). With 1 equiv of $P(OMe)_3$, formation of the kinetic product **8b′** is accompanied by ca. 10% of the disubstituted complex $FeCo(CO)_5[P(OMe)_3]_2(\mu\text{-}PPh_2)$ (**9a**). Heating complex **8b′** at 60 °C for several hours then leads to the thermodynamic isomer **8b**; the mechanism of this isomerism is unknown. Using 2 or more equiv of $P(OMe)_3$ affords **9a**, isolated as a brown solid, and its 36e counterpart $FeCo(CO)_6[P(OMe)_3]_2(\mu\text{-}PPh_2)$ (**10a**; eq 8). Further substitution

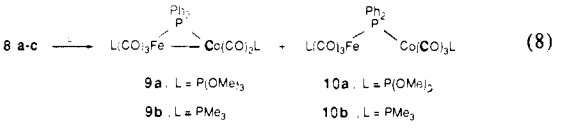

(8)

is slow (weeks) at 25 °C, and the products were not characterized. The addition of 1 equiv of PMe_3 to $FeCo(CO)_7(\mu\text{-}PPh_2)$ in toluene yields orange crystals of 36e $FeCo(CO)_7(PMe_3)(\mu\text{-}PPh_2)$ (**11**; Scheme IV). While thermolysis of **11** gives the thermodynamic monosubstituted 34e product $FeCo(CO)_6(PMe_3)(\mu\text{-}PPh_2)$ (**8c**), photolysis of **11** at 0 °C leads exclusively to the kinetic product **8c′** (Scheme IV). Using 2 or more equivalents of PMe_3 in THF again leads to both 34e and 36e disubstituted products **9b** and **10b** (eq 8). Further substitution is slow at 25 °C and was not investigated. Complexes **8–11** were characterized primarily by IR and ^{31}P NMR spectroscopy, with selected complexes isolated and characterized by elemental analysis and ^1H NMR spectroscopy. Complex **9a** was also characterized by a single-crystal X-ray diffraction study.

The molecular structure of **9a** (Figure 7) consists of $Fe(CO)_3L$ and $Co(CO)_2L$ fragments joined by a PPh_2 bridge and a metal–metal bond (Fe–Co = 2.706 (1) Å), with the L on Fe trans to the PPh_2 bridge (P1–Fe–P2 = 170.75 (8)°) and the L on Co trans to the Fe–Co bond (Fe–Co–P3 = 143.71 (4)°). The structure is thus similar to that determined previously[39] for

(36) Roberts, D. A.; Steinmetz, G. R.; Breen, M. J.; Shulman, P. M.; Morrison, E. D.; Duttera, M. R.; DeBrosse, C. W.; Whittle, R. R.; Geoffroy, G. L. *Organometallics* **1983**, *2*, 846.
(37) Smith, W. F.; Yule, J.; Taylor, N. J.; Paik, H. N.; Carty, A. J. *Inorg. Chem.* **1977**, *16*, 1593.
(38) Yu, Y.-F.; Gallucci, J.; Wojcicki, A. *J. Am. Chem. Soc.* **1983**, *105*, 4826.

Table VI. ^{31}P NMR Spectroscopic Data[a]

complex	no.	chemical shift, ppm: μ-PPh_2	L	$^2J_{PP}$, Hz
$[Fe_2(CO)_5(PMe_3)_3(PPh_2)]^+[Fe_2(CO)_8(PPh_2)]^-$[b]	**5a**	160.1, dd 58.0, s	18.5, 11.0, d, 16.2, s	31, 21
$\{Fe_2(CO)_5[P(OMe)_3]_3(PPh_2)\}^+\{Fe_2(CO)_6[P(OMe)_3]_2(PPh_2)\}^-$[c]	**5b**	164.5, ddd 71.8, t	165.3, 160.3, 159.8, d 202.1, d	26, 81, 9 55
$Et_4N[Fe_2(CO)_6(PPh_3)(PPh_2)]$	**6a**	139.0, d	78.2, d	32
$Et_4N[Fe_2(CO)_6(PMe_3)(PPh_2)]$	**6b**	134.2, d	33.6, d	29
$Et_4N\{Fe_2(CO)_6[P(OMe)_3](PPh_2)\}$	**6c**	129.4, d	192.9, d	70
$Et_4N[Fe_2(CO)_5(PMe_3)_2(PPh_2)]$	**6d**	120.1, t	26.8, d	14
$Et_4N\{Fe_2(CO)_5[P(OMe)_3]_2(PPh_2)\}$	**6e**	117.1, t	194.4, d	34
$Et_4N[Fe_2(CO)_6(PPh_3)_2(PPh_2)]$	**7a**	83.4, t	86.7, d	23
$Et_4N[Fe_2(CO)_6(PMe_3)_2(PPh_2)]$	**7b**	75.4, t	42.4, d	18
$Et_4N\{Fe_2(CO)_6[P(OMe)_3]_2(PPh_2)\}$	**7c**	70.6, t	199.1, d	54
$Et_4N[Fe_2(CO)_7(PPh_3)(PPh_2)]$	**7d**	88.8, d	72.9, d	26
$Et_4N[Fe_2(CO)_7(PMe_3)(PPh_2)]$	**7e**	68.3, d	44.7, d	21
$Et_4N\{Fe_2(CO)_7[P(OMe)_3](PPh_2)\}$	**7f**	63.6, d	197.0, d	57
$FeCo(CO)_7(PPh_2)$	**8**	193.0, s		
$FeCo(CO)_6(PPh_3)(PPh_2)$	**8a**	195.1, d	64.0, d	23
$FeCo(CO)_6(PPh_3)(PPh_2)$	**8a′**	164.9, d	57.7*, d	87
$FeCo(CO)_6[P(OMe)_3](PPh_2)$[d]	**8b**	191.9, d	173.2, d	56
$FeCo(CO)_6[P(OMe)_3](PPh_2)$[d]	**8b′**	168.6, d	172.1*, d	168
$FeCo(CO)_6(PMe_3)(PPh_2)$	**8c**	195.9, d	17.6, d	25
$FeCo(CO)_6(PMe_3)(PPh_2)$	**8c′**	146.6, d	17.1*, d	85
$FeCo(CO)_5[P(OMe)_3]_2(PPh_2)$	**9a**	168.2, d	180.4*, br, 178.8, dd	48, 3.5
$FeCo(CO)_5(PMe_3)_2(PPh_2)$	**9b**	172.2, dd	17.3*, 34.6, d	80, 16
$FeCo(CO)_6[P(OMe)_3]_2(PPh_2)$	**10a**	78.7, dd	156.8*, 193.7, d	99, 69
$FeCo(CO)_6(PMe_3)_2(PPh_2)$	**10b**	80.5, dd	23.7*, 45.7, d	53, 26
$FeCo(CO)_7(PMe_3)(PPh_2)$	**11**	63.8, d	27.5*, d	59
$[Na(THF)_n]_2[FeCo(CO)_6(PPh_2)]$	**13**	185.7, s		

[a] Recorded at 25 °C in THF-d_8. Complexes **6** and **7** were run in CD_3CN, and **8** and **9** were run at −60 °C to reduce ^{59}Co quadrupolar line broadening. Asterisk denotes L on Co center. [b] Recorded at −40 °C. [c] Recorded at 50 °C in $(CD_3)_2CO$. [d] Recorded in toluene-d_8.

Table VII. Summary of X-ray Diffraction Data

complex	$Fe_2(CO)_6[P(OMe)_3]$-(μ-PPh_2) (**2d**)	$[Fe_2(CO)_5(PMe_3)_3(\mu\text{-}PPh_2)]^+$-$[Fe_2(CO)_8(\mu\text{-}PPh_2)]^-$ (**5a**)	$Et_4N[Fe_2(CO)_6(PPh_3)_2$-($\mu$-$PPh_2$)] (**7a**)	$FeCo(CO)_5[P(OMe)_3]_2$-(μ-PPh_2) (**9a**)
formula	$C_{21}H_{19}Fe_2O_9P_2$	$C_{46}H_{47}Fe_4O_{13}P_5$	$C_{62}H_{60}Fe_2NO_6P_3$	$C_{23}H_{28}CoFeO_{11}P_3$
fw	589.02	1186.14	1119.79	688.17
a, Å	14.629 (4)	10.097 (2)	11.606 (2)	10.446 (2)
b, Å	11.218 (4)	17.077 (6)	21.647 (5)	11.496 (2)
c, Å	15.004 (3)	15.418 (7)	21.999 (8)	12.366 (3)
α, deg				95.59 (2)
β, deg	92.60 (2)	93.60 (3)	96.53 (2)	90.66 (2)
γ, deg				98.69 (2)
V, Å^3	2460 (2)	2653.2	5491.1	1460.4
Z	4	2	4	2
ρ_{calcd}, g cm^{-3}	1.59	1.485	1.354	1.565
space gp	Cc (No. 9)	$P2_1$ (No. 4)	$P2_1/c$ (No. 14)	$P\bar{1}$ (No. 2)
cryst dimens, mm	0.40 × 0.35 × 0.35	0.43 × 0.35 × 0.48	0.25 × 0.41 × 0.48	0.32 × 0.32 × 0.50
temp, °C	−94	−70	−70	−70
radiatn	Mo Kα	Mo Kα	Mo Kα	Mo Kα
μ, cm^{-1}	13.89	12.77	6.64	12.77
data collcn method	ω–2θ	ω–2θ	ω–2θ	ω–2θ
max 2θ, deg	54.0	55.0	48.0	55.0
scan speed, deg/min	5.0	1.80–5.00	1.50–5.00	1.7–5.0
scan width, deg	0.8 + 0.35 tan θ	1.20 − 1.80ω	1.20 − 1.50ω	1.20 − 1.90ω
total no. of observns	2835	6553	9146	7028
no. of unique data, $I > 3\sigma(I)$	2478	4256	3110	4590
final no. of variables	357	612	667	352
final max shift/error	0.13	0.15	0.05	0.05
max residual density, e$^-$/Å^3	0.34	0.47	0.41	0.81
R^a	0.024	0.042	0.053	0.043
R_w^b	0.034	0.043	0.046	0.048

[a] $\sum||F_o| - |F_c||/\sum|F_o|$. [b] $[\sum w(|F_o| - |F_c|)^2/\sum wF_o^2]^{1/2}$.

$RuCo(PPh_3)_2(CO)_5(\mu\text{-}PPh_2)$ although it has been noted[24] that this isomer is not formed by direct substitution of $RuCo(CO)_7(\mu\text{-}PPh_2)$. The Co–P bond distances are ca. 0.08 Å shorter than the Fe–P distances, and the M–P bond distances to the phosphite ligands are ca. 0.06 Å shorter than those to the PPh_2 bridge. While the Fe–Co and Co–$P(PPh_2)$ bond distances increase in **9a** relative to the unsubstituted **8**, the major structural difference induced by substitution involves the rotation of the CoL_3 fragment with respect to the Fe–P vector. The PPh_2 bridge converts from an axial ligand on Co in **8** to an equatorial ligand on Co in **9a**.

Spectroscopic Characterization of $FeCo(CO)_{7-n}L_n(\mu\text{-}PPh_2)$ (8–9) and of the CO Ligand Adducts 10–11. The ^{31}P NMR spectra of the initial substitution products **8a′–c′** consisted of two

(39) Foley, H. C.; Finch, W. C.; Pierpont, C. G.; Geoffroy, G. L. *Organometallics* **1982**, *1*, 1379.

Table VIII. Atomic Coordinates and Temperature Factors for $Fe_2(CO)_6[P(OMe)_3](\mu\text{-}PPh_2)$ (**2d**)

atom	*x*	*y*	*z*	*B*(eq)
Fe1	0	0.28713 (4)	0	1.63 (2)
Fe2	−0.16657 (4)	0.20691 (4)	−0.02920 (4)	1.83 (2)
P1	0.06268 (7)	0.21085 (8)	0.12121 (6)	1.99 (3)
P2	−0.09200 (7)	0.32492 (8)	−0.11829 (6)	1.67 (3)
O1	0.1482 (3)	0.4478 (4)	−0.0412 (3)	6.1 (2)
O2	−0.1125 (2)	0.4332 (3)	0.1143 (2)	4.1 (1)
O3	0.0383 (3)	0.0547 (3)	−0.0790 (2)	4.5 (2)
O4	−0.3518 (3)	0.2995 (4)	−0.0629 (3)	5.4 (2)
O5	−0.1888 (3)	−0.0042 (3)	−0.1444 (3)	5.1 (2)
O6	−0.2112 (2)	0.0903 (3)	0.1395 (2)	4.1 (1)
O7	−0.0107 (2)	0.1564 (4)	0.1822 (2)	2.6 (1)
O8	0.1310 (2)	0.2880 (3)	0.1826 (2)	2.6 (1)
O9	0.1291 (2)	0.0970 (3)	0.1108 (2)	2.7 (1)
O7B	0.009 (1)	0.108 (1)	0.158 (1)	2.3 (3)
O8B	0.053 (1)	0.302 (1)	0.214 (1)	2.9 (3)
O9B	0.163 (1)	0.192 (1)	0.132 (1)	2.5 (2)
C1	0.0910 (3)	0.3845 (4)	−0.0251 (3)	3.2 (2)
C2	−0.0718 (3)	0.3748 (4)	0.0685 (2)	2.5 (1)
C3	0.0210 (3)	0.1457 (4)	−0.0494 (3)	2.8 (2)
C4	−0.2791 (3)	0.2661 (4)	−0.0487 (3)	2.9 (2)
C5	−0.1779 (3)	0.0773 (4)	−0.0997 (3)	3.1 (2)
C6	−0.1902 (3)	0.1352 (4)	0.0760 (3)	2.7 (2)
C7	0.0140 (3)	0.0830 (5)	0.2600 (3)	4.0 (2)
C8	0.1020 (4)	0.4042 (5)	0.2156 (4)	4.2 (2)
C9	0.2098 (3)	0.1059 (5)	0.0620 (3)	4.0 (2)
C10	−0.1371 (2)	0.4742 (3)	−0.1394 (2)	2.0 (1)
C11	−0.2153 (3)	0.4873 (4)	−0.1961 (3)	2.9 (2)
C12	−0.2514 (3)	0.5986 (4)	−0.2139 (3)	3.5 (2)
C13	−0.2112 (4)	0.6978 (4)	−0.1762 (3)	3.6 (2)
C14	−0.1352 (4)	0.6872 (4)	−0.1186 (4)	3.8 (2)
C15	−0.0976 (3)	0.5749 (4)	−0.1002 (3)	2.8 (2)
C16	−0.0593 (3)	0.2750 (3)	−0.2282 (2)	2.0 (1)
C17	−0.1221 (3)	0.2184 (4)	−0.2866 (3)	2.7 (2)
C18	−0.0964 (4)	0.1832 (4)	−0.3705 (3)	3.6 (2)
C19	−0.0088 (4)	0.2030 (4)	−0.3966 (3)	3.5 (2)
C20	0.0538 (3)	0.2578 (5)	−0.3405 (3)	3.4 (2)
C21	0.0294 (3)	0.2953 (4)	−0.2565 (3)	2.8 (2)

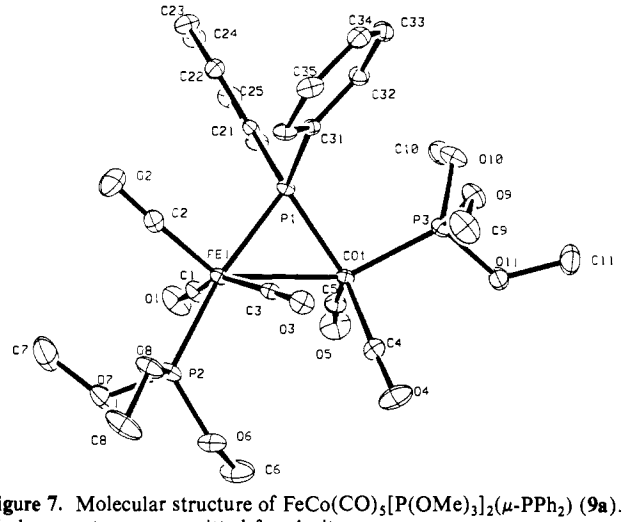

Figure 7. Molecular structure of $FeCo(CO)_5[P(OMe)_3]_2(\mu\text{-}PPh_2)$ (**9a**). Hydrogen atoms are omitted for clarity.

broad doublet resonances, which narrowed on cooling to −60 °C, suggesting that both phosphorus atoms are bound to Co. The large values of $^2J_{PP}$ further suggest that L is trans to the PPh_2 bridge as found previously[22] for the μ-$AsMe_2$ analogues. The spectra of the thermodynamic 34e products, **8a–c**, contain both broad and sharp doublets at 25 °C, with the former narrowing on cooling to −60 °C, indicating that L is now on the Fe center. Although we cannot rule out the cis structure, as observed previously[24] for $RuCo(CO)_6(PPh_3)(\mu\text{-}PPh_2)$, the value of $^2J_{PP}$ for **8a** resembles that observed previously[36] for $FeIr(CO)_5(PPh_3)_2(\mu\text{-}PPh_2)$, which has PPh_3 trans to the PPh_2 bridge. The ^{31}P NMR spectrum of the $[P(OMe)_3]_2$-substituted 34e complex **9a** is consistent with the solid-state structure. The Fe–phosphite ligand has $^2J_{PP}$ = 48 Hz

Table IX. Selected Bond Distances (Å) and Angles (deg) for $Fe_2(CO)_6[P(OMe)_3](\mu\text{-}PPh_2)$ (**2d**)

	Distances		
Fe1–C1	1.776 (4)	P1–O8B	1.74 (2)
Fe1–C3	1.784 (4)	P2–C10	1.822 (4)
Fe1–C2	1.797 (4)	P2–C16	1.825 (4)
Fe1–P1	2.175 (1)	O1–C1	1.131 (5)
Fe1–P2	2.219 (1)	O2–C2	1.137 (5)
Fe1–Fe2	2.6159 (9)	O3–C3	1.146 (5)
Fe2–C4	1.787 (4)	O4–C4	1.137 (6)
Fe2–C5	1.804 (4)	O5–C5	1.137 (5)
Fe2–C6	1.819 (4)	O6–C6	1.133 (5)
Fe2–P2	2.205 (1)	O7–C7	1.460 (5)
P1–O9B	1.49 (1)	O8–C8	1.464 (6)
P1–O7B	1.51 (1)	O9–C9	1.420 (6)
P1–O7	1.566 (3)	O7B–C7	1.56 (2)
P1–O8	1.585 (4)	O8B–C8	1.35 (2)
P1–O9	1.617 (3)	O9B–C9	1.60 (1)
	Angles		
C1–Fe1–C3	108.3 (2)	O6–C6–Fe2	175.3 (4)
C1–Fe1–C2	104.4 (2)	O9B–P1–O8B	96.2 (7)
C1–Fe1–P1	97.3 (1)	O9B–P1–Fe1	121.7 (6)
C1–Fe1–P2	98.4 (1)	O7B–P1–O8B	95.1 (8)
C1–Fe1–Fe2	151.4 (1)	O7B–P1–Fe1	113.3 (6)
C3–Fe1–C2	147.3 (2)	O7–P1–O8	107.7 (2)
C3–Fe1–P1	85.6 (1)	O7–P1–O9	100.4 (2)
C3–Fe1–P2	87.0 (1)	O7–P1–Fe1	111.6 (1)
C3–Fe1–Fe2	78.5 (1)	O8–P1–O9	97.0 (2)
C2–Fe1–P1	88.4 (1)	O8–P1–Fe1	120.1 (1)
C2–Fe1–P2	90.2 (1)	O9–P1–Fe1	117.5 (1)
C2–Fe1–Fe2	73.7 (1)	O8B–P1–Fe1	113.3 (5)
P1–Fe1–P2	164.04 (4)	C10–P2–C16	103.5 (2)
P1–Fe1–Fe2	111.03 (3)	C10–P2–Fe2	118.1 (1)
P2–Fe1–Fe2	53.50 (3)	C10–P2–Fe1	121.1 (1)
C4–Fe2–C5	97.4 (2)	C16–P2–Fe2	121.3 (1)
C4–Fe2–C6	95.5 (2)	C16–P2–Fe1	119.3 (1)
C4–Fe2–P2	98.9 (1)	Fe2–P2–Fe1	72.50 (3)
C4–Fe2–Fe1	138.1 (2)	C7–O7–P1	122.4 (3)
C5–Fe2–C6	97.6 (2)	C8–O8–P1	119.9 (3)
C5–Fe2–P2	99.9 (1)	C9–O9–P1	120.8 (3)
C5–Fe2–Fe1	116.8 (1)	P1–O7B–C7	120 (1)
C6–Fe2–P2	155.6 (1)	C8–O8B–P1	117 (1)
C6–Fe2–Fe1	102.7 (1)	P1–O9B–C9	117.3 (9)
P2–Fe2–Fe1	54.00 (3)	O1–C1–Fe1	179.1 (5)
O9B–P1–O7B	112.5 (8)	O2–C2–Fe1	175.8 (4)
O4–C4–Fe2	177.2 (5)	O3–C3–Fe1	176.8 (3)
O5–C5–Fe2	179.5 (5)		

to the trans PPh_2 bridge, and a small three-bond coupling to the Co–phosphite ligand (3.5 Hz) is also observed. While the ^{31}P NMR spectrum of the PMe_3 analogue **9b** also consists of one sharp and two broad resonances, the two-bond P–P coupling constants are quite different from those of **9a**. The $^2J_{PP}$ values for **9b** are very similar, however, to those reported previously[40] for $FeCo(CO)_5(PMe_3)_2[\mu\text{-}P(t\text{-}Bu)_2]$, which was shown by X-ray diffraction to have one L on each metal, both trans to the PPh_2 bridge. For the 36e complexes, the ^{31}P NMR spectra are little affected by the quadrupolar ^{59}Co nucleus, and all resonances are fairly sharp at 25 °C. Nevertheless, the magnitude of $^2J_{PP}$ and the photolysis results discussed above lead us to propose a structure for **11** which has the PMe_3 ligand on Co trans to the PPh_2 bridge. The disubstituted analogues **10a,b** have one L on each metal and probably both trans to PPh_2, as observed for the isoelectronic diiron anion $[Fe_2(CO)_6(PPh_3)_2(\mu\text{-}PPh_2)]^-$ (**7a**).

Electrochemical Studies of 33e and 34e Dinuclear Iron Complexes. Initial electrochemical measurements focused on the 33e dinuclear radical $Fe_2(CO)_7(\mu\text{-}PPh_2)$ (**1**) and its 34e counterpart $[Fe_2(CO)_6(\mu\text{-}CO)(\mu\text{-}PPh_2)]^-$ (**6**). Electrochemical data for complexes **1** and **6**, obtained by cyclic voltammetry, are presented in Table XVI. Both **1** and **6** undergo chemically reversible 1e reductions and oxidations, respectively (i_{pa}/i_{pc} = 1) with identical half-wave potentials ($E_{1/2}$ at room temperature in CH_2Cl_2 at scan

(40) Chandler, D. J.; Jones, R. A.; Stuart, A. L.; Wright, T. C. *Organometallics* **1984**, *3*, 1830.

Table X. Atomic Coordinates (×10000) and Temperature Factors for $[Fe_2(CO)_5(PMe_3)_3(\mu\text{-}PPh_2)][Fe_2(CO)_8(\mu\text{-}PPh_2)]$ (**5a**)

atom	x	y	z	B(iso)[a]	atom	x	y	z	B(iso)[a]
Fe1	1657.9 (10)	5000.0	2092.7 (7)	1.6 (1)	C13	6508 (9)	3681 (6)	6617 (6)	3.0 (2)
Fe2	−325.9 (10)	5795.5 (9)	2901.6 (7)	1.7 (1)	C21	4302 (9)	3719 (6)	1982 (7)	4.0 (3)
Fe3	6833 (1)	5691 (1)	9051 (1)	1.8 (1)	C22	1817 (10)	3003 (5)	1821 (6)	3.4 (3)
Fe4	7769 (1)	4176 (1)	7208 (1)	2.0 (1)	C23	2683 (12)	3838 (7)	436 (6)	5.2 (3)
P1	441 (2)	4586 (1)	3149 (1)	1.8 (1)	C24	2942 (9)	6868 (5)	1927 (7)	3.5 (3)
P2	2611 (2)	3923 (2)	1610 (1)	2.6 (1)	C25	4199 (9)	5786 (7)	956 (7)	4.6 (3)
P3	2573 (2)	5978 (1)	1338 (1)	2.6 (1)	C26	1701 (10)	6334 (6)	366 (6)	4.4 (3)
P4	−1784 (2)	6118 (1)	3869 (1)	2.5 (1)	C27	−3115 (10)	6724 (6)	3419 (6)	4.2 (3)
P5	6238 (2)	5029 (1)	7774 (1)	1.6 (1)	C28	−1184 (9)	6703 (5)	4793 (6)	3.1 (2)
O1	3957 (6)	5279 (4)	3302 (4)	3.4 (2)	C29	−2649 (9)	5299 (5)	4339 (6)	3.4 (3)
O2	−283 (6)	4852 (4)	619 (4)	3.9 (2)	C31	1306 (7)	4378 (4)	4200 (4)	1.6 (2)
O3	−2669 (6)	5165 (4)	1928 (4)	3.6 (2)	C32	993 (8)	4748 (5)	4961 (5)	2.3 (2)
O4	1834 (6)	6459 (4)	4034 (4)	3.1 (2)	C33	1595 (8)	4547 (5)	5752 (5)	2.6 (2)
O5	−382 (7)	7213 (4)	1829 (4)	3.8 (2)	C34	2547 (8)	3970 (5)	5804 (5)	2.3 (2)
O6	6362 (7)	4267 (4)	10057 (4)	3.8 (2)	C35	2899 (9)	3603 (5)	5055 (5)	2.9 (2)
O7	4580 (6)	6759 (4)	8764 (4)	4.0 (2)	C36	2281 (8)	3805 (5)	4267 (5)	2.5 (2)
O8	9533 (6)	5957 (5)	8509 (4)	4.6 (2)	C41	−699 (8)	3756 (5)	3060 (5)	2.2 (2)
O9	7504 (7)	6588 (4)	10616 (4)	4.9 (2)	C42	−984 (10)	3315 (6)	3780 (6)	3.5 (3)
O10	9034 (7)	5566 (4)	6490 (4)	3.9 (2)	C43	−1846 (11)	2688 (6)	3725 (7)	4.5 (3)
O11	9616 (7)	3121 (4)	6436 (5)	4.4 (2)	C44	−2456 (10)	2485 (6)	2918 (7)	4.3 (3)
O12	8697 (7)	3648 (4)	8948 (4)	4.3 (2)	C45	−2193 (10)	2918 (6)	2195 (7)	3.8 (3)
O13	5707 (7)	3324 (5)	6196 (5)	5.2 (2)	C46	−1328 (8)	3536 (5)	2263 (6)	2.8 (2)
C1	3021 (8)	5167 (5)	2843 (5)	2.3 (2)	C51	4652 (7)	4548 (4)	7951 (5)	1.8 (2)
C2	441 (8)	4902 (5)	1227 (5)	2.3 (2)	C52	4584 (8)	3750 (5)	8149 (5)	2.3 (2)
C3	−1707 (8)	5403 (5)	2287 (5)	2.2 (2)	C53	3381 (10)	3399 (5)	8305 (6)	3.1 (2)
C4	1007 (8)	6183 (5)	3588 (5)	2.0 (2)	C54	2242 (9)	3827 (6)	8280 (6)	3.5 (3)
C5	−361 (8)	6660 (5)	2244 (5)	2.1 (2)	C55	2286 (8)	4610 (6)	8093 (6)	3.2 (2)
C6	6549 (8)	4810 (5)	9637 (5)	2.1 (2)	C56	3473 (7)	4973 (5)	7935 (5)	2.3 (2)
C7	5473 (8)	6325 (5)	8846 (5)	2.4 (2)	C61	5691 (7)	5702 (5)	6888 (4)	1.7 (2)
C8	8454 (8)	5833 (5)	8694 (5)	2.7 (2)	C62	4871 (8)	5437 (5)	6193 (5)	2.4 (2)
C9	7251 (9)	6225 (5)	9985 (5)	2.8 (2)	C63	4430 (8)	5937 (5)	5541 (5)	2.7 (2)
C10	8534 (8)	5020 (5)	6786 (5)	2.6 (2)	C64	4821 (9)	6714 (5)	5540 (5)	2.8 (2)
C11	8893 (8)	3550 (5)	6744 (6)	2.4 (2)	C65	5668 (10)	6968 (5)	6199 (6)	3.2 (3)
C12	8310 (9)	3882 (5)	8279 (6)	2.6 (2)	C66	6092 (8)	6477 (5)	6867 (5)	2.2 (2)

[a] Anisotropically refined atoms are given in the form of the isotropic equivalent thermal parameter defined as $^4/_3[a^2B_{11} + b^2B_{22} + c^2B_{33} + ab(\cos\gamma)B_{12} + ac(\cos\beta)B_{13} + bc(\cos\alpha)B_{23}]$.

rates between 50 and 5000 mV/s). Mixed solutions of **1** and **6** show superimposed cyclic voltammograms for the two species. The cyclic voltammograms of **1** and **6** remain indistinguishable when the temperature is decreased to −40 °C. Both decreasing the temperature at a constant scan rate and increasing the scan rate at a constant temperature result in an increase in ΔE_p (separation of anodic and cathodic peaks) consistent with a slow heterogeneous electron transfer. Since the species $\mathbf{1}^-$ and $\mathbf{6}^+$ are not observed directly, no kinetic or thermodynamic information could be obtained about this structural isomerization.[41] A quasi-reversible scheme involving just **1** and **6** adequately models the observed electrochemistry (eq 9). Isomerization between $\mathbf{1}^-$ and **6** and

$$\underset{\mathbf{1}}{Fe_2(CO)_7(\mu\text{-}PPh_2)} + e^- \underset{E_R}{\rightleftharpoons} \underset{\mathbf{6}}{[Fe_2(CO)_6(\mu\text{-}CO)(\mu\text{-}PPh_2)]^-} \quad (9)$$

between $\mathbf{6}^+$ and **1**, which requires exchange of a bridging for a terminal carbonyl group, occurs faster than the limiting rate of heterogeneous electron transfer. This implies both a small reorganization energy and a low activation barrier to rearrangement in this system.

Both 17e mononuclear[5-16] and odd-electron multinuclear metal carbonyl radicals[17-19] readily substitute CO for Lewis bases. Transient electrochemical measurements have been used successfully to obtain thermodynamic and kinetic information for some of these systems.[7,8,11,16,17c] The fast isomerization of the bridging CO ligand in **6** to a terminal position in **1** on oxidation of **6** provides a convenient route for generating the 33e radical **1** for mechanistic studies.

Qualitative electrochemical studies of CO substitution in complex **1** were performed by adding known concentrations of a PR_3 nucleophile to dry, degassed solutions of **6** in CH_2Cl_2. Figure 8A shows the cyclic voltammogram obtained from addition of 30 mM PPh_3 to a 1 mM solution of **6** at 20 °C. Peaks A and

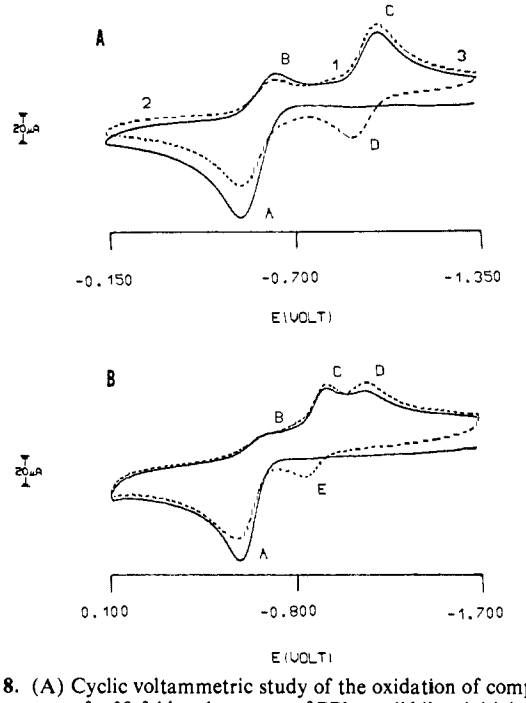

Figure 8. (A) Cyclic voltammetric study of the oxidation of complex **6** in the presence of a 30-fold molar excess of PPh_3: solid line, initial anodic scan cyclic voltammogram; dashed line, steady-state cyclic voltammogram attained at repetitive scans. Experimental conditions: $[Et_4N][Fe_2(CO)_6(\mu\text{-}CO)(\mu\text{-}PPh_2)]] = 1 \times 10^{-3}$ M; [TBAHFP] = 0.15 M; temperature 20 °C; scan rate 400 mV/s; solvent, CH_2Cl_2; IR compensated. (B) Cyclic voltammetric study of the oxidation of complex **6** in the presence of a 25-fold molar excess of $P(OMe)_3$: solid line, initial anodic scan cyclic voltammogram; dashed line, steady-state cyclic voltammogram attained at repetitive scans. Experimental conditions: same as Figure 8A, except the temperature is 10 °C.

(41) For a comprehensive review on this subject, see: Geiger, W. E. *Prog. Inorg. Chem.* **1985**, *33*, 275.

Table XI. Selected Bond Distances (Å) and Angles (deg) for $[Fe_2(CO)_5(PMe_3)_3(\mu\text{-}PPh_2)][Fe_2(CO)_8(\mu\text{-}PPh_2)]$ (**5a**)

	Distances		
Fe1–Fe2	2.780 (2)	P2–C22	1.803 (10)
Fe1–P1	2.217 (2)	P2–C23	1.821 (9)
Fe1–P2	2.226 (3)	P3–C24	1.797 (10)
Fe1–P3	2.265 (2)	P3–C25	1.808 (9)
Fe2–P1	2.230 (2)	P3–C26	1.796 (10)
Fe2–P4	2.230 (2)	P4–C27	1.801 (10)
Fe3–P5	2.317 (2)	P4–C28	1.813 (9)
Fe4–P5	2.332 (2)	P4–C29	1.822 (9)
Fe1–C1	1.764 (8)	P5–C51	1.835 (7)
Fe1–C2	1.764 (8)	P5–C61	1.844 (7)
Fe2–C3	1.768 (8)	O1–C1	1.160 (9)
Fe2–C4	1.785 (8)	O2–C2	1.155 (9)
Fe2–C5	1.789 (8)	O3–C3	1.161 (9)
Fe3–C6	1.787 (8)	O4–C4	1.150 (9)
Fe3–C7	1.762 (8)	O5–C5	1.141 (9)
Fe3–C8	1.776 (8)	O6–C6	1.153 (9)
Fe3C9	1.734 (8)	O7–C7	1.167 (9)
Fe4–C10	1.777 (9)	O8–C8	1.163 (9)
Fe4–C11	1.745 (8)	O9–C9	1.168 (9)
Fe4–C12	1.779 (9)	O10–C10	1.167 (10)
Fe4–C13	1.738 (9)	O11–C11	1.157 (9)
P1–C31	1.827 (7)	O12–C12	1.152 (10)
P1–C41	1.826 (8)	O13–C13	1.176 (10)
P2–C21	1.801 (10)		
	Angles		
Fe2–Fe1–P1	51.53 (6)	P5–Fe4–C10	86.8 (3)
Fe2–Fe1–P2	153.24 (8)	P5–Fe4–C11	177.8 (3)
Fe2–Fe1–P3	101.47 (8)	P5–Fe4–C12	90.1 (3)
Fe1–Fe2–P1	51.10 (6)	P5–Fe4–C13	91.1 (3)
Fe1–Fe2–P4	160.99 (8)	C1–Fe1–C2	171.4 (4)
Fe2–Fe1–C1	100.4 (3)	C3–Fe2–C4	176.1 (4)
Fe2–Fe1–C2	84.2 (3)	C3–Fe2–C5	91.3 (4)
Fe1–Fe2–C3	98.1 (3)	C4–Fe2–C5	91.0 (4)
Fe1–Fe2–C4	84.8 (2)	C6–Fe3–C7	117.4 (4)
Fe1–Fe2–C5	97.9 (3)	C6–Fe3–C8	116.8 (4)
P1–Fe1–P2	104.7 (1)	C6–Fe3–C9	93.5 (4)
P1–Fe1–P3	151.1 (1)	C7–Fe3–C8	125.7 (4)
P2–Fe1–P3	103.8 (1)	C7–Fe3–C9	88.4 (4)
P1–Fe2–P4	110.5 (1)	C8–Fe3–C9	90.3 (4)
P1–Fe1–C1	90.9 (3)	C10–Fe4–C11	92.2 (4)
P1–Fe1–C2	97.7 (3)	C10–Fe4–C12	117.0 (4)
P2–Fe1–C1	91.0 (3)	C10–Fe4–C13	121.6 (4)
P2–Fe1–C2	87.9 (3)	C11–Fe4–C12	92.2 (4)
P3–Fe1–C1	83.8 (3)	C11–Fe4–C13	87.8 (4)
P3–Fe1–C2	88.2 (3)	C12–Fe4–C13	121.4 (4)
P1–Fe2–C3	89.7 (3)	Fe1–P1–Fe2	77.37 (8)
P1–Fe2–C4	90.0 (3)	Fe3–P5–Fe4	118.7 (1)
P1–Fe2–C5	148.8 (3)	Fe1–P1–C31	117.2 (2)
P4–Fe2–C3	85.5 (3)	Fe1–P1–C41	124.6 (3)
P4–Fe2–C4	91.0 (2)	Fe2–P1–C31	118.3 (3)
P4–Fe2–C5	100.7 (3)	Fe2–P1–C41	119.7 (3)
P5–Fe3–C6	88.7 (3)	Fe3–P5–C51	105.9 (2)
P5–Fe3–C7	89.4 (3)	Fe3–P5–C61	112.0 (3)
P5–Fe3–C8	89.9 (3)	Fe4–P5–C51	112.4 (3)
P5–Fe3–C9	177.4 (3)	Fe4–P5–C61	106.7 (2)

B correspond to the redox couple for oxidation of **6** and reduction of **1**, respectively. The decrease in intensity of wave B implies that PR_3 reacts with some of the 33e radical **1** produced on electrochemical oxidation of **6**. Scanning to more negative potential shows a new cathodic wave labeled C in the presence of PPh_3. Repeating the voltammetric scan shows that C is coupled to the anodic wave D. This chemically reversible redox couple corresponds to reduction of the monosubstituted 33e complex $Fe_2(CO)_6(PPh_3)(\mu\text{-}PPh_2)$ (**2a**) followed by oxidation of the 34e carbonyl-bridged species $[Fe_2(CO)_5(PPh_3)(\mu\text{-}CO)(\mu\text{-}PPh_2)]^-$ (**6a**), which forms on reduction, as confirmed by electrochemical examination of an authentic sample of **2a** (Table XVI).

For all phosphorus ligands (Table XVI) only monosubstituted products form in the reaction with **1** on the time scale of the cyclic voltammetric experiments, except when the Lewis base is $P(OMe)_3$. The sterically unhindered $P(OMe)_3$ nucleophile yields mono- and disubstituted products in the cyclic voltammetric experiments (50–5000 mV/s). Disproportionation products are not

Scheme V

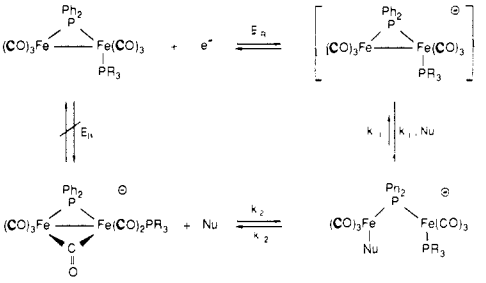

observed on the time scale of the electrochemical experiments. A cyclic voltammogram obtained on addition of 25 mM $P(OMe)_3$ to a 1 mM solution of **6** again shows A and B for the redox couple from **6** and **1** (Figure 8B). Assignment of the cathodic wave C to reduction of 33e $Fe_2(CO)_6[P(OMe)_3](\mu\text{-}PPh_2)$ (**2d**) and the cathodic wave D to the reduction of the 33e bis(phosphite)-substituted complex is verified by electrochemical examination of authentic samples of each complex. The experiments with authentic samples show that anodic wave E arises from oxidation of the 34e $P(OMe)_3$-monosubstituted anion, **6c**. The reduced disubstituted complex, **6e**, formed at cathodic wave D, has no observable anodic wave. It is important to note that authentic 33e $Fe_2(CO)_5[P(OMe)_3]_2(\mu\text{-}PPh_2)$ (**4c**) was generated by oxidation of 36e $Et_4N\{Fe_2(CO)_6[P(OMe)_3]_2(\mu\text{-}PPh_2)\}$ (**7c**) (a species possessing no metal–metal bond) according to reaction 10. The

$$\underset{\mathbf{4c}}{\{Fe_2(CO)_6[P(OMe)_3]_2(\mu\text{-}PPh_2)\}^-} \underset{+e^-}{\overset{-e^-}{\rightleftharpoons}} \underset{\mathbf{7c}}{Fe_2(CO)_5[P(OMe)_3]_2(\mu\text{-}PPh_2)} + CO \quad (10)$$

large ΔE_p for this reaction (605 mV, Table XVI), in comparison to those of other entries in Table XVI, probably results from the intervening chemical processes of CO loss and metal–metal bond formation that occur on oxidation of the anion. If the reverse pathway were to occur for the reduction of $Fe_2(CO)_5[P(OMe)_3]_2(\mu\text{-}PPh_2)$, produced via oxidation of **6** in the presence of $P(OMe)_3$, the resulting anodic wave would lie under the anodic wave for **6**, the dominant species in the bulk phase of the solution. Such a pathway is plausible because there will be CO in the diffusion layer near the electrode.

Data presented in Table XVI also show that complexes **1** and **6**, and their PR_3-substituted derivatives, exhibit irreversible to quasi-reversible behavior with formal potentials that span a wide range (−0.624 to −1.072 V). Reduction potentials for the monosubstituted 33e complexes vary little with the phosphine. This agrees with ESR spectral evidence presented earlier that shows L trans to the phosphido bridge on the six-coordinate iron atom, while the unpaired electron resides primarily on the pseudotrigonal-bipyramidal iron atom. The negligible phosphorus character in the HOMO of the complex results in the relative insensitivity of reduction potentials of the 33e phosphine-substituted complexes to the electronic features of the phosphine. This behavior contrasts markedly with electrochemical data obtained for PR_3-substituted mononuclear 17e iron carbonyl radicals.[16]

The magnitude of ΔE_p and the measure of chemical reversibility, i_{pa}/i_{pc}, depend on both steric and electronic features of PR_3. Note that no complex in Table XVI having a substituent with a $pK_a > 5$ (see Table XVII) exhibits chemical reversibility. The reasons for chemical irreversibility and for the large values of ΔE_p observed with some complexes are unknown. Possibly, the steric and electronic features of the phosphorus Lewis base affect the ease with which a terminal carbonyl returns to the bridging position on reduction of the 33e $Fe_2(CO)_6(PR_3)(\mu\text{-}PPh_2)$ complex. Alternatively, a different redox pathway may become operative that involves uptake of an additional 2e donor, and cleavage of the metal–metal bond on reduction, similar to that discussed above for $Fe_2(CO)_5[P(OMe)_3]_2(\mu\text{-}PPh_2)$. Such a pathway is outlined in Scheme V. A reductive pathway such as this may become important when electron-rich nucleophiles, such as PMe_3, are in excess in the bulk phase of the solution in the electrochemical cell.

Table XII. Atomic Coordinates (×10000) and Temperature Factors for $Et_4N[Fe_2(CO)_6(PPh_3)_2(\mu\text{-}PPh_2)]$ (7a)

atom	x	y	z	B(iso)[a]	atom	x	y	z	B(iso)[a]
Fe1	1951 (1)	7120 (1)	1087 (1)	1.7 (1)	C42	−1036 (9)	7523 (5)	1241 (5)	2.9 (4)
Fe2	3980 (1)	5968 (1)	2116 (1)	1.7 (1)	C43	−2239 (9)	7488 (5)	1220 (5)	3.2 (4)
P1	2888 (2)	6177 (1)	1205 (1)	1.5 (1)	C44	−2921 (8)	7928 (6)	913 (6)	3.6 (4)
P2	1091 (2)	8026 (1)	1044 (1)	1.7 (1)	C45	−2395 (10)	8397 (6)	618 (5)	3.6 (4)
P3	5041 (2)	5938 (1)	3006 (1)	1.8 (1)	C46	−1185 (9)	8428 (5)	628 (6)	3.4 (4)
O1	1301 (6)	7004 (3)	2330 (3)	2.9 (2)	C51	1361 (8)	8547 (5)	416 (5)	1.7 (3)
O2	4092 (6)	7715 (3)	786 (3)	2.7 (2)	C52	1492 (10)	9177 (5)	481 (6)	3.6 (4)
O3	370 (7)	6676 (4)	45 (4)	3.9 (3)	C53	1602 (11)	9547 (5)	−34 (7)	4.2 (5)
O4	4998 (6)	7197 (3)	2004 (3)	3.3 (3)	C54	1576 (9)	9292 (7)	−606 (6)	3.7 (4)
O5	1942 (6)	5650 (4)	2729 (4)	3.2 (3)	C55	1471 (10)	8666 (6)	−674 (6)	3.7 (4)
O6	4996 (7)	4824 (4)	1709 (4)	4.6 (3)	C56	1345 (10)	8304 (5)	−168 (6)	3.1 (4)
N1	2089 (7)	3210 (4)	1813 (4)	2.6 (3)	C61	4945 (8)	5248 (5)	3479 (5)	1.9 (3)
C1	1590 (9)	7037 (5)	1840 (5)	2.4 (3)	C62	5510 (9)	4713 (5)	3340 (5)	2.7 (4)
C2	3264 (9)	7471 (4)	917 (4)	1.4 (3)	C63	5492 (9)	4189 (5)	3695 (6)	3.1 (4)
C3	1012 (9)	6853 (5)	466 (5)	2.5 (4)	C64	4909 (10)	4215 (5)	4213 (6)	3.4 (4)
C4	4573 (8)	6703 (5)	2036 (5)	2.0 (3)	C65	4322 (10)	4732 (6)	4339 (6)	4.1 (4)
C5	2724 (9)	5788 (5)	2488 (5)	2.4 (4)	C66	4340 (9)	5247 (5)	3976 (6)	3.2 (4)
C6	4574 (9)	5290 (5)	1857 (5)	2.3 (3)	C71	6631 (8)	5975 (5)	3011 (5)	2.1 (3)
C11	3752 (9)	6074 (4)	561 (5)	2.1 (3)	C72	7408 (9)	5817 (6)	3518 (5)	3.2 (4)
C12	4957 (10)	6091 (5)	651 (5)	3.0 (4)	C73	8589 (9)	5860 (6)	3515 (6)	3.6 (4)
C13	5630 (10)	6001 (6)	176 (6)	4.2 (4)	C74	9050 (8)	6044 (5)	2990 (6)	3.0 (4)
C14	5120 (11)	5890 (5)	−395 (6)	3.3 (4)	C75	8316 (10)	6177 (5)	2477 (6)	2.8 (4)
C15	3910 (11)	5893 (5)	−516 (5)	3.4 (4)	C76	7108 (9)	6140 (5)	2483 (5)	2.6 (4)
C16	3252 (9)	5989 (5)	−40 (5)	2.5 (3)	C81	4712 (9)	6567 (5)	3522 (5)	2.0 (3)
C21	1778 (8)	5557 (5)	1035 (5)	1.7 (3)	C82	5365 (9)	6676 (5)	4088 (5)	3.2 (4)
C22	1959 (9)	5042 (5)	683 (5)	2.6 (4)	C83	5053 (10)	7127 (6)	4474 (5)	3.2 (4)
C23	1077 (11)	4617 (5)	551 (5)	3.0 (4)	C84	4078 (10)	7491 (5)	4309 (5)	2.6 (4)
C24	47 (10)	4669 (6)	785 (6)	3.6 (4)	C85	3459 (9)	7396 (5)	3761 (5)	2.5 (4)
C25	−117 (9)	5157 (6)	1146 (6)	3.3 (4)	C86	3761 (9)	6939 (5)	3371 (5)	2.5 (3)
C26	734 (9)	5603 (5)	1280 (5)	2.5 (4)	C91	3181 (9)	2897 (5)	2086 (5)	3.4 (4)
C31	1399 (8)	8527 (4)	1725 (5)	1.5 (3)	C92	4289 (10)	3205 (6)	1931 (6)	4.5 (4)
C32	653 (8)	9008 (5)	1835 (5)	2.0 (3)	C93	1957 (10)	3181 (6)	1114 (6)	3.7 (4)
C33	939 (10)	9413 (5)	2329 (5)	2.6 (4)	C94	1905 (12)	2541 (7)	842 (6)	5.9 (5)
C34	1966 (10)	9331 (6)	2709 (6)	3.3 (4)	C95	1080 (10)	2864 (6)	2041 (6)	4.0 (4)
C35	2691 (8)	8841 (5)	2606 (5)	2.5 (3)	C96	−120 (9)	3051 (6)	1759 (5)	3.8 (4)
C36	2397 (8)	8443 (5)	2130 (5)	2.0 (3)	C97	2056 (10)	3889 (5)	1990 (6)	3.5 (4)
C41	−493 (8)	7992 (5)	958 (5)	2.0 (3)	C98	2319 (10)	4023 (6)	2670 (6)	4.7 (4)

[a] Anisotropically refined atoms are given in the form of the isotropic equivalent thermal parameter defined as $^4/_3[a^2B_{11} + b^2B_{22} + c^2B_{33} + ab(\cos\gamma)B_{12} + ac(\cos\beta)B_{13} + bc(\cos\alpha)B_{23}]$.

Evidence for a four-component ECEC pathway[41] was not observed for any of the complexes studied nor was there evidence to suggest the presence of two different 34e complexes on reduction of 33e $Fe_2(CO)_6(PR_3)(\mu\text{-}PPh_2)$ complexes (Scheme V).

Kinetic Studies of 33e and 34e Dinuclear Iron Complexes. Quantification of the homogeneous kinetic parameters for CO substitution by PR_3 using cyclic voltammetry[42] would be tedious because of the observed non-Nernstian electrochemical behavior and the slow heterogeneous[43] electron transfer in dichloromethane solvent. Since the double potential step chronocoulometric (DPSCC) method[44] has been previously employed by our group to obtain thermodynamic and kinetic parameters for Lewis base induced disproportionation of 17e Fe(I) cation radicals,[16] it became the technique of choice to extract kinetic data for CO substitution by PR_3 at 33e $Fe_2(CO)_7(\mu\text{-}PPh_2)$. The double potential step experiment can be described by examining Figure 8A. The experiment consists of stepping the potential from an initial value E_i (labeled 1), where no electrode reaction proceeds, to a final value E_f (labeled 2), where the species of kinetic interest, 33e $Fe_2(CO)_7(\mu\text{-}PPh_2)$, forms at the electrode surface. After holding the potential at E_f for a time τ, it is stepped back to E_i and maintained there for the same interval τ. During this period a portion of the reactant generated at E_f (compound **1**) is converted back to starting material (compound **6**). The charge that passes through the electrode during each time interval is measured. The ratio of the charges provides a measure (after correction for background contributions in blank experiments) of the CO substitution reaction that consumes the 33e complex **1** generated at E_f. In the absence of a phosphorus Lewis base, the charge ratio Q_R/Q_F was within 2% of the expected value of 0.586[44] for a chemically reversible redox couple, and independent of step duration τ. Choosing E_i to be sufficiently negative (labeled 3, Figure 8A) and pulsing again to E_f also gives charge ratios close to 0.586 and independent of step duration. This shows that the only reaction consuming **1** at E_f (within times τ) generates the monophosphine-substituted 33e radical $Fe_2(CO)_6(PR_3)(\mu\text{-}PPh_2)$ (**2a**).

The mechanistic scheme for substitution corresponds to the EC case, an electrode reaction, eq 11 (E), followed by a single chemical reaction, eq 12 (C), which may or may not be reversible. Working

$$\text{(E)}\quad [Fe_2(CO)_6(\mu\text{-}CO)(\mu\text{-}PPh_2)]^- \underset{E_i}{\overset{E_f}{\rightleftharpoons}} Fe_2(CO)_7(\mu\text{-}PPh_2) + e^- \qquad (11)$$

$$\text{(C)}\quad Fe_2(CO)_7(\mu\text{-}PPh_2) + Nu \underset{k_{-1}}{\overset{k_1}{\rightleftharpoons}} Fe_2(CO)_6(Nu)(\mu\text{-}PPh_2) + CO \qquad (12)$$

$$Nu = PR_3$$

curves for the EC mechanism that plot the expected values of the charge ratio Q_R/Q_F as a function of the dimensionless kinet.c

(42) (a) Nicholson, R. S.; Shain, I. *Anal. Chem.* **1964**, *36*, 706. (b) Nicholson, R. S. *Ibid.* **1966**, *38*, 1406. (c) Polcyn, D. S.; Shain, I. *Electrochim. Acta* **1967**, *12*, **999**. (d) Saveant, J. M.; Vianello, E. *Ibid.* **1966**, *38*, 376. (e) Mastragostino, M.; Nadjo, L.; Saveant, J. M. *Ibid.* **1968**, *13*, 721. (f) Mastragostino, M.; Saveant, J. M. *Ibid.* **1968**, *13*, 751. (g) Olmstead, M. L.; Nicholson, R. S. *Anal. Chem.* **1969**, *41*, 862. (h) Nadjo, L.; Saveant, J. M. *Electrochim. Acta* **1971**, *16*, 87. (i) Feldberg, S. W. *J. Phys. Chem.* **1971**, *75*, 2377. (j) Feldberg, S. W.; Jeftic, L. *Ibid.* **1972**, *76*, 2349.

(43) (a) Feldberg, S. W. In *Electroanalytical Chemistry*; Bard, A. J., Ed.; Dekker: New York, 1969; Vol. 3, p 199. (b) Feldberg, S. W. *Computer Applications in Analytical Chemistry*; Mark, H. B., Ed.; Dekker: New York, 1972; Vol. 2, Chapter 7.

(44) (a) Christie, J. H.; Anson, F. C.; Lauer, G.; Osteryoung, R. A. *Anal. Chem.* **1963**, *35*, 1979. (b) Bard, A. J.; Faulkner, L. R. *Electrochemical Methods*; Wiley: New York, 1980. (c) Christie, J. H.; Osteryoung, R. A.; Anson, F. C. *J. Electroanal. Chem.* **1978**, *50*, 116. (d) Christie, J. H. *Ibid.* **1967**, *13*, 79. (e) Anson, F. C. *Acc. Chem. Res.* **1975**, *18*, 400, and references therein.

Table XIII. Selected Bond Distances (Å) and Angles (deg) for $Et_4N[Fe_2(CO)_6(PPh_3)_2(\mu\text{-}PPh_2)]$ (**7a**)

	Distances		
Fe1···Fe2	3.961 (1)	P2-C31	1.851 (10)
Fe1-P1	2.315 (3)	P2-C41	1.828 (10)
Fe1-P2	2.198 (3)	P2-C51	1.838 (10)
Fe2-P1	2.292 (3)	P3-C61	1.830 (11)
Fe2-P3	2.192 (3)	P3-C71	1.845 (9)
Fe1-C1	1.764 (12)	P3-C81	1.840 (10)
Fe1-C2	1.780 (11)	O1-C1	1.168 (11)
Fe1-C3	1.746 (12)	O2-C2	1.161 (10)
Fe2-C4	1.751 (10)	O3-C3	1.186 (11)
Fe2-C5	1.793 (11)	O4-C4	1.183 (10)
Fe2-C6	1.743 (11)	O5-C5	1.142 (11)
P1-C11	1.840 (10)	O6-C6	1.184 (11)
P1-C21	1.867 (10)		
	Angles		
P1-Fe1-P2	176.0 (1)	Fe1-P1-C21	107.8 (3)
P1-Fe2-P3	170.3 (1)	Fe2-P1-C11	110.7 (3)
P1-Fe1-C1	87.9 (3)	Fe2-P1-C21	109.5 (3)
P1-Fe1-C2	89.9 (3)	Fe1-P2-C31	116.2 (3)
P1-Fe1-C3	92.2 (3)	Fe1-P2-C41	114.5 (4)
P2-Fe1-C1	88.7 (3)	Fe1-P2-C51	117.7 (4)
P2-Fe1-C2	90.3 (3)	Fe2-P3-C61	117.8 (3)
P2-Fe1-C3	91.3 (3)	Fe2-P3-C71	117.6 (4)
P1-Fe2-C4	85.2 (4)	Fe2-P3-C81	113.2 (4)
P1-Fe2-C5	92.5 (3)	C11-P1-C21	100.5 (5)
P1-Fe2-C6	94.6 (4)	C31-P2-C41	101.9 (4)
P3-Fe2-C4	85.9 (3)	C31-P2-C51	102.5 (5)
P3-Fe2-C5	89.4 (3)	C41-P2-C51	101.7 (5)
P3-Fe2-C6	93.7 (4)	C61-P3-C71	99.1 (5)
C1-Fe1-C2	122.8 (5)	C61-P3-C81	102.9 (5)
C1-Fe1-C3	120.4 (5)	C71-P3-C81	104.0 (5)
C2-Fe1-C3	116.7 (5)	Fe1-C1-O1	176.3 (9)
C4-Fe2-C5	126.3 (5)	Fe1-C2-O2	177 (1)
C4-Fe2-C6	123.9 (5)	Fe1-C3-O3	180 (1)
C5-Fe2-C6	109.8 (5)	Fe2-C4-O4	177 (1)
Fe1-P1-Fe2	118.6 (1)	Fe2-C5-O5	177 (1)
Fe1-P1-C11	108.1 (3)	Fe2-C6-O6	177 (1)

parameter $k_1[Nu]\tau$ are available[45] for various values of $k_{-1}/k_1[Nu]$. Extensive DPSCC experiments, with PPh_3 and PCy_3 as nucleophiles, show that the charge ratios obtained decrease with increasing pulse width and increasing phosphine concentration. The ratio Q_R/Q_F approaches zero at moderate nucleophile concentrations and long pulse widths. Such behavior requires $k_{-1}/k_1[Nu] < 10^{-2}$. Otherwise a lower limit to Q_R/Q_F would be observed, because k_{-1} produces an electroactive species (complex **1**) during the reverse step of the experiment, which would give a measurable value for Q_R. Parts A and B of Figure 9 show the experimental values of Q_R/Q_F, obtained at five different nucleophile concentrations, fit to the working curve for the EC mechanism, where the parameter $k_{-1}/k_1[Nu] = 0$. This special case of the EC mechanism is often referred to as EC_i. The values of k_1 evaluated from the data points in parts A and B of Figure 9 are consistent for each nucleophile.

One must realize that the experimental data obtained for both nucleophiles will fit any EC working curve where $0 \le k_{-1}/k_1[Nu] \le 10^{-2}$. However, ESR experiments show that reaction of 1.5 equiv of phosphine ligand with complex **1** results in complete conversion of **1** to the 33e phosphine-substituted product. Thus, the assumption that k_{-1} is negligible relative to $k_1[Nu]$ under pseudo-first-order conditions appears valid (even for L = PPh_3).

The second-order rate constants k_1 for CO substitution at $Fe_2(CO)_7(\mu\text{-}PPh_2)$ by PPh_3 and PCy_3 were determined to be 44.2 ± 2.4 and 23.3 ± 2.5 M^{-1} s^{-1}, respectively. Plots of k_{obs} vs nucleophile concentration for the reaction between **1** and PPh_3 and PCy_3 are shown in Figure 10. A first-order dependence in nucleophile, with no nucleophile-independent (i.e. dissociative) reaction pathway, yields the rate law of eq 13.

$$-d[Fe_2(CO)_7(\mu\text{-}PPh_2)]/dt = k_1[Fe_2(CO)_7(\mu\text{-}PPh_2)][Nu] \quad (13)$$

(45) Hanafey, M. K.; Scott, R. L.; Ridgway, T. H.; Reilley, C. N. *Anal. Chem.* **1978**, *50*, 116.

Table XIV. Atomic Coordinates (×10000) and Temperature Factors for $FeCo(CO)_5[P(OMe)_3]_2(\mu\text{-}PPh_2)$ (**9a**)

atom	*x*	*y*	*z*	*B*(iso)[a]
Co1	1140.2 (5)	2159.7 (4)	3168.8 (4)	1.6 (1)
Fe1	3005.8 (6)	995.7 (5)	2290.0 (4)	1.7 (1)
P1	2516.4 (10)	2760.8 (8)	1977.8 (8)	1.5 (1)
P2	3153.7 (12)	−790.0 (9)	2653.6 (9)	2.3 (1)
P3	−235.4 (11)	3245.8 (9)	2822.5 (8)	2.0 (1)
O1	4384 (4)	1935 (3)	4344 (3)	3.9 (1)
O2	5132 (4)	1257 (4)	786 (3)	4.7 (1)
O3	762 (3)	−215 (3)	956 (2)	2.8 (1)
O4	−812 (4)	88 (3)	3270 (3)	4.3 (1)
O5	1809 (4)	2936 (3)	5448 (2)	4.1 (1)
O6	2037 (3)	−1507 (3)	3298 (2)	3.3 (1)
O7	4367 (4)	−1032 (3)	3340 (3)	3.8 (1)
O8	3100 (3)	−1624 (2)	1556 (2)	3.1 (1)
O9	−989 (3)	3108 (3)	1678 (2)	3.0 (1)
O10	180 (3)	4651 (3)	2787 (2)	3.1 (1)
O11	−1367 (3)	3141 (3)	3687 (2)	2.9 (1)
C1	3799 (4)	1588 (4)	3555 (4)	2.5 (1)
C2	4296 (5)	1125 (4)	1379 (4)	2.7 (1)
C3	1629 (4)	284 (3)	1477 (3)	2.0 (1)
C4	−22 (4)	892 (4)	3209 (3)	2.4 (1)
C5	1626 (4)	2653 (4)	4542 (3)	2.3 (1)
C6	1780 (6)	−1113 (5)	4398 (4)	4.8 (2)
C7	5651 (6)	−632 (6)	3050 (6)	5.6 (2)
C8	3016 (7)	−2893 (4)	1513 (5)	5.2 (2)
C9	−1370 (6)	1992 (5)	1068 (4)	4.6 (2)
C10	810 (5)	5375 (4)	3693 (4)	3.3 (1)
C11	−2483 (5)	3726 (5)	3585 (4)	4.2 (2)
C21	3798 (4)	4020 (3)	2281 (3)	1.7 (1)
C22	4640 (4)	4408 (4)	1479 (3)	2.1 (1)
C23	5632 (4)	5343 (4)	1714 (4)	2.8 (1)
C24	5803 (4)	5913 (4)	2754 (4)	2.6 (1)
C25	4984 (4)	5537 (4)	3566 (3)	2.6 (1)
C26	3997 (4)	4590 (3)	3330 (3)	2.2 (1)
C31	2045 (4)	2961 (3)	581 (3)	1.7 (1)
C32	1588 (4)	3995 (4)	390 (3)	2.2 (1)
C33	1137 (4)	4154 (4)	−645 (3)	2.8 (1)
C34	1163 (4)	3283 (4)	−1491 (3)	2.8 (1)
C35	1642 (5)	2268 (4)	−1315 (3)	2.7 (1)
C36	2107 (4)	2103 (3)	−286 (3)	2.2 (1)

[a] Anisotropically refined atoms are given in the form of the isotropic equivalent thermal parameter defined as $^4/_3[a^2B_{11} + b^2B_{22} + c^2B_{33} + ab(\cos\gamma)B_{12} + ac(\cos\beta)B_{13} + bc(\cos\alpha)B_{23}]$.

Second-order rate constants k_1 for eq 13 were determined for a series of phosphines (Table XVII) using the electrochemical technique discussed. The dependence of the rate of CO substitution on the particular nucleophile agrees with the proposed associative pathway. For the series Nu = $PPh_{3-n}Me_n$, where the phosphine cone angle[46] (θ) decreases with increasing σ-donicity (pK_a) throughout the series, we find a steady increase in the rate of carbonyl substitution (k_1). Although PCy_3 is the most electron-rich nucleophile ($pK_a = 9.7$), it also possesses the largest cone angle in the series ($\theta = 172°$) and the smallest measured value of k_1. Conversely, unhindered $PPh(OMe)_2$ ($\theta = 115°$) and $P(OMe)_3$ ($\theta = 107°$), with pK_a's similar to that of PPh_3, yield values of the pseudo-first-order rate constant k_1 over 5 times greater than those for PPh_3. The data suggest that both the steric and electronic properties of the incoming nucleophile determine the rate.

In addition to the dependence of the rate of carbonyl substitution on the steric and electronic properties of the entering nucleophile, and the lack of a nucleophile-independent reaction pathway, the derived activation parameters further support an associative mechanism. Rates of reaction between $Fe_2(CO)_7(\mu\text{-}PPh_2)$ and PPh_3 were determined at temperatures over a 45 °C range (+20 to −25 °C). An Eyring plot of the data obtained (Table XVIII) yields an enthalpy of activation ($\Delta H^\ddagger$) of 9.9 ± 1.0 kcal mol^{-1} and an entropy of activation ($\Delta S^\ddagger$) of −17.7 ± 3.9 cal mol^{-1} K^{-1}. Small enthalpies of activation and large negative entropies of activation often signal a transition state of higher coordination number than the ground state.[47,48] These values closely resemble

(46) Tolman, C. A. *Chem. Rev.* **1977**, *77*, 313.

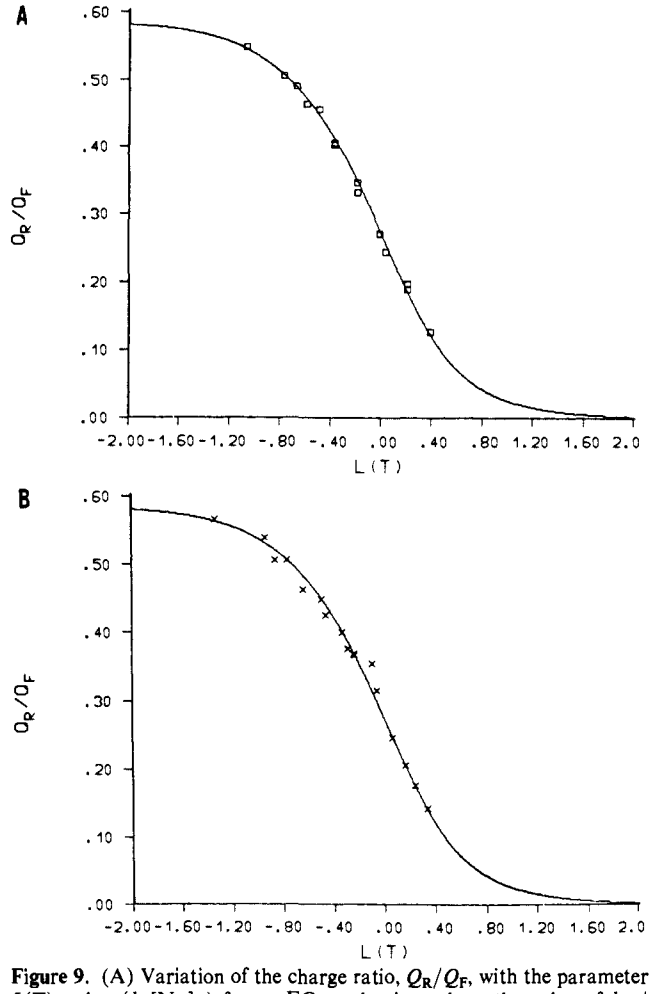

Figure 9. (A) Variation of the charge ratio, Q_R/Q_F, with the parameter $L(T) = \log (k_1[Nu]\tau)$ for an EC mechanism where the value of $k_{-1}/k_1[Nu]$ equals zero. The solid line represents the working curve for the mechanism and the boxes represent the experimental responses obtained at various nucleophile concentrations between 10 and 75 mM and pulse widths τ of 200, 500, and 750 ms. Experimental system: $[Et_4N[Fe_2(CO)_6(\mu\text{-}CO)(\mu\text{-}PPh_2)]] = 1 \times 10^{-3}$ M; [TBAHFP] = 0.15 M; temperature 20 °C; solvent, CH_2Cl_2; $E_i = -0.80$ V; $E_f = -0.10$ V (vs a Ag/0.1 M $AgNO_3$ reference electrode); Nu = PPh_3 and k_1(evald) = 44.2 ± 2.4 M^{-1} s^{-1}. (B) Same as in (A) above, except the crosses represent experimental data obtained at nucleophile concentrations between 10 and 125 mM. Experimental system: same as in (A) above except Nu = PCy_3 and k_1(evald) = 23.3 ± 2.5 M^{-1} s^{-1}.

the $\Delta H^{\ddagger} = 9.8 \pm 0.3$ kcal/mol and $\Delta S^{\ddagger} = -21 \pm 1$ cal/mol·K obtained[16] for associative attack of pyridine at 17e $[Fe(CO)_3(PPh_3)_2]^+$.

Previous studies[12] showed that 17e $V(CO)_6$ undergoes associative CO substitution 10^{10} times more rapidly than 18e $Cr(CO)_6$. Pentacoordinate 17e $[Fe(CO)_3L_2]^+$ radical cations undergo CO substitution at least 10^9 times faster than neutral 18e $Fe(CO)_3L_2$ complexes.[16] There is little knowledge about the degree of rate enhancement for open vs closed shell binuclear carbonyl complexes.[16] Using FTIR spectroscopy to measure the disappearance of the 34e anion $[Fe_2(CO)_6(\mu\text{-}CO)(\mu\text{-}PPh_2)]^-$ (**6**), we find that the rate of CO substitution by PPh_3 is 10^5–10^6 times slower than that for the 33e radical **1** (Table XIX). Because complexes **1** and **6** are not isostructural, one cannot determine whether the accelerated rate of carbonyl substitution at electron-deficient **1** results entirely from electronic factors or from a combination of electronic and geometric factors. Since trace oxidants or reductants could catalyze reactions of the 34e system, the factor of 10^5–10^6 represents a lower limit. Different steric constraints may be placed on the entering nucleophile in 34e **6** since two groups are bridging the two iron centers (CO and PR_2). Therefore, we examined the rate of CO substitution by PPh_3 at 34e $FeCo(CO)_7(\mu\text{-}PPh_2)$ (Table XIX), an electronically saturated compound that is isostructural to **1**. The rate of CO substitution at $FeCo(CO)_7(\mu\text{-}PPh_2)$ is similar to that at **6**, which suggests that

Table XV. Selected Bond Distances (Å) and Angles (deg) for $FeCo(CO)_5[P(OMe)_3]_2(\mu\text{-}PPh_2)$ (**9a**)

Distances			
Co1–Fe1	2.7061 (10)	P2–O8	1.579 (3)
Co1–P1	2.159 (1)	P3–O9	1.594 (3)
Co1–P3	2.107 (1)	P3–O10	1.613 (3)
Co1–C4	1.756 (4)	P3–O11	1.602 (3)
Co1–C5	1.780 (4)	P1–C21	1.824 (4)
Fe1–P1	2.234 (1)	P1–C31	1.836 (4)
Fe1–P2	2.171 (1)	O1–C1	1.150 (5)
Fe1–C1	1.786 (4)	O2–C2	1.149 (5)
Fe1–C2	1.765 (5)	O3–C3	1.150 (5)
Fe1–C3	1.789 (4)	O4–C4	1.151 (5)
P2–O6	1.591 (3)	O5–C5	1.142 (5)
P2–O7	1.592 (4)		
Angles			
Fe1–Co1–P1	53.23 (3)	C2–Fe1–C3	104.8 (2)
Fe1–Co1–P3	143.71 (4)	Co1–P1–Fe1	76.04 (4)
Fe1–Co1–C4	95.4 (1)	Co1–P3–O9	122.2 (1)
Fe1–Co1–C5	107.3 (1)	Co1–P3–O10	121.1 (1)
P1–Co1–P3	96.35 (5)	Co1–P3–O11	110.2 (1)
P1–Co1–C4	133.7 (1)	Co1–P1–C21	122.5 (1)
P1–Co1–C5	114.7 (1)	Co1–P1–C31	123.1 (1)
P3–Co1–C4	94.0 (2)	Fe1–P2–O6	120.0 (1)
P3–Co1–C5	103.5 (1)	Fe1–P2–O7	119.9 (1)
C4–Co1–C5	106.4 (2)	Fe1–P2–O8	109.2 (1)
Co1–Fe1–P1	50.73 (3)	Fe1–P1–C21	116.2 (1)
Co1–Fe1–P2	121.02 (4)	Fe1–P1–C31	117.5 (1)
Co1–Fe1–C1	80.7 (1)	O6–P2–O7	98.5 (2)
Co1–Fe1–C2	142.6 (1)	O6–P2–O8	100.4 (2)
Co1–Fe1–C3	79.5 (1)	O7–P2–O8	106.5 (2)
P1–Fe1–P2	170.75 (8)	O9–P3–O10	92.3 (2)
P1–Fe1–C1	91.7 (1)	O9–P3–O11	103.9 (2)
P1–Fe1–C2	91.8 (1)	O10–P3–O11	104.2 (2)
P1–Fe1–C3	90.0 (1)	C21–P1–C31	101.1 (2)
P2–Fe1–C1	90.7 (1)	Co1–C4–O4	177.0 (4)
P2–Fe1–C2	96.4 (2)	Co1–C5–O5	173.0 (4)
P2–Fe1–C3	83.8 (1)	Fe1–C1–O1	175.2 (4)
C1–Fe1–C2	102.1 (2)	Fe1–C2–O2	177.2 (4)
C1–Fe1–C3	152.9 (2)	Fe1–C3–O3	177.3 (4)

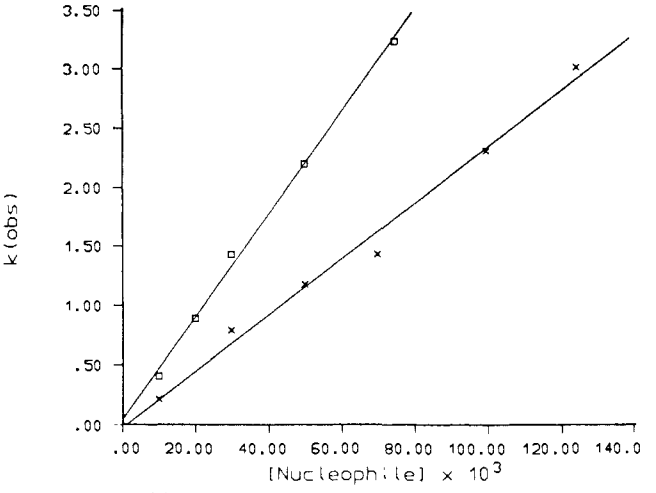

Figure 10. Plot of k_{obs} vs nucleophile concentration for $Fe_2(CO)_7(\mu\text{-}PPh_2)$ in CH_2Cl_2 at 20 °C. Crosses and boxes correspond to the data obtained for PCy_3 and PPh_3 nucleophiles, respectively. Rates were measured using double potential step chronocoulometry.

(47) (a) Wawersik, H.; Basolo, F. *J. Am. Chem. Soc.* **1967**, *89*, 4626. (b) Schuster-Woldan, H. G.; Basolo, F. *Ibid.* **1966**, *88*, 1657. (c) Thorsteinson, E. M.; Basolo, F. *Ibid.* **1966**, *88*, 3929. (d) Dobson, G. R. *Acc. Chem. Res.* **1976**, *19*, 300. (e) Darensbourg, D. J. *Adv. Organomet. Chem.* **1982**, *21*, 131.

(48) (a) Basolo, F.; Pearson, R. G. *Mechanisms of Inorganic Reactions*, 2nd ed.; Wiley: New York, 1967; pp 234. (b) Espenson, J. H. *Chemical Kinetics and Reaction Mechanisms*, 1st ed.; McGraw-Hill: New York, 1981; pp 116.

(49) Streuli, C. A. *Anal. Chem.* **1959**, *31*, 1652. Henderson, W. A.; Streuli, C. A. *J. Am. Chem. Soc.* **1962**, *82*, 5791.

Table XVI. Cyclic Voltammetric Data for $Fe_2(CO)_xL_y(\mu\text{-}PPh_2)$ Complexes

compd	$E_{1/2}$,[d,e] mV	E_{pc},[f] mV	ΔE_p,[g] mV	i_{pa}/i_{pc}[h]	redox couple
$Fe_2(CO)_7(\mu\text{-}PPh_2)$[a]	−624	−669	91	1.0	0/1−
$Et_4N[Fe_2(CO)_6(\mu\text{-}CO)(\mu\text{-}PPh_2)]$[a]	−624	−669	91	1.0	1−/0
$Fe_2(CO)_6[P(OMe)_3](\mu\text{-}PPh_2)$[a]	−965	−1012	94	1.0	0/1−
$Fe_2(CO)_6[PPh(OMe)_2](\mu\text{-}PPh_2)$[b]	−985	−1047	124	0.8	0/1−
$Fe_2(CO)_6(PPh_3)(\mu\text{-}PPh_2)$	−990	−1027	74	1.0	0/1−
$Fe_2(CO)_6(PPh_2Me)(\mu\text{-}PPh_2)$[b]	−990	−1035	90	1.0	0/1−
$Fe_2(CO)_6(PPhMe_2)(\mu\text{-}PPh_2)$[b]	−970	−1128	317	0.6	0/1−
$Fe_2(CO)_6(PMe_3)(\mu\text{-}PPh_2)$[b]	−920	−1089	338	0.7	0/1−
$Fe_2(CO)_6(PCy_3)(\mu\text{-}PPh_2)$[b]	−1072	−1115	86	0.4	0/1−
$Et_4N[Fe_2(CO)_6[P(OMe)_3]_2(\mu\text{-}PPh_2)]$[c]	−881	−1183	605	1.6	1−/0
$FeCp_2$[a]	110	70	80	1.0	0/1+

[a] Experimental conditions: [compound] = 1×10^{-3} M; supporting electrolyte, 0.15 M tetrabutylammonium hexafluorophosphate (TBAHFP); temperature 20 °C; scan rate 400 mV/s; solvent, CH_2Cl_2; IR compensated. [b] Generated via electrochemical oxidation of $Et_4N[Fe_2(CO)_6(\mu\text{-}CO)(\mu\text{-}PPh_2)]$ to $Fe_2(CO)_7(\mu\text{-}PPh_2)$ in the presence of the appropriate PR_3 under pseudo-first-order conditions. Experimental conditions: same as above. [c] This species loses CO and forms a metal–metal bond upon 1e chemical oxidation to generate $Fe_2(CO)_5[P(OMe)_3]_2(\mu\text{-}PPh_2)$. The intervening chemical processes between oxidation and reduction of this complex account for the unusually large value of ΔE_p. Experimental conditions: same as above. [d] Half-wave potentials relative to a Ag/0.1 M $AgNO_3$ reference electrode in acetonitrile. [e] Platinum disk or glassy carbon disk working electrodes used. [f] Cathodic peak position. [g] Separation of anodic and cathodic peak positions. [h] Ratio of anodic to cathodic peak current.

Table XVII. Second-Order Rate Constants for Substitution of Carbon Monoxide by PR_3 Nucleophiles at the 33e $Fe_2(CO)_7(\mu\text{-}PPh_2)$ Radical at 20 °C

phosphine	k_1,[a] $M^{-1}\ s^{-1}$	log k_1	phosphine cone angle, deg	pK_a
PCy_3[b]	23.3 ± 2.5	1.37	170	9.70[d]
PPh_3[b]	44.2 ± 2.4	1.65	145	2.73[d]
PPh_2Me[b]	350	2.54	136	4.65[d]
$PPhMe_2$[b]	950	2.98	122	6.49[d]
PMe_3[b]	1100	3.04	118	8.65[d]
$PPh(OMe)_2$[b]	225	2.35	115	2.64[e]
$P(OMe)_3$[b]	240	2.38	107	2.60[d]
$P(OMe)_3$[c]	25.3	1.40	107	2.60[d]

[a] Rate measured using double potential step chronocoulometry and fitting the experimental responses to the theoretical working curve for an EC_i mechanism. Rates greater than 200 $M^{-1}\ s^{-1}$ should be considered approximate since only low phosphine concentrations were used (10–20-fold molar excess) to ensure that Q_R/Q_F did not become too small to measure accurately. [b] Rate reported is for the substitution of a single carbon monoxide by PR_3 at $Fe_2(CO)_7(\mu\text{-}PPh_2)$ to give the product $Fe_2(CO)_6(PR_3)(\mu\text{-}PPh_2)$. [c] Rate reported is for the substitution of a single carbon monoxide by PR_3 at $Fe_2(CO)_6(PR_3)(\mu\text{-}PPh_2)$ to give the product $Fe_2(CO)_5(PR_3)_2(\mu\text{-}PPh_2)$. [d] pK_a of the phosphonium–phosphine in water.[49] [e] Estimate based on the pK_a values of $P(OMe)_3$ and PPh_3.

Table XVIII. Data[a,b] for Eyring Plot for the Reaction between $Fe_2(CO)_7(\mu\text{-}PPh_2)$ and PPh_3

$T^{-1} \times 10^3$, K^{-1}	ln (k_1/T)	$T^{-1} \times 10^3$, K^{-1}	ln (k_1/T)
3.401	−1.895	3.825	−4.096
3.534	−2.789	4.035	−5.308
3.661	−3.518		

[a] Rates obtained using double potential step chronocoulometry. [b] $\Delta H^{\ddagger} = 9.9 \pm 1.0$ kcal mol^{-1}; $\Delta S^{\ddagger} = -17.7 \pm 3.9$ cal $mol^{-1}\ K^{-1}$.

Table XIX. Second-Order Rate Constants for CO Substitution at Dinuclear Phosphido-Bridged Carbonyl Complexes at 20 °C

complex	CVE[a]	k_1, $M^{-1}\ s^{-1}$	rel rate
$[Fe_2(CO)_6(\mu\text{-}CO)(\mu\text{-}PPh_2)][Et_4N]$	34	$1.4 \pm 0.1 \times 10^{-4}$ [b]	1.5
$FeCo(CO)_7(\mu\text{-}PPh_2)$	34	$9.2 \pm 0.4 \times 10^{-5}$ [b]	1
$Fe_2(CO)_7(\mu\text{-}PPh_2)$	33	$4.42 \pm 0.24 \times 10^{1}$ [c]	5×10^5

[a] Cluster valence electron count. [b] Rate measured by monitoring the change in infrared absorption spectrum with time. [c] Rate measured using double potential step chronocoulometry.

the rate acceleration of $\sim 10^5$–10^6 for CO substitution at 33e $Fe_2(CO)_7(\mu\text{-}PPh_2)$ (**1**) versus that of its 34e counterpart $Et_4N[Fe_2(CO)_6(\mu\text{-}CO)(\mu\text{-}PPh_2)]$ (**6**) arises primarily from electronic differences.

Electrochemical Studies of 34e Dinuclear Iron–Cobalt Complexes. Electrochemical oxidation of the isostructural analogue

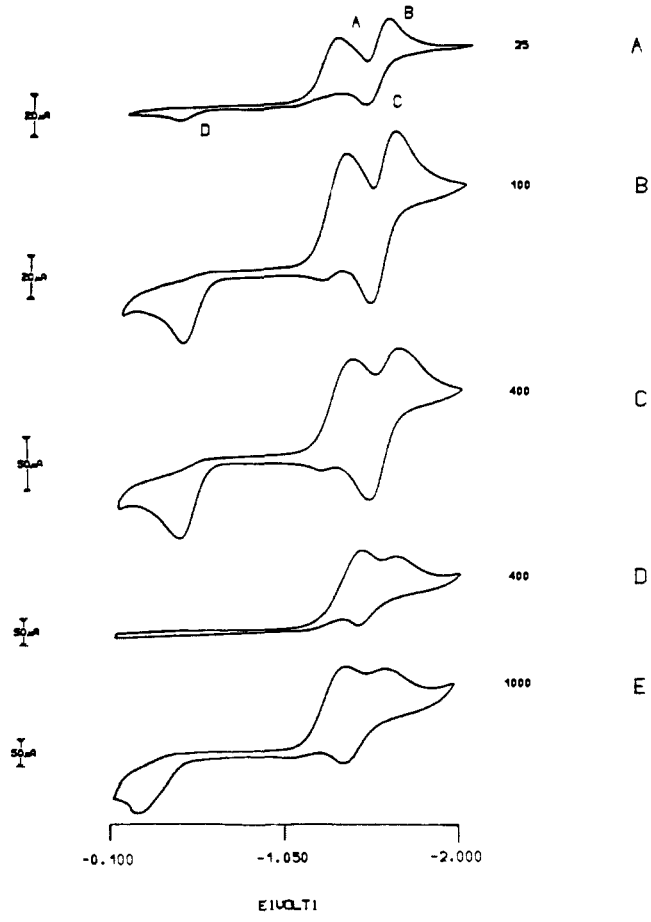

Figure 11. Cyclic voltammetric study of the reduction of $FeCo(CO)_7(\mu\text{-}PPh_2)$: (A) N_2 atmosphere, 25 mV/s; (B) N_2 atmosphere, 100 mV/s; (C) N_2 atmosphere, 400 mV/s; (D) CO atmosphere, 400 mV/s; (E) CO atmosphere, 1000 mV/s. Experimental conditions: $[FeCo(CO)_7(\mu\text{-}PPh_2)] = 1 \times 10^{-3}$ M; [TBAHFP] = 0.15 M; temperature 20 °C; solvent, THF; IR compensated.

of **1**, $FeCo(CO)_7(\mu\text{-}PPh_2)$ (**8**), to the 33e cation radical appears irreversible in the cyclic voltammogram at scan rates up to 10 V/s. More electron-rich analogues of $FeCo(CO)_7(\mu\text{-}PPh_2)$, such as $FeCo(CO)_6(PPh_3)(\mu\text{-}PPh_2)$, exhibit reversible 1e oxidations (Table XX) at a potential about 0.8 V more positive than that of the 34e anion **6**. Chemically generated $[FeCo(CO)_6(PPh_3)(\mu\text{-}PPh_2)]^+$ (**14**) could not be isolated and was characterized solely by ESR spectroscopy (see later).

The reductive electrochemistry of the phosphido-bridged iron–cobalt carbonyl compounds is complex. Three cathodic scan cyclic voltammograms of **8**, obtained at scan rates of 25, 100, and

Table XX. Cyclic Voltammetric Data[a] for Oxidation and Reduction of $FeCo(CO)_7(\mu\text{-}PPh_2)$ and $FeCo(CO)_6(PPh_3)(\mu\text{-}PPh_2)$

compd	E_{pa},[b] mV	E_{pc}, mV	redox couple
$FeCo(CO)_7(\mu\text{-}PPh_2)$	439	irrev[c]	0/1+
$FeCo(CO)_7(\mu\text{-}PPh_2)$	irrev	−1410	0/1−
$FeCo(CO)_6(\mu\text{-}PPh_2)^-$	−480	irrev	1−/0
$FeCo(CO)_6(\mu\text{-}PPh_2)^-$	−1530	−1650	1−/2−
$FeCo(CO)_6(PPh_3)(\mu\text{-}PPh_2)$	227	111	0/1+
$FeCo(CO)_6(PPh_3)(\mu\text{-}PPh_2)$	irrev	−1780[d]	0/1−
$FeCo(CO)_6(PPh_3)(\mu\text{-}PPh_2)^-$	−830	irrev	1−/0
$FeCo(CO)_5(PPh_3)(\mu\text{-}PPh_2)^-$	−1830	−1900[b]	1−/2−

[a] Experimental conditions: platinum disk working electrode; [complex] = 1×10^{-3} M; supporting electrolyte, 0.15 M tetrabutylammonium hexafluorophosphate (TBAHFP); temperature 20 °C; scan rate 200 mV/s; solvent for 0/1+ couples is CH_2Cl_2 and THF for others; *iR* compensated. [b] Half-wave potential referenced to a Ag/0.1 M $AgNO_3$ electrode in acetonitrile. [c] Oxidation irreversible up to a scan rate of 10 V/s. [d] Scan rate of 50 mV/s or less needed to resolve −1780 and −1900 peaks.

400 mV/s in tetrahydrofuran, are displayed in Figure 11. Two reduction waves, labeled A and B, appear on the negative scan, and two anodic waves, labeled C and D, appear on the reverse sweep. Scanning to a potential between A and B results in a cyclic voltammogram containing only waves A and D. Thus D arises directly from a 1e reduction of **8**, and wave C is coupled to B. Cyclic voltammetric parameters from Figure 11 are contained in Table XX.

It is noteworthy that the relative peak current of anodic wave D decreases with decreasing scan rate. One explanation for this behavior would be that A and D, though coupled, represent the reduction and oxidation, respectively, of two different species. At slow scan times the species corresponding to the peak current at D either isomerizes to an easily oxidized form or undergoes a chemical transformation. Repeated voltammetric scans at fast scan rates (>5 V/s) do not show additional cathodic waves, which implies that the species oxidized at D does not have a cathodic process.

Carrying out the reduction of **8** under 1 atm of CO produces the steady-state cyclic voltammetric responses shown in parts D–E of Figure 11. The voltammogram obtained at 400 mV/s (Figure 11D) under a CO atmosphere shows little current at the potential corresponding to the anodic wave D as compared to the voltammogram in Figure 11C. Increasing the sweep rate to 1000 mV/s (Figure 11E) causes the anodic wave D to reappear. Again, repeated cyclic voltammograms show no evidence of additional cathodic waves, while the carbon monoxide atmosphere does not significantly affect the B–C redox couple.

These data can best be accounted for by eq 14–16. Anodic wave D thus corresponds to oxidation of the unsaturated 33e radical anion $[FeCo(CO)_6(\mu\text{-}PPh_2)]^-$ (**12**) formed by rapid dissociative CO loss from $\mathbf{8}^-$. The reversibility of eq 15 would be consistent

$$\underset{\mathbf{8}}{FeCo(CO)_7(\mu\text{-}PPh_2)} + e^- \rightarrow \underset{\mathbf{8}^-}{[FeCo(CO)_7(\mu\text{-}PPh_2)]^{\bullet -}} \quad (14)$$

$$\underset{\mathbf{8}^-}{[FeCo(CO)_7(\mu\text{-}PPh_2)]^{\bullet -}} \underset{k_{-1}}{\overset{k_1}{\rightleftharpoons}} \underset{\mathbf{12}}{[FeCo(CO)_6(\mu\text{-}PPh_2)]^{\bullet -}} + CO \quad (15)$$

$$\underset{\mathbf{12}}{[FeCo(CO)_6(\mu\text{-}PPh_2)]^{\bullet -}} \underset{-e^-}{\overset{+e^-}{\rightleftharpoons}} \underset{\mathbf{13}}{[FeCo(CO)_6(\mu\text{-}PPh_2)]^{2-}} \quad (16)$$

with the decreased amounts of **12** present at slow scan rates and the cyclic voltammograms shown in parts D–E of Figure 11. The redox couple B–C is thus assigned to the chemically reversible 1e reduction of **12** (eq 16). Even though the electrochemical data provide only qualitative information, precedent exists for dissociative CO loss from a multinuclear hypervalent anionic carbonyl radical. Ohst and Kochi's study[17c] of an iron–rhodium carbonyl cluster showed simlar voltammetric responses for the 1e and 2e reductions of a tetranuclear complex. In addition, a CO atmosphere quenched the anodic wave attributed to the unsaturated

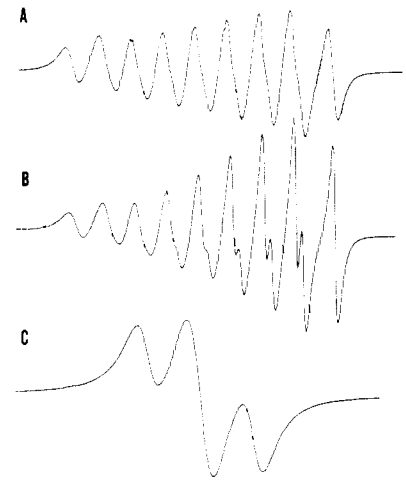

Figure 12. ESR spectra: of the $[FeCo(CO)_6(\mu\text{-}PPh_2)]^-$ radical anion in THF at (A) +25 °C and (B) −25 °C; (C) of $[FeCo(CO)_6(PPh_3)(\mu\text{-}PPh_2)]^+$ in CH_2Cl_2 at 25 °C.

radical anion, as we observe (Figure 11). Kochi's system[17c] was unambiguously defined since the unsaturated complex was chemically isolable. The striking similarity between the two systems suggests that dissociative CO loss may prove to be a general mechanistic pathway available to electronically and coordinatively saturated metal carbonyl clusters upon 1e reduction.

Examination of the reduction of monosubstituted $FeCo(CO)_6(PPh_3)(\mu\text{-}PPh_2)$ (**8a**) gives cyclic voltammograms similar to **8**, except all cathodic and anodic waves occur at more negative potentials (Table XX). A quenching of anodic wave D occurs for this complex at slow scan rates, when the reduction takes place under a CO atmosphere. Addition of other 2e donors, such as PR_3, to solutions of $FeCo(CO)_7(\mu\text{-}PPh_2)$ or $FeCo(CO)_6(PPh_3)(\mu\text{-}PPh_2)$ before the voltammetric reduction quenches the anodic wave D of the proposed unsaturated anion radical. Since anodic wave D resulting from the reduction of **8a** occurs at a different potential from wave D in the reduction of **8**, this suggests that primarily CO dissociates, rather than PPh_3, on reduction of **8a**.

Negative scan cyclic voltammograms of compound **6**, $Et_4N[Fe_2(CO)_6(\mu\text{-}CO)(\mu\text{-}PPh_2)]$, do not resemble those obtained for the phosphido-bridged iron–cobalt carbonyl dimers. Only one cathodic wave ($E_{pc} \sim -2650$ mV) and three irreversible anodic waves are seen. One anodic wave ($E_{pa} = -2210$ mV) disappears in the presence of an atmosphere of CO.

Generation and Spectroscopic Characterization of $[FeCo(CO)_6(\mu\text{-}PPh_2)]^-$ (12), $[FeCo(CO)_6(\mu\text{-}PPh_2)]^{2-}$ (13), and $[FeCo(CO)_6(PPh_3)(\mu\text{-}PPh_2)]^+$ (14). The reduction of $FeCo(CO)_7(\mu\text{-}PPh_2)$ (**8**) with 1 equiv of Na–Hg amalgam in THF results in gas evolution and formation of the green 33e radical anion $[Na(THF)_n][FeCo(CO)_6(\mu\text{-}PPh_2)]$ (**12**) characterized by IR and ESR spectroscopy. While addition of 1 equiv of 18-crown-6 to the reduced solution led to a simplified IR spectrum (Table II), attempts to isolate the radical anion led instead to a red-brown solid identified as $[Na_2(18\text{-crown-6})][FeCo(CO)_6(\mu\text{-}PPh_2)]$ (**13′**) by elemental analysis. The dianion **13**, which presumably forms via a slow disproportionation of the radical anion **12**, is also unstable at 25 °C in THF solution, giving several unidentified diamagnetic products.

A more convenient preparation of the $[FeCo(CO)_6(\mu\text{-}PPh_2)]^-$ radical anion for ESR studies is the instantaneous reaction of the parent complex **8** with 1 equiv of sodium naphthalenide in THF. The spectrum at 25 °C obtained in this manner is shown in Figure 12A. From the improved resolution of the high field lines at −25 °C (Figure 12B), we conclude that the spectrum consists of a ^{59}Co hyperfine multiplet of eight lines ($I(^{59}Co) = {}^7/_2$) with a splitting of 12.4 G, each line of which is further split into doublets by a ^{31}P coupling of 15.1 G ($g = 2.0445$). At −25 °C the low-field lines are broader, and therefore smaller in height, than the high field lines. This effect is common for organometallic radicals and

is caused by the incomplete averaging of the anisotropies of the g and hyperfine tensors by the tumbling of the radical in solution. The ESR parameters can be compared with those of isoelectronic $Co_2(CO)_6[(\mu\text{-}P(t\text{-}Bu)_2]$, which has a substantially larger g factor (2.078) and ^{59}Co coupling (29.5 G).[50] The larger g factor for the dicobalt radical, where the unpaired electron is necessarily equally divided between the two Co centers, results from larger spin–orbit coupling for Co than for Fe since this coupling increases from left to right in the periodic table. As the g factor of the FeCo radical anion is smaller and resembles those of the diiron radicals of this work (Table III), we conclude that the unpaired electron in **12** resides more on the Fe center than on the Co center. The smaller ^{59}Co coupling for **12** compared with that of the dicobalt analogue also agrees with this conclusion.

While electrochemical reduction of monosubstituted $FeCo(CO)_6(PPh_3)(\mu\text{-}PPh_2)$ (**8a**) leads to the monosubstituted 33e radical anion, chemical reduction of **8a** with Na–Hg amalgam or sodium naphthalenide gave unsubstituted **12** as the only observable radical species. Chemical oxidation of **8a** with $[Cp_2Fe]BF_4$ or $AgBF_4$ generated a new 33e radical cation, $[FeCo(CO)_6(PPh_3)(\mu\text{-}PPh_2)]BF_4$ (**14**), which is unstable at room temperature and could not be isolated. The ESR spectrum of **14** in CH_2Cl_2 at room temperature, where the line width is optimal (Figure 12C), consists of a broad, partially resolved triplet with a line width of ca. 11 G, a splitting for two equivalent or nearly equivalent P atoms of ca. 18.7 G, and a g factor of 2.0504. These spectral parameters are similar to those of a series of trigonal-bipyramidal 17e radicals $[Fe(CO)_3L_2]^+$ (L = phosphine and phosphite ligand).[51] This suggests that the ligand environment around the iron center in this radical cation may also be a distorted trigonal bipyramid much as in **1** at the five-coordinate Fe center. One CO ligand must therefore have migrated from Fe to Co to give a cationic six-coordinate Co(I) center. The ^{59}Co hyperfine splitting in this radical is evidently small and only broadens the spectral lines.

Conclusions

Structural Considerations. The seven different structural types encountered in this study (Figure 13) reflect the electronic diversity of the complexes. While the 34e FeCo and $[Fe_2]^-$ $M_2L_7(\mu\text{-}P)$ complexes have different ground-state structures (A and C, respectively), their 36e $M_2L_8(\mu\text{-}P)$ counterparts are isostructural (F). The 35e Fe_2 complexes, on the other hand, possess the unique triply bridged structure E similar to $Fe_2(CO)_9$.[52] As found for many other dinuclear metal carbonyl complexes, these structures are likely to lie very close in energy, as evidenced by the observation of A and C for two different isomers of $FeCo(PMe_3)_2[P(OMe)_3](CO)_4(\mu\text{-}AsMe_2)$[22] and by the observation of D and E for $HFe_2(CO)_7(\mu\text{-}PPh_2)$ in the solid state and in solution, respectively (H replaces CO in E).[53]

Stereoselectivity and Stereochemistry of Ligand Substitution. Mono- and disubstitution in the three systems examined in this study appear to be stereoselective, with a single isomer, or at worst two isomers with one clearly preferred, being observed. These results contrast with those observed for the RuCo system[24] in which mixtures of isomers were obtained, even though ligand substitution was confined to the Ru center. Low-temperature ^{31}P NMR spectra gave no indication of "freezing out" further substitutional isomers (nor any temperature dependence of the two-bond P–P coupling between L and the PPh_2 bridge), except for the disubstituted 34e anions, **6d,e**, and the trisubstituted cations, **5a,b**. The temperature dependence of the ^{31}P and ^{13}C hyperfine splittings observed in the ESR spectra of 35e $Fe_2(CO)_7(PEt_3)(\mu\text{-}PPh_2)$, however, suggests that the details of CO ligand mobility must be worked out before an accurate assessment of stereoselectivity can be rendered.

The stereochemistry of substitution in all three systems appears to follow from steric considerations. While the initial site of nucleophilic attack on structure A is likely to be the five-coordinate metal center, different products are observed for the Fe_2 and FeCo systems. If we assume that L is trans to the PPh_2 bridge in the initial 35e (structure E, **3a,b**) or 36e (structure F, **11**) adducts and that CO ligand loss occurs from the equatorial belt cis to L,[48] the former can interconvert five- and six-coordinate metal centers by simple transfer of a CO ligand, giving **2a–d**, while the latter must interchange CO and L in rearranging from **8a′–c′** to the thermodynamically stable isomer **8a–c**. Disubstitution is also likely to occur at the five-coordinate, unsubstituted metal center, affording the 35e (**3c–f**) or 36e (**10a,b**) adducts with both L's trans to the PPh_2 bridge. The former is unstable in the absence of CO and gives rise to major and minor isomers of the disubstituted 33e radicals **4a–c** and **4a′–c′**. While the stereochemistry of these isomers is uncertain, EHMO calculations[1] on A indicated that the SOMO is localized largely on the five-coordinate metal center and its two equatorial ligands cis to the PPh_2 bridge. If disubstitution occurs to give both L's trans to the PPh_2 bridge, we would expect no hyperfine splitting from L on the six-coordinate center (as demonstrated for the monosubstituted 33e Fe_2 radicals) and only a small coupling to L on the five-coordinate center.[2] This is, in fact, the splitting pattern observed for the major isomers **4a–c** (Table III). If, however, the second substitution places L on the five-coordinate center cis to the PPh_2 bridge, a much larger hyperfine splitting is expected, as observed for the minor isomers **4a′–c′**. This proposal is supported by the qualitative observation that the amount of the minor isomer increases as the steric bulk of the phosphorus ligand decreases.

Disubstitution in the FeCo system suggests that there may also be an electronic factor in the stereochemical outcome, as different structures are indicated by ^{31}P NMR for the 34e PMe_3 and $P(OMe)_3$ derivatives **9a,b**. The 36e complexes **10a,b** have similar spectral features (δ, Fe–L > Co–L; $^2J_{PP}$, |Co–L| > |Fe–L|, $|P(OMe_3)| = 2|PMe_3|$), which are shared by **9b**, which has both PMe_3 ligands trans to the PPh_2 bridge (Figure 13, structure A). However, complex **9b** shows no trans two-bond P–P coupling between the PPh_2 bridge and the Co-bound $P(OMe)_3$ and has been shown by X-ray diffraction to have structure B with $FeP(OMe)_3$ trans to the PPh_2 bridge and $CoP(OMe)_3$ trans to the FeCo bond. If we assume that for the disubstituted complexes structure B is preferred by electronic factors and that structure A is favored by the bulkier PMe_3 ligand, the implications for the analogous diiron system are intriguing. Since the amount of the minor isomer increases as the steric bulk of L decreases and since the ESR parameters of the less bulky PEt_2-bridged analogue $Fe_2(CO)_5[P(OMe)_3]_2(\mu\text{-}PEt_2)$ resemble those of the minor isomer, we suggest that the minor disubstituted isomer, **4a′–c′**, has structure B with L on the six-coordinate Fe center trans to the PPh_2 bridge and L on the five-coordinate Fe center trans to the Fe–Fe bond. Attempts to isolate and crystallize $Fe_2(CO)_5[P(OMe)_3]_2(\mu\text{-}PEt_2)$ are presently under way in order to test this proposal. Finally, we note that the IR spectra of the substituted FeCo complexes resemble those observed by Langenbach and Vahrenkamp[22] for the $AsMe_2$-bridged analogues. The major differences are our lack of observation of monosubstituted 36e complexes (except for L = PMe_3), the ready rearrangement at 25 °C of the Co–L monosubstituted 34e complexes (except for L = $P(OMe)_3$), the lack of observation of complexes with more than one L on Co, and the reluctance of the PPh_2-bridged system to undergo trisubstitution at 25 °C in the presence of excess L.

In addition to reacting 440000 times faster, the major difference in the substitution chemistry of the Fe_2 vs the FeCo system involves the natural substitution limits. In the $AsMe_2$-bridged FeCo system the 36e tetrasubstituted complexes represent the substitution limit, as loss of L becomes preferred over CO loss.[22] In the PPh_2-bridged Fe_2 system, however, the trisubstituted 35e radicals become so electron-rich that electron transfer to a less substituted dinuclear species occurs to give the diamagnetic disproportionation products. This point is illustrated by the results of adding less than 3 equiv of $P(OMe)_3/Fe_2$ radical. One then observes unsubstituted and

(50) Baker, R. T., unpublished results.
(51) (a) Baker, P. K.; Connelly, N. G.; Jones, B. M. R.; Maher, J. P.; Somers, K. R. *J. Chem. Soc., Dalton Trans.* **1980**, 579. (b) Therien, M. J.; Trogler, W. C. *J. Am. Chem. Soc.* **1986**, *108*, 4037.
(52) Cotton, F. A.; Troup, J. M. *J. Chem. Soc., Dalton Trans.* **1974**, 800.
(53) Baker, R. T.; Krusic, P. J.; Menon, R.; San Filippo, J., to be submitted for publication.

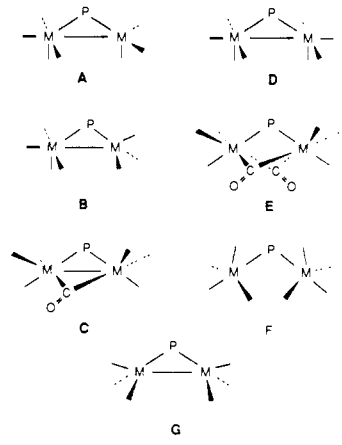

Figure 13. Structures of PR_2-bridged dinuclear metal carbonyl complexes; (A–C) $M_2L_7(\mu\text{-P})$; (D–F) $M_2L_8(\mu\text{-P})$; (G) $M_2L_6(\mu\text{-P})$.

mono- and disubstituted 36e anions but only the trisubstituted 34e cation.

The substitution chemistry of the $[Fe_2]^-$ system is unique, providing only the disubstituted 36e complexes, presumably by S_N2 attack on the five-coordinate Fe center in the monosubstituted 36e intermediate, as the intermediacy of the monosubstituted 34e complex could be ruled out and the monosubstituted 36e complex is only observed in the absence of excess L.

The proposed structure (G, Figure 13) of the radical anion $[FeCo(CO)_6(\mu\text{-}PPh_2)]^-$ (**12**) resembles that proposed by Albright et al.[54] for the neutral dicobalt analogue on the basis of EHMO calculations; the structure with two ligands trans to the PR_2 bridge was found to be 5 kcal higher in energy than G for $Co_2(CO)_6(\mu\text{-}PH_2)$. The reduction of **12** to the dianion **13** is also to be expected based on the analogous dicobalt radicals $Co_2(DMPM)_2(PMe_3)_2(\mu\text{-}PMe_2)$[54] (DMPM = $CH_2(PMe_2)_2$) and $Co_2(CO)_6[\mu\text{-}P(t\text{-}Bu)_2]$,[50] which are both easily reduced to the 34e anions. The ESR spectra of the radical cation $[FeCo(CO)_6(PPh_3)(\mu\text{-}PPh_2)]^+$ (**14**) shows two comparable ^{31}P hyperfine splittings and no detectable ^{59}Co hyperfine splitting. Although the thermal instability of **14** precluded its complete characterization, the ESR data are consistent with structure A (Figure 13) having the cationic charge localized on the six-coordinate Co(I) center. The unpaired electron spin density would then be centered on the five-coordinate Fe which also bears the PPh_3 ligand.

The results of the kinetic investigation of CO substitution in $Fe_2(CO)_7(\mu\text{-}PPh_2)$ by PR_3 ligands parallel those obtained[55] by Poe et al. for $FeCo(CO)_7(\mu\text{-}AsMe_2)$, although 36e monosubstituted complexes were obtained in the latter study. Previous workers[7,56] have separated the importance of steric factors (the cone angle θ) and electronic factors (pK_a) in determining the overall rate of substitution at metal complexes with PR_3 nucleophiles. Regression analysis of our data with θ and pK_a as dependent variables affords the relationship of eq 17 with a

$$\log k_1 = 6.93 + 0.060pK_a - 0.036\theta \qquad (17)$$

correlation coefficient of 0.98 for the five phosphine ligands examined. Addition of the data points for $PPh(OMe)_2$ and $P(OMe)_3$ reduces the fit to 0.89, suggesting that other factors, such as π-acidity, may be important in determining the reactivity of these ligands. Indeed, when Geiring's π-acidity ($E\pi_a$) parameter[56] is included, the fit of eq 18 gives a correlation coefficient of 0.97

$$\log k_1 = 6.92 + 0.059pK_a - 0.036\theta - 4.72E\pi_a \qquad (18)$$

as shown in Figure 14. Note that addition of the $E\pi_a$ parameter improves the fit without changing the coefficients that describe the relative importance of steric and σ-electronic effects found in eq 17.

(54) Karsh, H. H.; Milewski-Mahrla, B.; Besenhard, J. O.; Hofmann, P.; Stauffert, P.; Albright, T. A. *Inorg. Chem.* **1986**, *25*, 3811.
(55) Jackson, R. A.; Kanluen, R.; Poe, A. *Inorg. Chem.* **1981**, *20*, 1130.
(56) Golovin, M. N.; Rahman, M. M.; Belmonte, J. E.; Geiring, W. P. *Organometallics* **1985**, *4*, 1981.

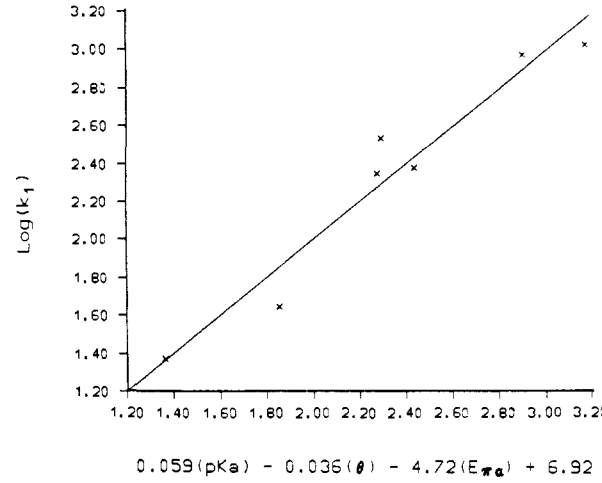

Figure 14. Correlation of the rate constants log k_1 for carbonyl substitution at $Fe_2(CO)_7(\mu\text{-}PPh_2)$ with the combined steric and electronic effects of the various tertiary phosphorus nucleophiles.

From the point of view of reactivity, a metal-centered radical in a dinuclear complex resembles that of a mononuclear radical such as $V(CO)_6$. Both compounds undergo ligand substitution rapidly because of the availability of a low-energy associative process, which must occur through an electron-rich[12] (hypervalent)[9] transition state. The reactivity enhancement observed for electron deficient cluster radicals relative to closed-shell analogues appears (on the basis of a limited comparison) less than in mononuclear complexes. Whether this arises from decreased reactivity of the radical or increased reactivity of the even electron cluster remains to be established. Ligand dissociation appears to be the preferred mode of reactivity[17] for electron-rich polynuclear radicals formed by 1e reduction of the closed-shell cluster. This trend also parallels results[14] for mononuclear radicals.

Acknowledgment. We thank S. A. Hill, D. J. Jones, W. J. Marshall, and T. J. Onley for skilled technical assistance and Prof. A. J. Carty (University of Waterloo) for valuable comments on ^{31}P NMR spectroscopic assignments. The electrochemical and kinetic studies were supported by the National Science Foundation (Grant CHE-85-04088), and W.C.T. thanks the Alfred P. Sloan Foundation for a research fellowship.

Registry No. 1, 102211-00-7; **2a**, 116783-54-1; **2b**, 116783-55-2; **2c**, 116783-56-3; **2d**, 116783-57-4; **3**, 102211-04-1; **3a**, 116783-58-5; **3b**, 116783-59-6; **3c**, 116783-60-9; **3d**, 116783-61-0; **3e**, 116783-62-1; **3f**, 116783-63-2; **4a**, 116783-64-3; **4a'**, 116839-28-2; **4b**, 116783-65-4; **4b'**, 116839-29-3; **4c**, 116783-66-5; **4c'**, 116839-30-6; **5a**, 116946-62-4; **5b**, 116783-70-1; **6**·Et_4N, 116783-71-2; **6a**, 116783-73-4; **6b**, 116783-75-6; **6c**, 116783-77-8; **6d**, 116783-79-0; **6e**, 116783-81-4; **7a**, 116783-83-6; **7b**, 116783-85-8; **7c**, 116839-31-7; **7d**, 116783-87-0; **7e**, 116783-89-2; **7f**, 116783-91-6; **8**, 22852-98-8; **8**$^-$, 116783-92-7; **8a**, 116783-93-8; **8a'**, 116783-94-9; **8b**, 116783-95-0; **8b'**, 116783-96-1; **8c**, 116783-97-2; **8c'**, 116783-98-3; **9a**, 116783-99-4; **9b**, 116784-00-0; **10a**, 116784-01-1; **10b**, 116784-02-2; **11**, 116784-03-3; **12**, 116784-04-4; **12**·Na, 116784-05-5; **12'**, 116784-06-6; **13**, 116784-07-7; **13'**, 116784-09-9; **14**, 116808-53-8; $Fe_2(CO)_7(PEt_2)$, 102210-99-1; $Fe_2(CO)_8(PEt_2)$, 102211-03-0; $Fe_2(CO)_6[P(OMe)_3](PEt_2)$, 116784-10-2; $Fe_2(CO)_7[P(OMe)_3](PEt_2)$, 116784-11-3; $Fe_2(CO)_5[P(OMe)_3]_2(PEt_2)$, 116808-54-9; $Fe_2(CO)_6[P(OMe)_3]_2(PEt_2)$, 116784-12-4; $Fe_2(CO)_4[P(OMe)_3]_3(PEt_2)$, 116784-13-5; $Fe_2(CO)_6[PPh(OMe)_2](\mu\text{-}PPh_2)$, 116784-14-6; $Fe_2(CO)_6(PPh_2Me)(\mu\text{-}PPh_2)$, 116784-15-7; $Fe_2(CO)_6(PPhMe_2)(\mu\text{-}PPh_2)$, 116784-16-8; $Fe_2(CO)_6(PCy_3)\mu\text{-}PPh_2)$, 116784-17-9; PCy_3, 2622-14-2; PPh_3, 603-35-0; PPh_2Me, 1486-28-8; $PPhMe_2$, 672-66-2; PMe_3, 594-09-2; $PPh(OMe)_2$, 2946-61-4; $P(OMe)_3$, 121-45-9; $FeCo(CO)_6(PPh_3)(\mu\text{-}PPh_2)^-$, 116784-18-0.

Supplementary Material Available: Listings of atomic coordinates and temperature factors for hydrogen atoms and anisotropic thermal parameters for non-hydrogen atoms (8 pages); tables of observed and calculated structure factor amplitudes (20 pages). Ordering information is given on any current masthead page.